

Weird Narrow-Line Seyfert 1s: A Multi-Epoch, Broadband Analysis to  
Study the X-Ray Emission in Mrk 1239 and WKK 4438

by

Margaret Z Buhariwalla

A Thesis Submitted to Saint Mary's University, Halifax, Nova Scotia in Partial Fulfillment  
of the Requirements for the Degree of MSc in Astronomy  
(Department of Astronomy and Physics)

2021, Halifax, Nova Scotia

© Margaret Buhariwalla, 2021

Approved: \_\_\_\_\_

Dr. Luigi Gallo

Approved: \_\_\_\_\_

Dr. Ian Short

Approved: \_\_\_\_\_

Dr. Roby Austin

Date: August 16 2021.

## **Acknowledgements**

This work was completed almost entirely during the Covid-19 pandemic. Meaning all research discussions, collaborative work, feedback and meetings have taken place virtually. With this in mind, I would like to thank my supervisor Dr. Luigi Gallo for his support and patience during this incredibly difficult time for everyone.

I would also like to thank all faculty and staff who have done a wonderful job of keeping the department running smoothly over the last 18 months.

Finally I'd like to thank all the other grad students and members of the SMASHERS research group who have all done their best to foster a scene of community while we have been apart.

# Contents

<b>1</b>	<b>Introduction</b>	<b>1</b>
1.1	What is an AGN . . . . .	1
1.1.1	Active and Normal Galaxies . . . . .	2
1.1.2	Unification . . . . .	2
1.1.3	Spectral Energy Distribution . . . . .	4
1.2	X-Ray Emitting Region of an AGN . . . . .	6
1.2.1	Primary X-ray Source . . . . .	7
1.2.2	Soft Excess . . . . .	9
1.2.3	Blurred Disc Reflection . . . . .	10
1.3	Narrow Line Seyfert 1s . . . . .	13
1.3.1	NLS1 and BLS1 . . . . .	13
1.3.2	Disc Emission in NLS1 . . . . .	14
1.3.3	Disc-Jet Connection . . . . .	16
1.4	This Work . . . . .	18
1.4.1	Mrk 1239 . . . . .	18
1.4.2	WKK 4438 . . . . .	19
<b>2</b>	<b>Uncovering the primary X-ray emission and possible starburst component in the</b>	

<b>polarized NLS1 Mrk 1239</b>	<b>21</b>
2.1 Introduction . . . . .	21
2.2 Observations and Data Reduction . . . . .	25
2.2.1 <i>XMM-Newton</i> . . . . .	25
2.2.2 <i>Suzaku</i> . . . . .	27
2.2.3 <i>NuSTAR</i> and <i>Swift</i> . . . . .	28
2.3 Characterizing the Variability . . . . .	28
2.3.1 Long term Variability . . . . .	28
2.3.2 Rapid variability . . . . .	30
2.4 Spectral Modelling . . . . .	34
2.4.1 <i>NuSTAR/Swift</i> . . . . .	34
2.4.2 Multi-epoch Spectral Modelling . . . . .	37
2.4.2.1 Partial Covering . . . . .	38
2.4.2.2 Blurred Reflection . . . . .	46
2.5 Discussion . . . . .	49
2.5.1 Origins of the soft excess . . . . .	50
2.5.2 The hard X-ray spectrum of Mrk 1239 . . . . .	54
2.6 Conclusion . . . . .	56
<b>3 Multi-Epoch, Broadband Analysis of WKK 4438: Origins of the Broad Iron Line and Hard Excess</b>	<b>59</b>
3.1 Introduction . . . . .	59
3.2 Data Reduction . . . . .	61
3.2.1 <i>NuSTAR</i> and <i>Swift</i> . . . . .	62
3.2.2 <i>Suzaku</i> . . . . .	63

3.3	Characterizing the Variability . . . . .	63
3.3.1	Rapid Variability . . . . .	63
3.3.2	Long Term Variability . . . . .	67
3.4	Spectral Modelling . . . . .	69
3.4.1	Double Powerlaw . . . . .	73
3.4.2	Blurred reflection . . . . .	78
3.5	Discussion . . . . .	80
3.5.1	Blurred Reflection . . . . .	80
3.5.2	Hard Excess . . . . .	82
3.5.3	Broad Iron Line . . . . .	83
3.6	Conclusion . . . . .	85
<b>4</b>	<b>Conclusion</b>	<b>87</b>

# List of Figures

1.1	Unification model of AGN . . . . .	3
1.2	Spectral Energy Distribution of AGN . . . . .	4
1.3	Diagram of the inner X-ray producing region of an AGN . . . . .	8
1.4	Spectra of inner region of AGN . . . . .	8
1.5	Reflected disc emission . . . . .	11
1.6	Broad Fe $K\alpha$ line profile . . . . .	12
1.7	Blurred reflection spectra . . . . .	12
1.8	Blazar SEDs . . . . .	16
2.1	The unfolded spectra of Mrk 1239 . . . . .	29
2.2	<i>NuSTAR</i> and <i>Suzaku</i> lightcurves of Mrk 1239 . . . . .	31
2.3	Mrk 1239 Data and Background model. . . . .	35
2.4	Best fit partial covering model applied to Mrk 1239 . . . . .	39
2.5	Best fit blurred reflection model applied to Mrk 1239 . . . . .	48
2.6	Physical interpretation of Mrk 1239 . . . . .	57
3.1	The lightcurve from the 2018 <i>NuSTAR</i> observation of WKK 4438 . . . . .	64
3.2	The hardness ratio of WKK 4438's 2018 <i>NuSTAR</i> observation. . . . .	65
3.3	The Fractional Variability of WKK 4438 . . . . .	66

3.4	The unfolded spectra of WKK 4438 . . . . .	67
3.5	The difference Spectra of WKK 4438 . . . . .	68
3.6	Power law fit to WKK 4438 . . . . .	70
3.7	WKK 4438 Fe $K\alpha$ investigation . . . . .	71
3.8	WKK 4438 Double Powerlaw . . . . .	74
3.9	WKK 4438 Blurred Reflection . . . . .	79
3.10	Model comparison between N2013 and N2018 . . . . .	81
3.11	WKK 4438 <i>PIN</i> and <i>BAT</i> spectra . . . . .	82
4.1	Simulated ionized partial covering data fit with blurred reflection model. . . . .	88
4.2	Simulated RGS spectra . . . . .	89

# List of Tables

2.1	Observation log for Mrk 1239. . . . .	26
2.2	Quantitative measure of LC . . . . .	32
2.3	Best-fit model parameters for Mrk 1239 . . . . .	45
2.4	Flux and luminosity for each model component between 0.5 – 2 keV. . . . .	52
3.1	Observation log for WKK 4438. . . . .	62
3.2	Quantitative measure of HR . . . . .	65
3.3	WKK 4438 model Parameters . . . . .	77



# Abstract

## Weird Narrow-Line Seyfert 1s: A Multi-Epoch, Broadband Analysis to Study the X-Ray Emission in Mrk 1239 and WKK 4438

by Margaret Z. Buhariwalla

X-ray emission from Seyfert 1 galaxies has a debated origin. The primary X-ray source is the compact corona, but the secondary X-ray emission is thought to originate from either a Comptonising layer or blurred reflection from the accretion disc. Finding objects that do not fit into this standard framework are important for understanding the class as a whole. We examine broadband, multi-epoch data of two atypical NLS1s, Mrk 1239 and WKK 4438. While both objects are defined as Seyfert 1s based on optical classification, their X-ray emission is poorly understood. We use broadband multi-epoch spectroscopy to model X-ray emission and examine the timing properties of both galaxies. In Mrk 1239 we determine that the spectra are consistent with high absorption and emission from a distant starburst component. In WKK 4438, we discover excess emission above 30 keV, that may point to a jet origin. Blurred reflection and Comptonisation fail to describe either object indicating the standard paradigm for the X-ray emission cannot be applied universally.

August 16, 2021

# Chapter 1

## Introduction

### 1.1 What is an AGN

Active Galactic Nuclei (AGN) are supermassive black holes (SMBHs) that have matter falling onto them via an accretion disc. The SMBH and the disc form the central engine that powers the AGN. AGN emit in a broad spectral band across the whole electromagnetic spectrum. AGN can have vastly different spectra based on their geometry and composition (Netzer 2013).

Seyfert (1943) first identified a group of 12 ‘extragalactic nebulae’ (now known to be galaxies) with high ionization optical emission lines in their nuclear region. These emission lines had broader widths than expected from observations of planetary nebulae, and as a whole these galaxies were brighter than the average spiral galaxy. Seyfert had compiled the first catalogue of AGN host galaxies, as such near-by AGN are given the historical name Seyfert Galaxy. AGN come in many different forms, they are typically classified by their radio properties, optical line widths, obscuration and viewing angles.

### 1.1.1 Active and Normal Galaxies

The difference between a normal galaxy and one that hosts an AGN is the proximity of matter to the SMBH at the centre of them. An AGN will have matter in much closer proximity of the SMBH and well within the tidal limit of the singularity. Netzer (2013) states that a galaxy is defined as an AGN if one or more of the following conditions holds:

1. The galaxy is host to a compact region that emits excess energy significantly above what is expected from stellar processes.
2. There is a non-stellar continuum present in the galaxy centre.
3. There are strong emission lines with line ratios that must originate from non-stellar radiation fields.
4. There is continuum variation present in the spectra of the galaxy.

The spectral energy distribution (SED) of an AGN is characterized by its very broad shape spanning the entire electromagnetic spectrum. Figure 1.2 shows a comparison between a normal galaxy template and a variety of AGN templates. The normal galaxy template is primarily composed of a collection of blackbody spectra over a small range of temperatures to account for the stellar emission from different populations of stars (Peterson 1997). The AGN cannot be modelled with a single blackbody. A staple of AGN SED is the presence of X-ray emission (Peterson 1997). AGN have the distinct property of having relatively consistent emission in each waveband, from the radio to  $\gamma$ -ray emission, different process combine to make the flat broadband spectrum (Section 1.1.3).

### 1.1.2 Unification

A unified model of AGN activity is proposed as a way to broadly describe all the characteristics that are seen in the AGN population. Unification attempts to describe all AGN based on

the presence of a radio jets and viewing angle. Figure 1.1 shows the different types of AGN based on their viewing angle and radio properties. AGN were originally divided into one of

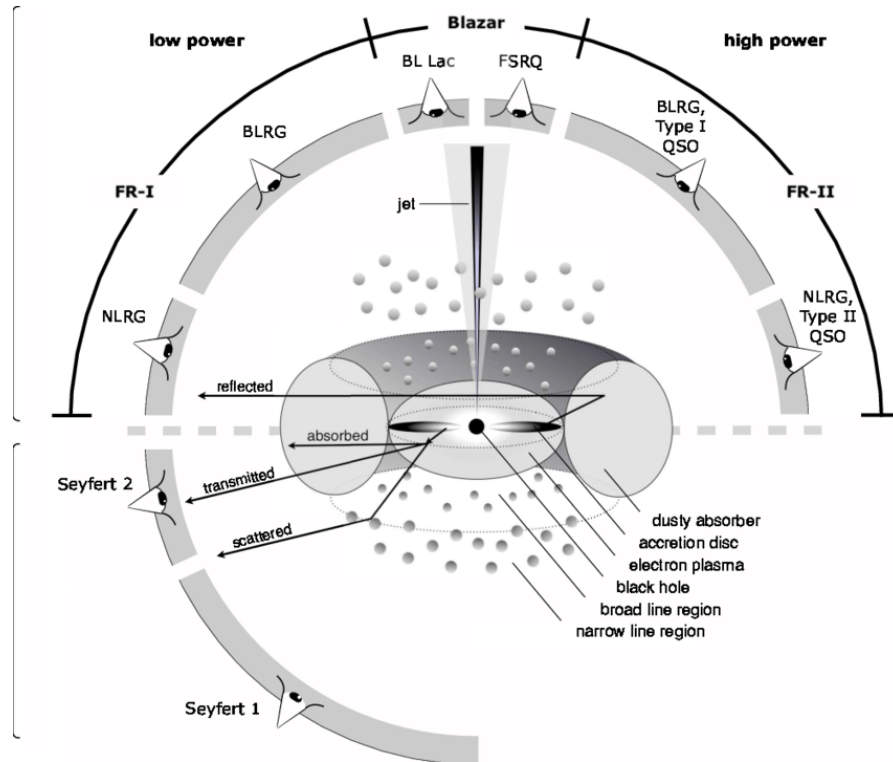


Figure 1.1: Unification model of AGN (Beckmann & Shrader 2013). Many of the differences can be attributed to orientation effects.

two categories, type I or type II. Type I AGN have a clear, generally unobstructed, view of the central engine of the AGN whereas type II AGN have a fully obstructed view. Type I AGN have generally broader emission lines originating from the BLR which is contained within the torus. In type II, the BLR is obscured and only the distant NLR is visible (Netzer 2013). This viewing angle effect is thought to originate from the dust torus (Antonucci & Miller 1985; Antonucci 1993). Osterbrock (1977) introduced the groups 1.2, 1.5, 1.8 to describe those intermediate galaxies, which had more obscuration than type Is but less than type IIs.

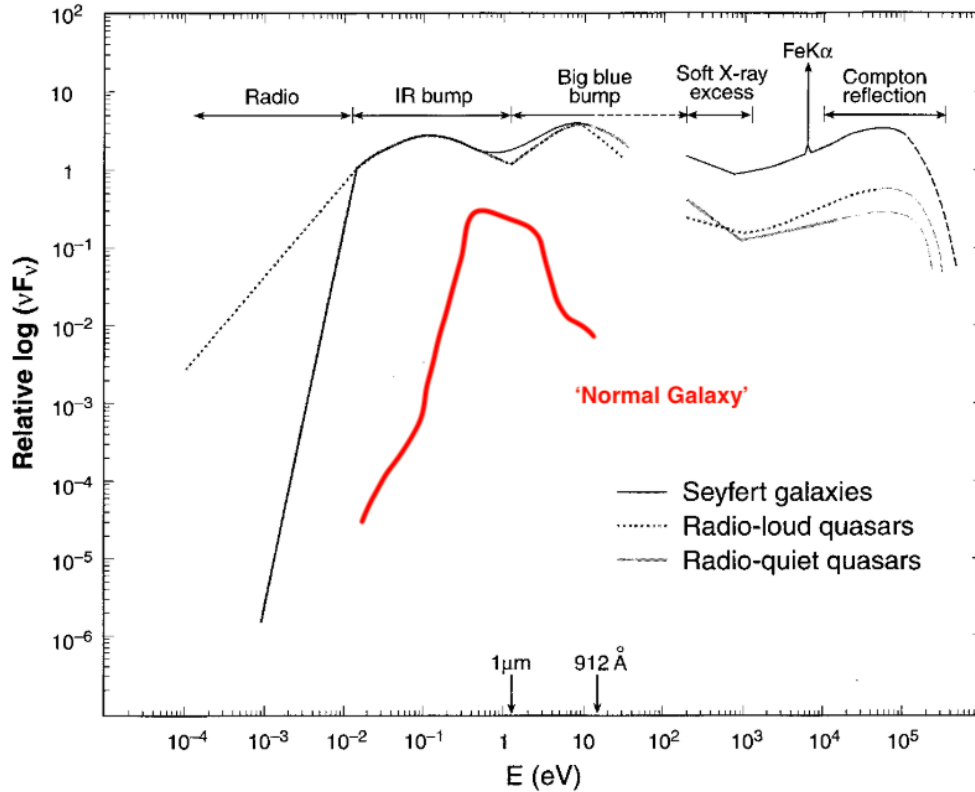


Figure 1.2: Spectral Energy Distribution of AGN (Koratkar & Blaes 1999) with a normal galaxy template from Peterson (1997) reproduced in red.

### 1.1.3 Spectral Energy Distribution

The radio loudness (denoted as  $R$ ) of a galaxy is determined by its the ratio of the radio-to-optical flux density in select bands. By convention the radio flux density is measured at 5 GHz while the optical flux density is measured at  $4400\text{\AA}$ . A radio quiet (RQ) galaxy has an  $R$  value less than 1, while a radio-loud (RL) galaxy has an  $R$  value greater than 10 (Kellermann et al. 1989). There are many physical sources for radio emission in galaxies, as well as many different radio morphologies. A common classification is Fanaroff-Riley (FR) type I or II. FRI have the brightest radio emission close to the host galaxy centre. FR II have their brightest radio regions away from the centre of the host galaxy (Fanaroff & Riley 1974). The source of radio emission from an AGN is due to the synchrotron emission produced by the radio jets.

In AGN the infrared (IR) emission is thought to be originating from dust that has been heated by processes related to the central engine. The emission can be from warm, cool, or hot dust particles and it covers the emission from near-IR to mid-IR. The infrared emission from an AGN originates from the torus ( $\sim 1$  pc) (Netzer 2013).

Optical images of Seyfert 1s show point sources at the centre of their host galaxy and the optical spectra of AGN lack the traditional stellar absorption lines. Together this is strong evidence for a non-stellar origin for the optical emission. Emission from the central engine can often outshine the entire host galaxy. Optical emission from AGN comes from several regions; the broad line region (BLR); the narrow line region (NLR) and the disc (Netzer 2013).

The BLR is a region of dense gas that surrounds the AGN, the emission from the central engine will photoionize this region. Resulting in a collection of emission lines in the optical spectra. Due to the proximity to the SMBH the gas clouds that form the BLR orbit the black hole with Keplerian speeds on the order of 1000s of  $\text{km s}^{-1}$ . This results in Doppler broadening of the the emission lines, thus the name of the region.

The NLR is a region of the galaxy that contains lower density gas at a larger distance from the SMBH (several kpc). It is ionized by the same source as the BLR but due to the large distance between the NLR and the SMBH, the velocities of the gas are much smaller resulting in lines that are narrow instead of broadened (Netzer 2013).

Due to absorption in the AGN host galaxy as well as absorption in our own it is near impossible to observe AGN (or other extragalactic sources) in the far-UV band. A significant source of UV photons is thought to be the accretion disc surrounding the black hole (Koratkar & Blaes 1999). In the standard Shakura-Sunyaev accretion disc, the disc is assumed to be geometrically thin and optically thick. The disc is heated when friction between layers of the disc removes angular momentum moving closer to the SMBH. Gravitational energy is released as the material gets closer to the SMBH in the form of kinetic (to maintain the orbit around the SMBH) and

thermal energy heating the disc (Shakura & Sunyaev 1973; Longair 2011).

The temperature of a thin accretion disc falls off to lower temperature as the distance from the SMBH increases ( $T \propto r^{-3/4}$ ). This results in concentric rings of material with constant temperature surrounding the SMBH. Assuming that the material in these rings emits as a blackbody then the combined spectra of the UV disc emission is a modified blackbody that is stretched to cover a broader energy band. At lower energies, the modified blackbody has a Rayleigh-Jean tail that is determined by the temperature in the outer regions of the disc (Longair 2011). The innermost stable orbit (ISCO) is responsible for the Wien tail, where an exponential drop in flux is observed related to the peak temperature of the disc. The maximum temperature of the disc is inversely proportional to the mass of the SMBH,  $T_{disc} \propto M^{-1/4}(L_{disc}/L_{Edd})^{1/4}$  thus larger SMBH are host to cooler discs (Gierliński & Done 2004). This disc emission cannot reproduce the soft excess, discussed in Section 1.2.2 (Laor et al. 1997).

Inside the radio jets, while the production of synchrotron radiation is occurring, the radio photons can inverse Compton scatter off the ultra relativistic electrons producing high energy photons. This process is call Synchrotron Self Comptonization (SSC), and it is the source of the Gamma-ray emission observed from AGN (Netzer 2013). Not all AGN are Gamma-ray sources, but the presence of high energy photons is evidence of possible jet activity. The X-ray producing region of AGN will be discussed in Section 1.2

## 1.2 X-Ray Emitting Region of an AGN

The X-ray emitting region of AGN subtends a physically small region of space. For an AGN with a  $10^6 M_{\odot}$  black hole the central engine is contained within a region less than 100 gravitation radii ( $r_g$ ), where  $r_g = \frac{GM}{c^2}$ . This means that the physical size of the X-ray emitting region would be approximately 2 AU. Current instrumentation is unable to spatially resolve these inner region

scales of extragalactic sources. Instead we rely on spectroscopy to indirectly determine the underlying mechanisms producing the X-ray emission.

A schematic of the central engine can be seen in Figure 1.3, the resultant spectra from just these three components can be seen in Figure 1.4. The most basic X-ray spectra of the typical Seyfert 1 is composed of three main components, the primary emission (blue), the thermal disc emission (pink) and the reprocessed blurred reflection (green). These three spectral components originate from the central regions of the AGN and are dependant on each other (Haardt & Maraschi 1991). Each of these components will be discussed in more detail in the following sections.

### 1.2.1 Primary X-ray Source

In the standard view of an AGN the corona is the source for the primary X-ray emission. We can infer that the corona inhabits a physically small region of space due to its ability to rapidly change flux on timescales as short as hours (Haardt & Maraschi 1993). The corona is composed of an optically thin cloud of electrons that interact with UV seed photons produced by the accretion disc. The electron and the seed photons interact in a process called Comptonization<sup>1</sup>. For Comptonization to occur the electrons must be at relativistic energies, and there must be sufficient numbers of low-energy photons (Shapiro et al. 1976). During this type of scattering a seed photon will scatter off a high energy electron, and some of the electron's momentum and energy is transferred to the photon, resulting in a high energy photon leaving the corona (Rybicki & Lightman 1979; Longair 2011). The photons that leave the corona have an energy distribution related to the optical depth of the corona. In simple geometries a cut-off power law is sufficient to model the Comptonization effect, but more complex geometries may need more complex models (Petrucci et al. 2001).

---

<sup>1</sup>Also called inverse Compton scattering and Compton upscattering.



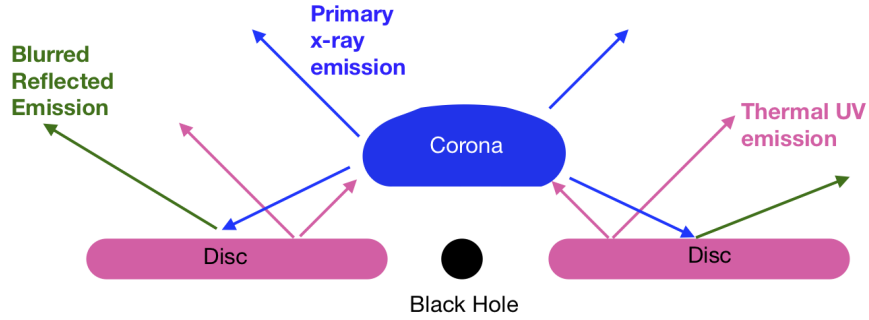


Figure 1.3: Diagram of the inner X-ray producing region of an AGN, photons are emitted as a modified black body by the accretion disc (pink). Electrons in the corona inverse Compton scatters the photons to higher energies, producing the primary X-ray emission (blue). Some of the primary emission escapes the system while some will reflect off the accretion disc before leaving the system and reaching the observer (green).

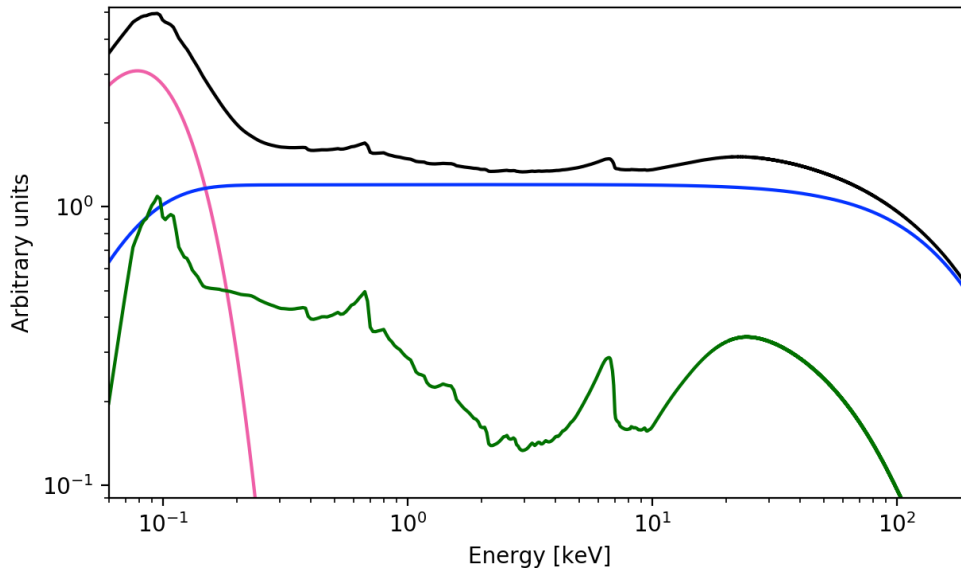


Figure 1.4: Each of the components in Figure 1.3 produces a different spectral shape: the disc emission is modelled with a single blackbody in pink; the primary emission is modelled using a thermally Comptonized continuum (blue); the reflected emission is modelled using a blurred reflection component (green). Together these components make the observed spectrum form the central region of the AGN.

The exact geometry and location of the corona is still a debated topic. The simplest geometry (eg. lamppost geometry) is an optically thin point source some height,  $h$ , above the black hole that radiates isotropically (Wilkins & Fabian 2012; Gonzalez et al. 2017). More complex coronal geometries include an extended cloud surrounding the black hole (Wilkins & Gallo 2015); slab

geometry, where a disc with a finite thickness occupies a space above the accretion disc (Wilkins & Fabian 2012; Gonzalez et al. 2017); and conical geometry, where an inverted cone occupies a space above the black hole (Gonzalez et al. 2017). There is evidence of AGN coronae changing geometry between epochs, as well as a possible connection between the corona and relativistic jets responsible for the synchrotron emission seen in radio loud AGN (Wilkins & Gallo 2015). This is evidence to suggest that the base of the jet could serve as the corona in the central region of the AGN (Wilkins & Fabian 2012). In Mrk 335, one interpretation of the spectra indicated that the corona was the base of a failed jet (Wilkins & Gallo 2015). Gonzalez et al. (2017) found that conical coronal geometry was the most likely scenario for corona-jet connection.

Photons emitted from the corona as the primary X-ray emission have low and high energy cut-offs where the number of photons emitted decreases substantially. The high energy cut-off indicates the temperature of the electrons within the corona (Fabian et al. 2015). The low-energy cut-off reflects the temperature of the seed photons (e.g. UV disc photons).

### **1.2.2 Soft Excess**

The soft excess often seen in AGN has many possible explanations. It is defined as excess emission above the standard power-law continuum produced by the primary X-ray emission in the soft band (energies below 2 keV). It was thought that this excess emission was due to disc UV/soft X-ray photons emitting as a blackbody (Haardt & Maraschi 1991), however the temperatures required to produce the soft excess are not achievable by a standard accretion disc that surrounds a SMBH (Shakura & Sunyaev 1973; Gierliński & Done 2004 ). The actual origin of the soft excess is still unclear, models include a secondary cool corona (Magdziarz et al. 1998); an ionized partial covering scenario (Gierliński & Done 2004); or reflection off a photoionized accretion disc (Ballantyne et al. 2001). Each scenario has a physical motivation and specific objects that motivate the models, it is unlikely there is just one origin of the soft

excess.

A predicted secondary feature of one soft-excess model is the hard excess arising from reflection of high energy photons off optical thick material. Waddell & Gallo (2020) show that there is some correlational between the strength of these two features in NLS1s indicating a possible common origin (blurred disc reflection).

### 1.2.3 Blurred Disc Reflection

During the reflection ‘event’ hard X-ray photons from the corona are either absorbed via photoelectric absorption or Compton scattered off of electrons present in the disc. Compton scattered photons are typically the higher energy coronal photons, as there are few paths for photoelectric absorption for these photons. For the electrons that photo-excited the disc atoms there are two possible paths to de-excitation; Auger emission, or fluorescence. Auger emission does not produce a photon, instead the energy released as the electron drops into a lower shell is reabsorbed by another electron before it can exit the atom (Longair 2011).

A simulation of the reflection spectrum off a disc is shown in Figure 1.5 based off of calculations done by George & Fabian (1991). The strongest emission line present is the Fe  $K\alpha$  line at 6.4 keV. This emission line is formed by the transition of a L-shell electron dropping to the K-shell of the atom. The edge present at approximately 7.1 keV is the iron absorption edge. Photons above this energy are able to eject electrons from the K-shell of the Fe atom.

The spectrum given in Figure 1.5 is not what one would expect to see from an accretion disc surrounding the SMBH as this spectrum does not include any relativistic blurring effects that occur in close proximity to black holes. There are many blurring effects that need to be taken into account to adequately model the reflection spectra. They can be seen most clearly when looking at the Fe  $K\alpha$  emission line in isolation. Figure 1.6 illustrates these effects. The intrinsic line profile of the Fe  $K\alpha$  emission is shown in black. The green line is the effects

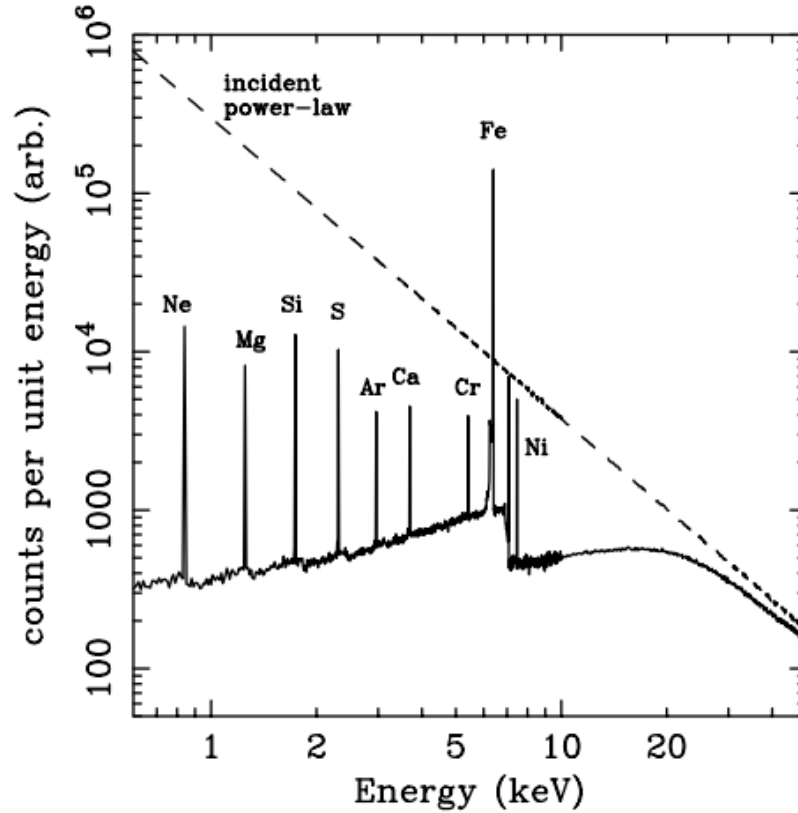


Figure 1.5: Reflected X-ray emission from an optically thick disc with slab geometry (Fabian et al. 2000). The Fe  $K\alpha$  line is the strongest emission line from the disc.

due to Doppler broadening, where the material in the disc moving away from us is redshifted while the material in the disc moving towards us is blue shifted to higher energies. The double horned peak is typical of Doppler profiles. The red line shows the effects of special relativity on the Doppler broadened profile. The material that emits near the edge of the disc is moving at fractions of the speed of light, this causes relativistic beaming to brighten the blue wing of the iron profile, and dim the red wing. Finally General relativistic effects must be taken into account, the photons closest to the black hole will lose energy as they escape the gravitational pull. The combination of these blurring effects results in broad lines emitted. Figure 1.7 shows a reflected spectrum (black) and a blurred reflected spectrum (blue). At low energies the emission lines blend together. In the harder bands the Fe  $K\alpha$  emission line is isolated and extremely broadened, the Compton hump above 10 keV is significant.

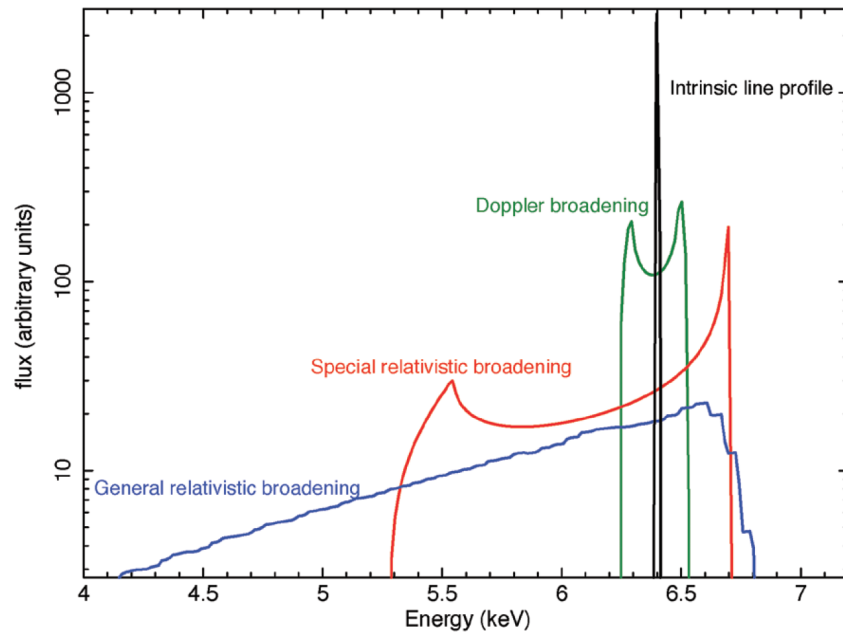


Figure 1.6: An incremental look at the the different processes that occur to photons produced by Fe  $K\alpha$  emission and reflected off the accretion disc surrounding a SMBH. Doppler broadening, special relativistic broadening and general relativistic broadening combine to form the broad Fe  $K\alpha$  line profile, a key component of reflection spectra (Gallo 2011).

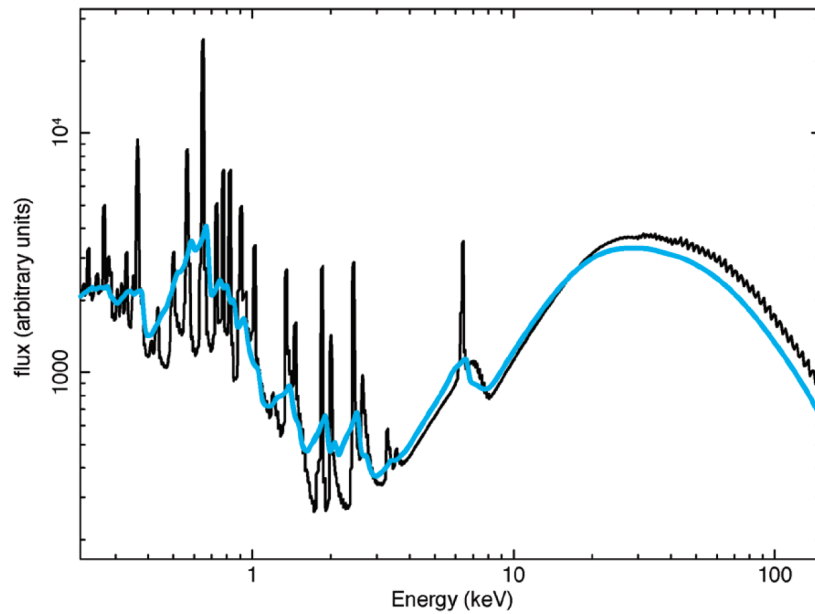


Figure 1.7: In black the reflected spectrum off a disc without any broadening effects, in blue the same spectrum with blurring effects (Gallo 2011).

## 1.3 Narrow Line Seyfert 1s

### 1.3.1 NLS1 and BLS1

The distinction between a Narrow Line Seyfert 1 (NLS1) and a Broad Line Seyfert 1 (BLS1) is based on the full-width at half-maximum (FWHM) measurement of their  $H\beta$  lines in the optical band. NLS1s have an  $H\beta$  line with  $\text{FWHM} < 2000 \text{ km s}^{-1}$  while BLS1s have widths greater than this. NLS1s have small line ratios of  $[\text{O III}]/H\beta$ , and exhibit strong Fe II emission that is inconsistent with type II AGN (Osterbrock & Pogge 1985; Goodrich 1989). NLS1s also accrete at higher fractions of the Eddington limit (see Sec. 1.3.2). The combination of small line-width and higher accretion rates suggest NLS1s might be low-mass SMBH that are growing rapidly (Mathur 2000).

In general, the X-ray band of NLS1s tend to have steeper photon indices (Brandt et al. 1997; Leighly 1999b), which indicate a cooler or more diffuse corona. The soft excess (see Sec. 1.2.2) is a more dominant feature in NLS1s compared to their broad line counter parts (Puchnarewicz et al. 1992). The X-ray variability is more rapid and of higher amplitude in NLS1s than BLS1s, which indicates a physically smaller emitting region (Leighly 1999a; Fabian et al. 2015). However Ponti et al. (2012) showed that this was related to their lower masses rather than a fundamental difference in the populations. NLS1s also show higher levels of excess variance, again indicating a difference in mass from the heavier BLS1s (Leighly 1999a). The excess variance is very tightly correlated with black hole mass and is often used to infer the mass of the SMBH.

At longer wavelengths, NLS1s continue to show interesting behaviour. In the infrared (IR) NLS1s show evidence for an increased amount of star formation as compared to BLS1s (Sani et al. 2010). This implies that AGN with more efficient accretion on to the SMBH have higher star formation rate (SFR). In the radio band, it is less common for NLS1s to host jets, but it is still

possible (Foschini et al. 2012). The general properties of these radio-loud narrow line Seyfert 1s (RL-NLS1) are consistent with radio-quiet NLS1s (RQ-NLS1) (e.g. mass, Eddington ratio, and spectral Index). These RL-NLS1 sources could also be  $\gamma$ -ray sources, with the emission originating in the jet and pointed directly at us (Foschini et al. 2015).

### 1.3.2 Disc Emission in NLS1

The Eddington luminosity ( $L_{Edd}$ ) is the luminosity limit such that the force of gravity (due to the SMBH) per unit area is equal to the radiative pressure of the photons leaving the system. The  $L_{Edd}$  is defined for a point mass, with luminosity  $L$  and mass  $M$ . The Eddington luminosity is given by

$$L_{Edd} = \frac{4\pi cGM\mu m_p}{\sigma_T}, \quad (1.1)$$

where  $c$  is the speed of light;  $G$  is the Gravitational constant;  $M$  is the mass of the black holes;  $\mu$  is the mean molecular weight of the material surrounding the black hole;  $m_p$  is the mass of a proton; and  $\sigma_T$  is the Thomson cross section. This expression for  $L_{Edd}$  assumes that the in-falling material is fully ionized and all the radiative pressure is driven by Thomson scattering. Given the strict assumptions about ionization, geometry and composition of the plasma, we would not expect a source to emit at the Eddington luminosity (Peterson 1997; Netzer 2013). Sources can be super Eddington, but not for extended periods of time. During super Eddington accretion the radiative force will drive away in-falling material, effectively starving the central engine. Without in-falling matter releasing energy the radiative force dips, resulting in a re-start of in-falling material. NLS1s are thought to be accreting at or near the Eddington limit (Pounds et al. 1995).

The reflected spectrum off the accretion disc is best studied in low flux, reflection dominated states. This allows for the reflection component to lead the variability and probe disc properties

(Fabian et al. 2004). The spectra of NLS1 in low flux states are more likely to deviate from a standard power law (showing evidence of reflection) in the 2.5-10 keV energy band (Gallo 2006). This is thought to be connected with the height of the corona over the accretion disc and SMBH, as the corona gets closer to the disc the gravitational effects of the SMBH become more prominent. Light bending effects distort the illumination pattern or emissivity profile of the disc, resulting in lower flux states and higher reflection fractions. This can also affect the spectral variability properties of the source as reflection dominated spectra are expected to vary less rapidly in shape than the power law dominated spectra (Miniutti & Fabian 2004).

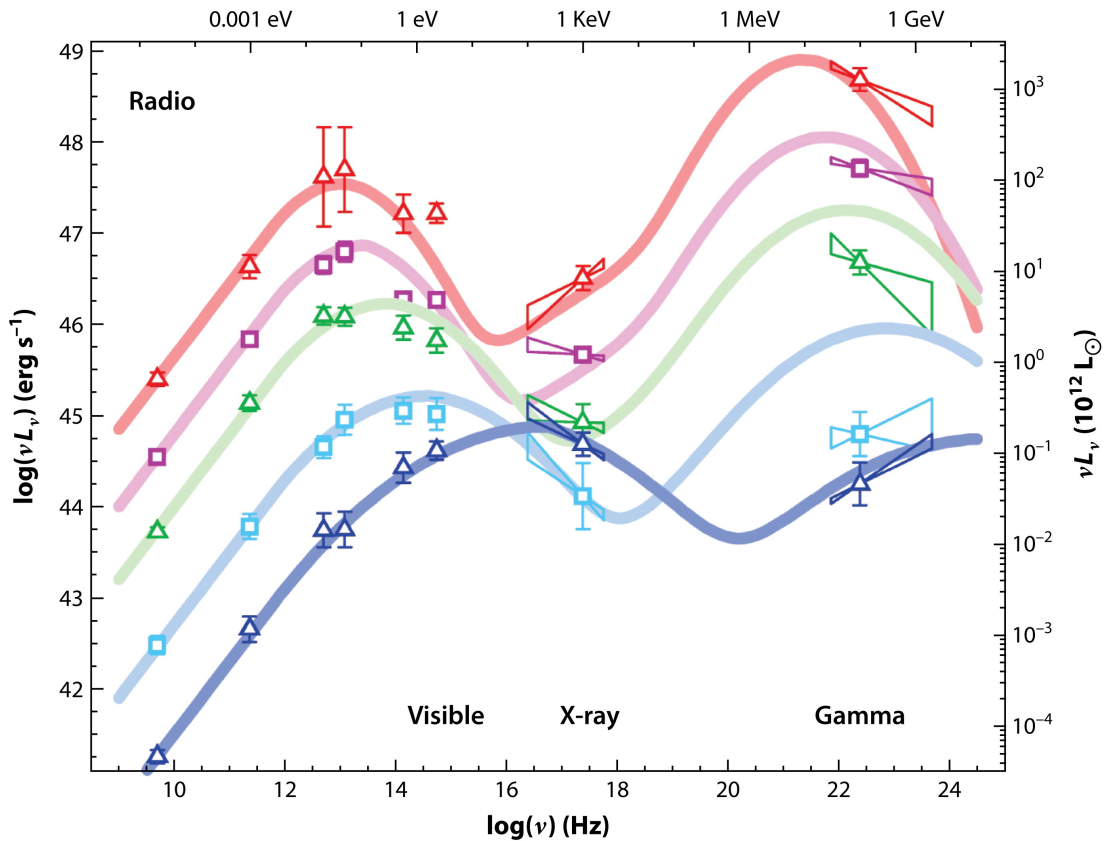
1H0707-495 shows evidence of a Kerr black hole with broadened iron lines ( $\text{Fe K}\alpha$  and  $\text{Fe L}\alpha$ ) resulting from emission from within a few gravitational radii of the SMBH. This object also shows evidence that changes in the primary X-ray emission leads similar changes in the reflected component by approximately 30 seconds. Combining this with the mass of the SMBH, the height of the primary X-ray emission could be determined. The technique is called reverberation mapping and it has the power to probe the inner regions of AGN (Fabian et al. 2009).

In extreme cases it is possible that the inner accretion disc can emit a blackbody-like spectrum. For this to be possible the inner disc must be heated by a combination of high accretion rates around a low mass SMBH while still in the thin disc regime. The combination of coronal emission and returning radiation (Cunningham 1976) close to the SMBH will blur the evidence of the reflection spectra producing a blackbody-like feature. IRAS 13224-3809, a high spin NLS1 shows evidence that the soft excess is in fact due to some sort of emission related to the disc. Further observations of this object suggested the need for this blackbody component could be removed if different disc reflection models were considered. A high density disc model could potential explain the blackbody-like emission (Jiang et al. 2018).



### 1.3.3 Disc-Jet Connection

In the inner regions of radio loud AGN, collimated clouds of ultra-relativistic electrons are pushed away from the central regions. These jets of electrons produce synchrotron emission due to the presence of magnetic fields. Sometimes the electrons can boost external photons to  $\gamma$ -ray energies by inverse Compton scattering. This results in a peak of emission in the radio and  $\gamma$ -ray band, Figure 1.8 shows this characteristic double peaked behaviour (Netzer 2013). In




 Blandford R, et al. 2019.  
*Annu. Rev. Astron. Astrophys.* 57:467–509

Figure 1.8: Selection of SEDs for different blazars, note the peaks in the low frequency from synchrotron emission, and the high frequency from inverse Compton scattering, characteristic of jet emission (Blandford et al. 2019).

some sources the base of the jet could be directly connected to the accretion disc surrounding the SMBH (Blandford et al. 2019). The base of the jet may be able to serve as the source of the primary X-ray emission, combining with or replacing the traditional diffuse corona (Wilkins

& Gallo 2015). It is difficult to disentangle the jet emission from coronal or reflected emission. 3C 273 is a nearby high luminosity quasar that contains a jet. X-ray observations of this object contain emission from both the jet and disc. Understanding both is key for understanding the geometry and physical parameters of this system and others like it (Madsen et al. 2015).

Mrk 335 showed evidence of a collimated corona that had beamed emission during its high flux state (Gallo et al. 2015). Wilkins & Gallo (2015) interpret the drastic changes in Mrk 335 as a failed jet launching event. The 2013 observation of Mrk 335 contained a significant flaring event. Before the flare the corona of Mrk 335 was extended. During the flare the corona became collimated and had beamed emission. When the flare ended the corona collapsed and Mrk 335 entered a lower flux state with a compact corona.

IZw 1 shows peculiar variability of the broad Fe  $K\alpha$  line which suggested the presence of two separate components of the corona: an extended corona that illuminated the distant disc, and a compact core that illuminated the inner regions of the disc (Gallo et al. 2007a; Gallo et al. 2007b). In follow up work, Wilkins et al. (2017) found two distinct reverberation lags. They interpret the longer lag to be from the extended corona covering the inner regions of the accretion disc and the shorter to originate in the compact core. The compact core can be interpreted as the base of a jet or an aborted jet, similar to Mrk 335. IZw 1 is a radio quiet object, which is consistent with the failed jet scenario. This object, along with Mrk 335, demonstrates the intimate connection between the central engine of AGN and radio jets that span the host galaxy. NLS1 are key objects needed to understand this connections between jets and the SMBH that power them.

## 1.4 This Work

NLS1 have been shown to be some of the most interesting and variable AGN. The nature of the corona (Sect. 1.2.1) and soft excess (sect. 1.2.2) are uncertain. Even in RQ-NLS1s there is the possibility that jet emission plays a role (Sect. 1.3.3). In this work we examine two AGN that are unusual (or ‘weird’) even by NLS1 standards, to determine the nature of the X-ray emission. WKK 4438 is a known  $\gamma$ -ray source that possess a weak soft excess and broad Fe  $K\alpha$  line. Mrk 1239 is highly absorbed, but exhibits a strong soft excess. Both AGN will be studied with new data from the *NuSTAR* observatory (Harrison et al. 2013) along with archival data.

### 1.4.1 Mrk 1239

Optical measurements of Mrk 1239 were part of Osterbrock & Pogge (1985) paper outlining the narrow line Seyfert properties. Véron-Cetty & Véron (2001) find the  $H\beta$  line of Mrk 1239 to be  $1075 \text{ km s}^{-1}$ , well with in the NLS1 classification. Mrk 1239 has a Galactic column density of  $4.43 \times 10^{20} \text{ atoms cm}^{-2}$  (Willingale et al. 2013). It is located at a redshift of  $z = 0.01993$  (Beers et al. 1995) and contains a black hole with mass  $2.4 \times 10^6 M_{\odot}$  (Marin 2016).

The optical spectra of Mrk 1239 contains a relatively high degree of polarization. In Marin (2016) it has the second highest degree of polarization of all the type I AGN in their sample. Goodrich (1989) showed that the level of polarization of the Balmer lines was higher than the forbidden lines in the optical spectra. This discrepancy indicates that the source of the emission for the Balmer and forbidden lines is different. Pan et al. (2021) show that the intrinsic polarization of Mrk 1239 is even higher than previously measured, with a median value of 11.6%. They suggest that Mrk 1239 is actually a type II object (e.g. absorbed with a NLS1 engine.).

Infrared measurements of Mrk 1239 reveal possible star formation regions. Using polycyclic aromatic hydrocarbon (PAH) as a tracer for star formation, a possible region was identified to be

no further than 400 pc from the nucleus with a star formation rate (SFR) of less than  $7.5 M_{\odot}/\text{yr}$  (Ruschel-Dutra et al. 2016).

It is uncommon for NLS1s to be radio loud or possess jets (Komossa et al. 2006). Mrk 1239 is a borderline RL source (Doi et al. 2015), behaving like both a RL (e.g. Berton et al. 2015) and RQ (Berton et al. 2018) object. It does show some evidence of jet activity. VLBA images of Mrk 1239 indicate the presence of non-thermal jet-like structures protruding from the central region of the galaxy. The emission from these jet-like structures does not have a stellar origin and thus must be from synchrotron emission from AGN jets (Doi et al. 2015).

In the X-ray band, Mrk 1239 has previously been observed with *ROSAT*, *XMM-Newton*, and *Suzaku*. The *ROSAT* observations showed that Mrk 1239 had a large photon index and was heavily absorbed (Rush & Malkan 1996). Grupe et al. (2004) analysed the 10 ks of *XMM-Newton* data, they also found a high photon index and high column density. They reported a feature at 0.9 keV and attributed it to Ne IX emission line, and proposed a super solar abundance of neon to account for the line strength. The *Suzaku* observation of Mrk 1239 has only been used in sample studies previous to this work being completed (e.g. Miyazawa et al. 2009; Fukazawa et al. 2011; Ricci et al. 2014; Liu et al. 2014). In this work we will make use of broadband data from *NuSTAR* which will provide information up to 30 keV for the first time.

## 1.4.2 WKK 4438

WKK 4438 (IGR J14552-5133) is a NLS1 located towards the Galactic centre in the southern sky and is several degrees away from the Great Attractor. Due to the proximity to the Zone Of Avoidance (ZOA), a region of high column density due to gas and dust from the Galactic centre, this object was not catalogued until the turn of the century. WKK 4438 lies at Galactic Longitude  $l = 321.7^{\circ}$  and Galactic latitude  $b = 6.7^{\circ}$  (Woudt & Kraan-Korteweg 2001) and has a significant amount of Galactic absorption  $4.34 \times 10^{21}$  atoms  $\text{cm}^{-2}$  (Willingale et al. 2013).

Malizia et al. (2008) give the width of the  $H\beta$  line to be  $\text{FWHM} = 1700 \text{ km s}^{-1}$  and the mass of the SMBH as  $2 \times 10^6 M_{\odot}$ . The redshift of WKK 4438 is  $z = 0.016$  (Masetti et al. 2006). In 2007 *Swift* XRT data confirmed the association of WKK 4438 and the  $\gamma$ -ray source IGR J14552-5133 (Landi et al. 2007).

WKK 4438 was first considered an AGN based on its flux in the 20-100 keV band. The flux was measured to be  $(2.4 \pm 0.5) \times 10^{-11} \text{ erg cm}^{-2} \text{ s}^{-1}$  and was obtained using *INTEGRAL* observations (Bassani et al. 2005). The presence of an AGN was confirmed using optical follow up observations by Masetti et al. (2006), who measured the tentative optical counterpart of IGR J14552-5133, LEDA 3076910. The  $H\beta$  and [O III] emission line strengths corrected for the Galactic absorption were measured at  $(1.5 \pm 0.1) \times 10^{-13}$  and  $(1.02 \pm 0.07) \times 10^{-13}$  atoms  $\text{cm}^{-2}$  respectively.

WKK 4438 was part of the *Swift* BAT survey (Tueller et al. 2010; Ajello et al. 2012; Baumgartner et al. 2013; Oh et al. 2018) and was observed in the optical/UV and X-ray/ $\gamma$ -ray bands. There have been limited infrared observations of this object (e.g. 2MASS Skrutskie et al. 2006; *HERSCHEL* Meléndez et al. 2014) and no radio observations to date.

In the X-ray, WKK 4438 is a well studied. Some evidence to suggests a possible Ultra-Fast Outflow (UFO) detected in the *Suzaku*, and *NuSTAR* X-ray spectra (Jiang et al. 2018). The reported outflow found at 9.8 keV had a velocity of  $v \sim 0.3c$ , assuming it originated from Fe XXV emission line at 6.97 keV. In addition, Ar XVIII  $\text{Ly}\alpha$  line was found at similar velocities. In Jiang et al. (2018), the lamppost geometry was used to describe the reflection spectra of WKK 4438. The inner radius of the disc was constrained to  $15_{-5}^{+8} r_g$ , and an over abundance of Fe ( $\sim 2.6 Z_{\odot}$ ) and Ar ( $\gtrsim 6 Z_{\odot}$ ) were required.

Since the publication of Jiang et al. (2018), new deeper *NuSTAR* observations have been obtained. We will use these new spectra that are sensitive up to 50 keV for a new analysis on the nature of the X-ray emission in WKK 4438.

## Chapter 2

# Uncovering the primary X-ray

# emission and possible starburst

# component in the polarized NLS1 Mrk

# 1239

*Note:* This chapter was published in September 2020 in the *The Astrophysical Journal*, Volume 902 Number 2, pg 118, in collaboration with Sophia G. H. Waddell, Luigi C. Gallo, Dirk Grupe, and S. Komossa.<sup>1</sup>

## 2.1 Introduction

Active Galactic Nuclei (AGN) are powered by supermassive black holes which are accreting material from their surroundings. AGN emit light across the entire electromagnetic spectrum and are typically variable at all wavelengths. Studying the X-ray emission from these objects

---

<sup>1</sup><https://iopscience.iop.org/article/10.3847/1538-4357/abb08a>

allows the characterisation of the innermost regions of the system, where extreme relativistic effects occur.

AGN are typically classified based on their viewing angle, where Seyfert 1 (type-1) AGN provide a direct view of the central engine, and Seyfert 2 (type-2) AGN are viewed through the cold, obscuring torus (Antonucci 1993). Seyfert 1 galaxies can then be further classified based on their optical properties, in particular, the full-width-half-maximum (FWHM) of the  $H\beta$  line. Narrow-line Seyfert 1 (NLS1) galaxies have FWHM less than  $2000 \text{ km s}^{-1}$ , while broad-line Seyfert 1 (BLS1) galaxies have FWHM greater than  $2000 \text{ km s}^{-1}$  (Osterbrock & Pogge 1985; Goodrich 1989). The narrower lines observed in NLS1s are typically explained by lower mass AGN which are accreting at a higher fraction of their Eddington limit (Pounds et al. 1995; Grupe et al. 2004; Komossa 2008).

The X-ray spectra of type-1 AGN is dominated by a power law. The origin of the power law is the X-ray emitting corona, a source of hot electrons located at some height above the black hole. UV seed photons from the accretion disc are Compton up-scattered in the corona and re-emitted as X-rays in the form of a power law. Many spectra also show evidence of a prominent emission line at  $\sim 6.4 \text{ keV}$ . This is typically attributed to Fe  $K\alpha$  emission from neutral iron, originating in the torus, a distant cloud of neutral gas and dust (e.g. Nandra et al. 2007). Above  $10 \text{ keV}$ , spectra show evidence for a Compton hump, peaking at  $20 - 30 \text{ keV}$ . This feature is produced via Compton down-scattering of photons from the corona in an optically thick medium, such as the torus or the accretion disc.

Below  $\sim 2 \text{ keV}$ , many Seyfert 1 AGN show a strong soft excess of disputed origin. This feature has been shown to be particularly prominent in NLS1 galaxies (e.g. Boller et al. 1996; Grupe et al. 1998; Puchnarewicz et al. 1992). One commonly adopted interpretation is the partial covering scenario, wherein the soft excess is produced via absorption of X-rays from the corona (e.g. Tanaka et al. 2004). The absorber is typically located close to the corona, and a number of

ionisation states, densities, and covering fractions of the absorbing material can be adopted to explain the observed emission. This interpretation has been used to model the observed spectra of numerous type-1 AGN (e.g. Miyakawa et al. 2012; Gallo et al. 2015).

An alternative interpretation is known as the blurred reflection scenario (e.g. Ross & Fabian 2005). In this model, some fraction of photons emitted by the corona are incident upon the accretion disc. As the photons interact with the disc, they produce strong emission and absorption features, most of which are associated with iron and have energies below  $\sim 2$  keV. As the disc rotates, the material is subject to extreme general relativistic effects, and the features appear broadened. This produces a strong soft excess, as well as a broadened Fe  $K\alpha$  line between 4 – 7 keV. This model has been successfully applied to the spectra of numerous NLS1 galaxies (Fabian et al. 2004; Ponti et al. 2010; Gallo et al. 2019).

When the continuum (power law) component is significantly suppressed, for whatever reason, the underlying components can often be distinguished. In dim sources, distant reflection from the torus and even X-ray emission from star formation in the galaxy can also contribute to the soft excess (e.g. Franceschini et al. 2003; Gallo et al. 2019; Parker et al. 2019). While the partial covering and blurred reflections typically produce smoother soft excesses, the torus and star formation regions lie far away from the central engine and are not subject to extreme relativistic effects. The emission and absorption features therefore appear narrow.

Mrk 1239 (RX J0952.3-0136) is typically classified as a NLS1 galaxy and is found at a redshift of  $z = 0.01993$  (Beers et al. 1995). The source has been studied at many wavelengths and numerous interesting properties have been revealed. The mass of the supermassive black hole at the centre of Mrk 1239 has been reported as  $2.4 \times 10^6 M_{\odot}$  (Marin 2016). Véron-Cetty & Véron (2001) measure a FWHM of  $1075 \text{ km s}^{-1}$  for the  $H\beta$  line, moderate [O III] emission strength ( $[O \text{ III}]/H\beta = 1.29$ ), and weak Fe II emission ( $[Fe \text{ II}]/H\beta = 0.63$ ). Additionally, the optical spectrum shows evidence for polarisation on the order of  $\sim 3 - 4\%$ , and has one of the



highest degrees of polarisation reported in Martin et al. (1983). Goodrich (1989) show that the Balmer lines and forbidden optical lines show different degrees of polarisation and suggest that these features have distinct physical origins, polarised due to dust reflection and transmission.

In the radio regime, Mrk 1239 has been classified as both radio-quiet (Doi et al. 2015), or borderline radio-loud (Berton et al. 2018). Doi et al. (2015) show that the radio emission cannot solely be attributed to starburst activity and must also comprise AGN jet activity. They classify this source as a Fanaroff-Riley Type I candidate (Fanaroff & Riley 1974), meaning that the radio luminosity decreases with increasing distance from the centre of the galaxy. Doi et al. (2015) also give clear evidence for kilo-parsec scale non-thermal radio emission attributed to AGN jets, however, most of the radio power is centred in the inner 100 pc.

Based on near-infrared observations, Mrk 1239 has some evidence for star forming regions based on signatures from polycyclic aromatic hydrocarbon (PAH). Ruschel-Dutra et al. (2016) and Jensen et al. (2017) both report signatures of PAH at  $11.3\mu\text{m}$ , although both suggest that these features do not lie in the inner nucleus, but rather a few hundred pc from the centre. Rodríguez-Ardila & Viegas (2003) place only an upper limit on a  $3.3\mu\text{m}$  PAH detection, also state that starburst activity may be occurring a few hundred pc from the nucleus. An estimated star formation rate (SFR) of less than  $7.5 M_{\odot}\text{yr}^{-1}$  (Ruschel-Dutra et al. 2016) has been measured. Sani et al. (2010) find that Mrk 1239 exhibits weaker star formation relative to AGN emission than the average NLS1. As well, Rodríguez-Ardila & Mazzalay (2006) reported a remarkable NIR bump, they interpret it as a massive reservoir of dusty gas between NLR and BLR. This could explain strong continuum absorption.

In the X-ray, observations with *ROSAT* and *XMM-Newton* have previously been analysed. Rush & Malkan (1996) report a soft X-ray slope of  $\Gamma \simeq 3$  using *ROSAT* and find absorption higher than the Galactic  $N_{\text{H}}$  value by a factor of  $\sim 1.5$ , indicating absorption in the host galaxy. Mrk 1239 is also included in the *ROSAT* sample analysed by Boller et al. (1996), where a steep

soft X-ray slope of 3.9 and a high column density of  $8.3 \times 10^{20} \text{ cm}^{-2}$  is reported. Grupe et al. (2004) report on a 10 ks *XMM-Newton* observation of Mrk 1239, using data from the EPIC-pn and MOS detectors. They find that the spectral shape can successfully be reproduced using a power law which is almost entirely absorbed by two distinct absorbers, akin to the two polarisation regions reported in Goodrich (1989). They also report a strong feature around 0.9 keV found in all three detectors, which they attribute to a strong Ne IX line due to a super-solar Ne/O ratio (Grupe et al. 2004).

This work presents the spectral and timing analysis of all available X-ray data from *XMM-Newton*, *Suzaku*, *NuSTAR* and *Swift*, spanning 18 years between 2001 and 2019, and seeks to explain the unique X-ray properties of the source. In Section 2.2, the observations and data reduction techniques are summarised. Section 2.3 examines the variability of the source across both long (years) and short (hours) timescales and in Section 2.4 the spectra are analyzed. A discussion of the results is given in Section 2.5, and conclusions are drawn in Section 2.6.

## 2.2 Observations and Data Reduction

Mrk 1239 was observed with *XMM-Newton*, *Suzaku*, and *NuSTAR/Swift* at three different epochs over 18 years. The data analysed here are listed in Table 2.1. This section describes the observations and data reduction.<sup>2</sup>

### 2.2.1 *XMM-Newton*

Mrk 1239 was observed with *XMM-Newton* (Jansen et al. 2001) for  $\sim 10$  ks in late 2001. The source appears in the field of view of the target source, RXJ 095208.7-014818, and is therefore substantially off axis.

---

<sup>2</sup>Note: X-ray telescopes generally will record the time, pixel position, and energy of each photon that arrives at the detector. This information is used to produce spectra and light curves.

(1)	(2)	(3)	(4)	(5)	(6)
Observatory	Observation ID	Name	Date	Exposure [s]	Energy Range [keV]
<i>XMM-Newton</i> MOS 1+2	0065790101	MOS	2001-11-12	9371	0.3-8.0
<i>Suzaku</i> XIS 0+3	702031010	XIS	2007-05-06	63128	0.7-1.5, 2.5-10
<i>Suzaku</i> PIN		PIN		50240	12-20
<i>NuSTAR</i> FPMA/B	60360006002	FPMA/B	2019-06-17	21093	3-30
<i>Swift</i> XRT	00081986001	XRT	2019-06-17	6216	0.5-7

Table 2.1: Observation log for Mrk 1239. The observations and instruments used for analysis are listed in column (1). The observation ID and labels used in this work are given in columns (2) and (3), respectively. The start date of each observation is given in column (4), in the format YYYY-MM-DD. The duration of each observation, total exposure time and total counts for each observation are given in columns (5), (6), and (7), respectively. The energy each observation were fit over is given in column (8). For *Suzaku* the combined counts from XIS0 and XIS3 are given (column 7). Similarly for *XMM-Newton* the combined counts from MOS1 and MOS2 is reported.

The *XMM-Newton* Observation Data Files (ODF) were processed to produce a calibrated event list using the *XMM-Newton* Science Analysis System, SAS v17.0.0. Examination of the background showed significant flaring in the EPIC-pn detector. A good time interval (GTI) was created and applied. Background flaring was not significant in the EPIC-MOS1 and MOS2 detectors.

For each detector, source photons were extracted from a circular region with a  $35''$  radius centred on Mrk 1239, and background photons were extracted from an off-source circular region with a  $50''$  radius on the same CCD. For the pn detector, single and double events were selected, while single to quadruple events were selected for the MOS detectors. The SAS tasks RMFGEN and ARFGEN were used to generate response files. *XMM-Newton* light curves were not examined due to the short length of the observation (10 ks).

The source and background spectra were binned with a minimum of 10 counts per bin. The final pn, MOS1 and MOS2 spectra were checked for consistency, and all spectra were found to

be comparable within known uncertainties.<sup>3</sup> The pn spectrum had low counts due to background flare filtering and the source was located at the very edge of the detector. For this reason, the combined MOS data are used for further analysis. The ungrouped MOS1 and MOS2 source and background spectra were merged using ADDSPEC, and the corresponding response files merged using ADDRMF and ADDARF. The combined source and background spectra were then binned with a minimum of 10 counts per bin. This combined MOS spectrum had a higher signal and lower background than the pn detector, allowing for improved spectral modelling. Data above 8 keV are background dominated so only the 0.3 – 8 keV range is used for spectral modelling.

### 2.2.2 *Suzaku*

Mrk 1239 was the target of a  $\sim 126$  ks *Suzaku* (Mitsuda et al. 2007) observation in May 2007. The data were taken in XIS nominal mode. Extraction of spectra and light curves was performed with XSELECT v2.4G using cleaned event files from the front illuminated (FI; XIS0 and XIS3) and back illuminated (BI; XIS1) CCDs.

For each instrument, source photons were extracted using a  $240''$  region centred around the source, while background photons were extracted from a  $180''$  off-source region, while avoiding the calibration regions in the corners of the CCDs. Response matrices for each detector were generated using the tasks XISRMFGEN and XISSIMARFGEN. Source and background spectra for each detector were then binned using the optimal binning routine in FTGROUPPHA (Kaastra & Bleeker 2016). The XIS spectra were checked for consistency and found to be comparable with one another. The XIS0 and XIS3 source and background spectra were then merged using ADDASCASPEC. For simplicity, only the merged FI spectra are presented for the remainder of the analysis. The XIS spectrum is modelled between 0.7- 10 keV, while excluding 1.5 – 2.5 keV due to calibration uncertainties.

---

<sup>3</sup><https://xmmweb.esac.esa.int/docs/documents/CAL-TN-0018.pdf>

Cleaned event files from the HXD-PIN detector were processed using the tool HXDPIXBPI, resulting in a 54 ks exposure. Both the non-X-ray background (NXB) and the cosmic X-ray background (CXB) are used to determine the background level. The source is detected at  $\sim 4.5$  per cent above the background between 12-20 keV, which is considered marginal (Fukazawa et al. 2009).

### 2.2.3 *NuSTAR* and *Swift*

Mrk 1239 is part the *NuSTAR* (Harrison et al. 2013) Extragalactic Legacy Survey, specifically the *NuSTAR* Local AGN NH Distribution Survey (NuLANDS). NuLANDS is designed to look at heavily obscured AGN in the local universe (Boorman et al. 2018). There are 30 AGN in the sample and observations were completed in 2019.

Mrk 1239 was observed in June 2019 with a simultaneous *Swift* observation shortly after *NuSTAR* began. FPMA and FPMB data were extracted from source region of 75". A background was selected from the same chip with a region of 115". The data were processed with CALDB index version 20181030. The joint *Swift* XIS spectrum was obtained from the *Swift*-XRT data product generator (Evans et al. 2009)<sup>4</sup>.

The *NuSTAR* data were optimally binned using FTGROUPPHA. The *Swift* spectra was binned to have a minimum of 10 counts per bin using GRPPHA.

## 2.3 Characterizing the Variability

### 2.3.1 Long term Variability

The unfolded spectra of Mrk 1239 compared to a flat ( $\Gamma = 0$ ) power law are plotted in Figure 2.1. Plotting the unfolded spectra in this way allows us to directly compare data from different in-

---

<sup>4</sup>[www.swift.ac.uk/user\\_objects/](http://www.swift.ac.uk/user_objects/)

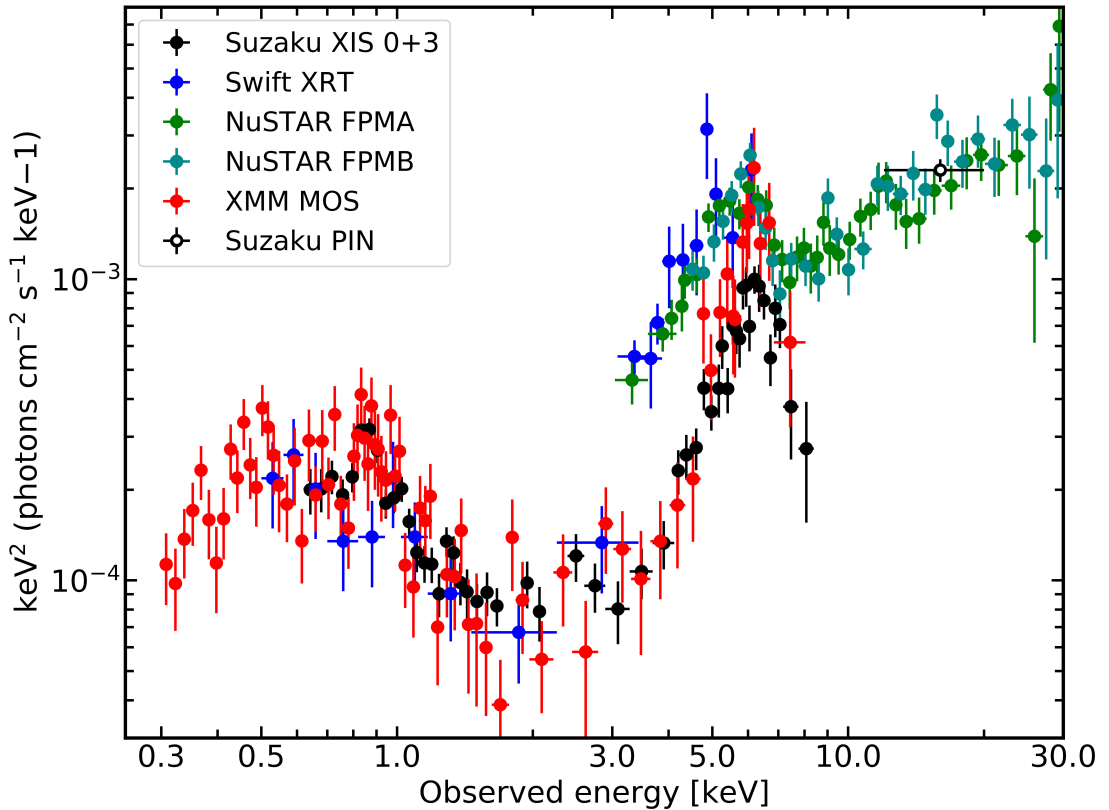


Figure 2.1: The unfolded spectra of Mrk 1239, with observations spanning 18 years. Data from *XMM-Newton* are shown in red, *Suzaku* are shown in black, *NuSTAR* are shown in green and aqua, and *Swift* are shown in blue. The data are compared to a flat power law with  $\Gamma = 0$ . The intrinsic spectrum is hard, and spectral changes are apparent in the 3 – 10 keV band.

struments<sup>5</sup>, highlighting any spectral differences at each of the three epochs.

The soft band (0.3 – 3 keV) is remarkably similar between epochs, displaying the same flux and curved spectral shape in the XRT, XIS and MOS spectra. The large hump like feature appears to be a soft excess. This feature has been consistently observed in this source outside the observations included in this paper. The source was also observed using *ROSAT* (Truemper 1982) in 1992. Rush & Malkan (1996) fit the source with an absorbed power law and found that was an acceptable fit. However the fit was improved using an additional component, either thermal emission (blackbody or Raymond-Smith thermal plasma<sup>6</sup>) or an emission line at  $\sim 0.7$  keV. The spectra lacked the data quality to distinguish between any of the models. An

<sup>5</sup>Unfolding the spectra in this manner removes the effects of detector area at different energies, allowing for a visual comparison of the data.

<sup>6</sup>See Raymond & Smith 1977

emission line-like feature at  $\sim 0.9$  keV was also reported by Grupe et al. (2004) in the EPIC-pn spectra. This feature is prevalent in all the data.

The most significant variability appears between 3 – 10 keV. The flux and spectral shape of the source is different in 2019 compared to the earlier XIS and MOS observations. In particular, the *NuSTAR* and *Swift* data are a factor of  $\sim 2 - 3$  brighter than the XIS and MOS data in this energy range. The MOS and XIS data are remarkably similar across the entire energy range. There is a slight discrepancy around  $\sim 6 - 7$  keV, where the MOS data appear slightly brighter; however, the spectra remain consistent within error.

The source is significantly detected in *NuSTAR* up to  $\sim 30$  keV. The source is only marginally detected in the PIN, but appears to be comparable in brightness at the two epochs (2007 and 2019). We cannot comment on any change in shape between epochs because the PIN data are limited.

### 2.3.2 Rapid variability

Having established that there is some long-term variability in the 3 – 10 keV band, we examine light curves for rapid variability over the course of the *NuSTAR* and *Suzaku* observations. The FPMA and FPMB lightcurves were merged to improve signal-to-noise, as were the XIS0 and XIS3 lightcurves. Variability was examined using 500 s and 5780 s bins, where 5780 s corresponds approximately to the orbital period of the satellites. The lightcurves were binned using LCURVE. Given the modest data quality, all lightcurves and hardness ratios are compared to their mean value to examine variability. The fit quality is given by a reduced  $\chi^2$  test. In Figure 2.2 and Table 2.2, the light curves and fits are presented.

The XIS lightcurve for the soft band (0.5–3 keV) has a mean count rate of  $\sim 0.05$  count  $s^{-1}$ . The  $\chi^2/dof$  for the light curves is 144/145 using the 500 s bins and 11/21 using the 5780 s bins. This indicates that the source is not variable below 3 keV on short time scales.

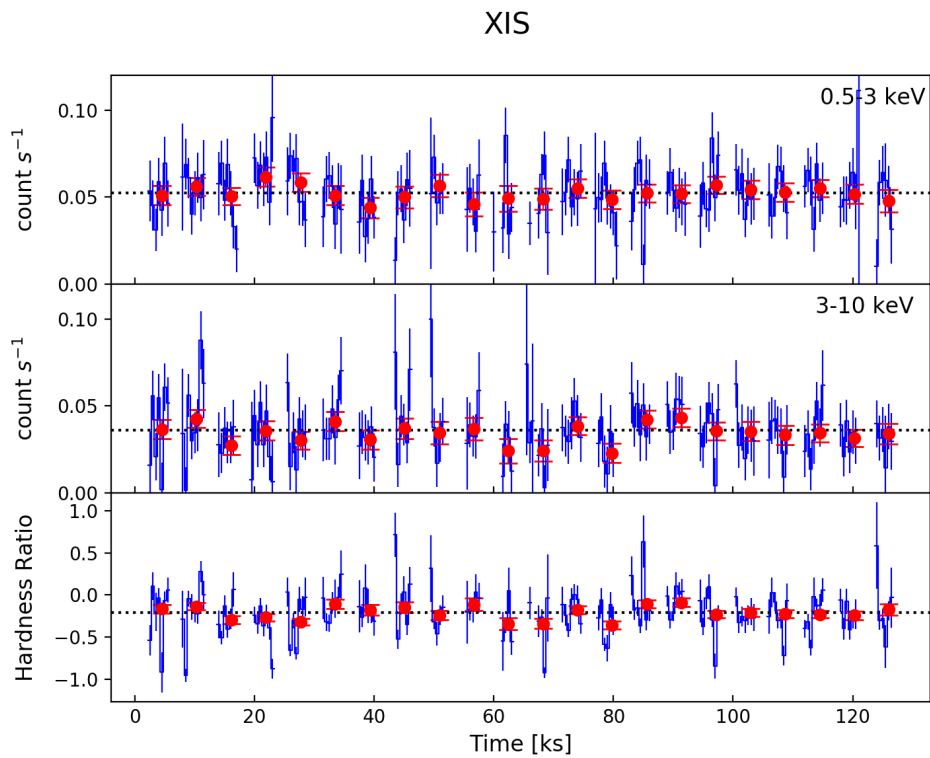
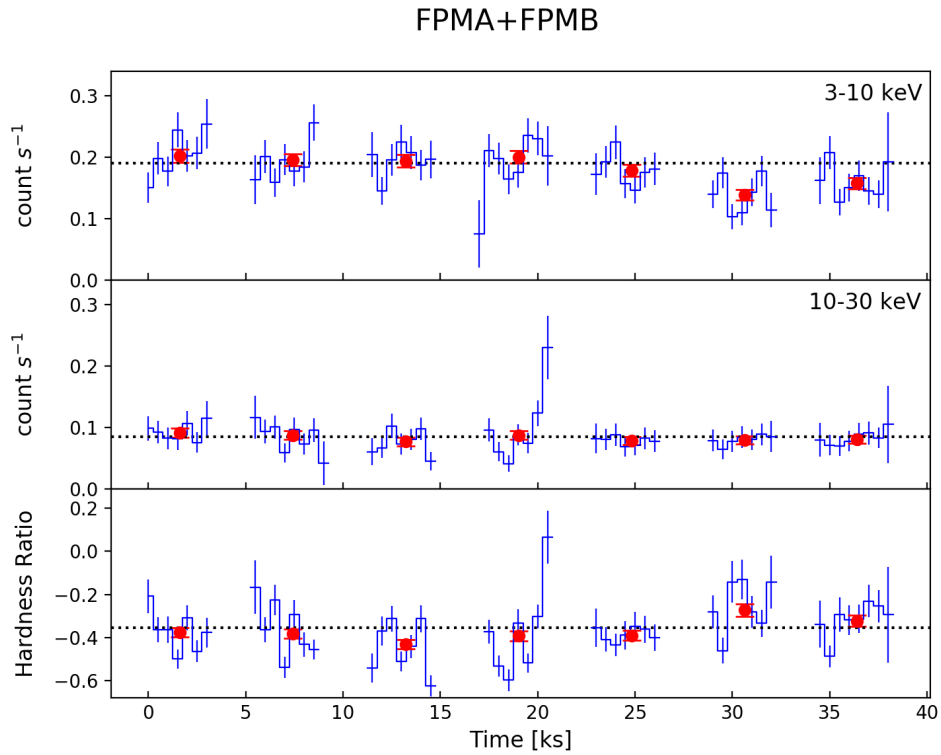


Figure 2.2: *FPMA+FPMB*: *NuSTAR* light curve with *FPMA* and *FPMB* combined. Top panel is the 3-10 keV band, middle is the 10-30 keV band and bottom panel is the hardness ratio calculated by:  $HR = (H - S)/(H + S)$ . *XIS*: *Suzaku* light curve. Top panel is the 0.5-3 keV band, middle is the 3-10 keV band and bottom panel is the hardness ratio. In all panels the dashed line is the average count rate or HR.



(1)	(2)	(3)	
Instrument	Energy band	$\chi^2/dof$	
		500 s	5780 s
FPMA+FPMB	3 – 10 keV	101/50	41/6
	10 – 30 keV	53/50	4/6
	HR <sub>FPM</sub>	198/49	25/6
XIS	0.5 – 3 keV	144/145	11/21
	3 – 10 keV	139/142	23/21
	HR <sub>XIS</sub>	658/139	52/21

Table 2.2: The fit statistic for each lightcurve and HR compared to their mean value. Column (1) indicates which instrument the light curve was produced by. Column (2) states the energy bin of the lightcurve. Column (3) gives the fit quality when the mean is fit for each light curve.

The hard band (10 – 30 keV) was only observed with *NuSTAR*, and has a mean count rate of  $\sim 0.1 \text{ count s}^{-1}$ . The  $\chi^2/dof$  of the 500 s and 5780 s bin lightcurves are 53/50 and 4/6, respectively. The slight difference in the  $\chi^2$  values may be the result of a flare in the 500 s bin lightcurve at approximately 20 ks. On short time scales, the hard band remains constant in flux within uncertainties

The intermediate band (3 – 10 keV) is the only band that has overlap between *NuSTAR* and XIS. In the XIS lightcurve the mean count rate is  $\sim 0.04 \text{ count s}^{-1}$ . The AGN is more significantly detected in *NuSTAR* and the mean count rate is  $\sim 0.2 \text{ count s}^{-1}$ . Upon visual inspection the intermediate band appears to have more variability compared to the soft and hard bands. This is confirmed in the constant fit test. The *NuSTAR* 500 s and orbital binned light curves are inconsistent with constants and have  $\chi^2/dof = 101/50$  and 41/6, respectively. The XIS data shows marginal variability (23/21) in the orbital binned lightcurve in this band and none in the 500 s bin lightcurve. However due to the low count rate it is difficult to rule out rapid variability in the XIS lightcurves.

The hardness ratio (HR) for the XIS lightcurves, HR<sub>XIS</sub>, has a mean value of  $\sim -0.2$ , indi-

cating that the soft count rate is higher than the intermediate count rate. The *NuSTAR*  $\text{HR}_{\text{FPM}}$  has a mean value of  $\sim -0.4$ , indicates the intermediate count rate is higher than the hard count rate. All HR curves are inconsistent with a constant fit ( $\chi^2/dof > 1$ ) indicating a significant amount of spectral variability. This spectral variability is driven by fluctuations in the intermediate, 3 – 10 keV, band. This is the same result found on long time scales (Figure 2.1). On both time scales there is very little change in the soft band, which remained constant in shape and flux. The intermediate band changes in shape and flux on long time scales as well as flux on rapid time scales.

The excess variance ( $\sigma_{\text{rms}}^2$ ) (e.g. Ponti et al. 2012) is calculated for the *NuSTAR* 3 – 10 keV light curve to further examine the rapid variability. The light curve is binned in 200 s and subdivided in 10 ks segments. The excess variance is calculated in each segment and then averaged over all of the segments. The measured average value for Mrk 1239 during the *NuSTAR* observation is  $\sigma_{\text{rms}}^2 = 0.04 \pm 0.01$ . The value is comparable to that measured in other NLS1 galaxies (Ponti et al. 2012).

Seyfert 1 AGN can display substantial variability at lower energies, and NLS1s in particular are known to display extreme soft variability on both short and long timescales (e.g. Boller et al. 1996; Leighly 1999b; Grupe et al. 2001; Nikolajuk et al. 2009; Grupe et al. 2010; Komossa et al. 2016; Bonson et al. 2018; Gallo 2018). The differences in the rapid and long term spectral variability may be pointing to different origins for the soft ( $< 3$  keV) and intermediate (3 – 10 keV) emission. This suggests that the primary source of the soft excess is highly atypical compared to other NLS1s. However, the variability above 3 keV seen on both short and long timescales is more typical of what is seen in other sources, implying a distinct origin from the soft excess. More discussion for this will be given in Section 2.5.

## 2.4 Spectral Modelling

All data were background modelled in XSPEC, except for the PIN data which was background subtracted. We used C-statistics (Cash 1979) to evaluate the fit quality throughout<sup>7</sup>. Errors were calculated at the 90 per cent confidence level using the XSPEC error comand. The *NuSTAR* and *Swift* spectra were treated as one epoch for all spectral modelling. All model parameters were linked between them. The same was done for the *Suzaku* XIS and PIN data. A cross-calibration constant was applied to the FPMB detector in *NuSTAR*, the XRT data from *Swift* and the PIN data from *Suzaku*. The constant was free for FPMB and XRT and monitored to ensure it remained within acceptable ranges, as prescribed by *NuSTAR* FAQ<sup>8</sup>. The constant applied to the PIN data was frozen at 1.18<sup>9</sup>. A Galactic column density of  $N_{\text{H}} = 4.43 \times 10^{20}$  atoms  $\text{cm}^{-2}$  (Willingale et al. 2013) was applied to all models and frozen throughout spectral fitting. Wilms et al. (2000) abundances were used throughout spectral fitting.

Figure 2.3 shows each spectra separately with its background model, and ratio for an absorbed power law with  $\Gamma = 2$  to represent a typical NLS1. As we can see in Figure 2.3, all spectra exhibit curvature and none are fit well by the power law. All five spectra show evidence for excess emission between 5 – 8 keV. The MOS spectrum shows a soft excess below 1 keV and all spectra are over estimated by the model in the 2 – 5 keV range.

### 2.4.1 *NuSTAR/Swift*

We begin by examining only the *NuSTAR* and *Swift* spectra, and only consider data above 2 keV. This is the first time this data set has been examined in detail and it provides the best view of the AGN above 10 keV. The examination of the unfolded spectrum reveals many key character-

---

<sup>7</sup>C-statistics are used as they utilize Poisson distributions allowing us to optimally bin our spectra for better spectral resolution.

<sup>8</sup>[https://heasarc.gsfc.nasa.gov/docs/nustar/nustar\\_faq.html](https://heasarc.gsfc.nasa.gov/docs/nustar/nustar_faq.html)

<sup>9</sup><https://heasarc.gsfc.nasa.gov/docs/suzaku/analysis/abc/node8.html> (See Sec. 5.7.2)

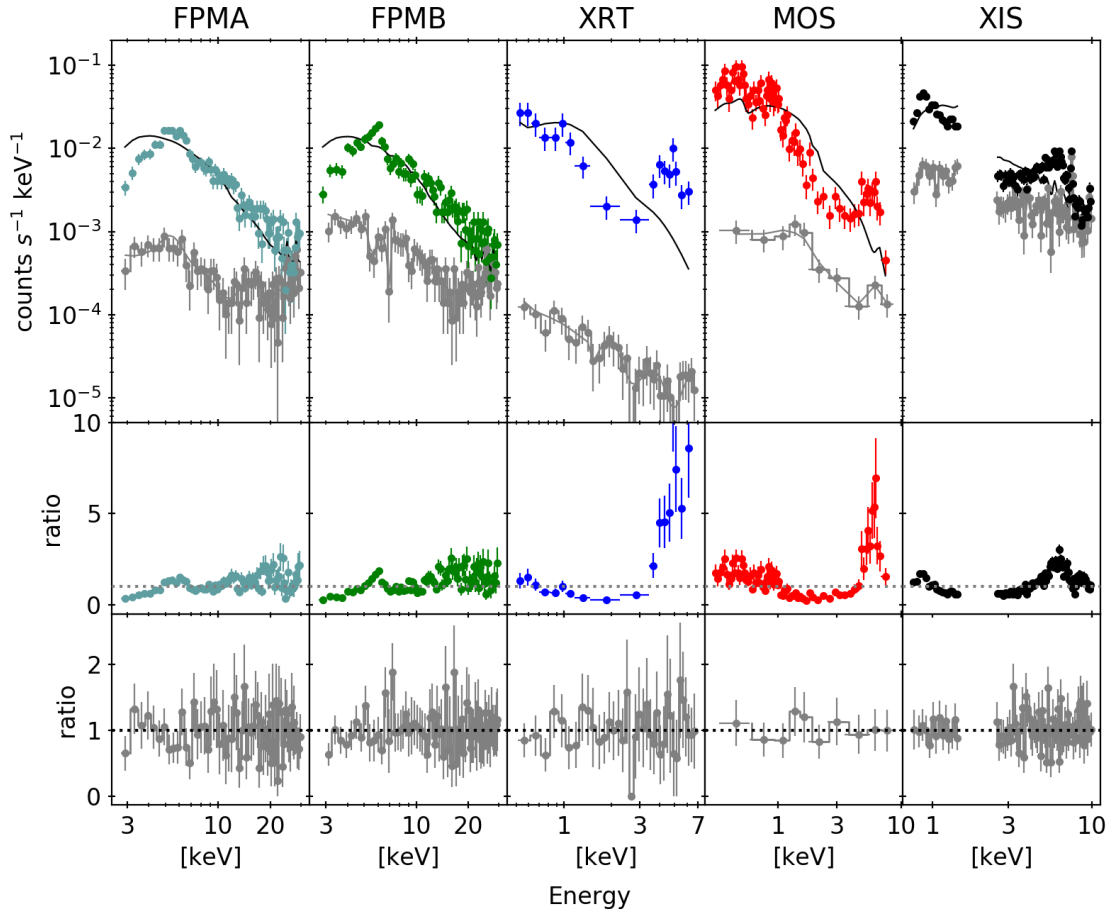


Figure 2.3: *Top row:* The folded source spectra for each instrument with the background shown in grey. The model, shown in black, is a power law with Galactic absorption, with  $\Gamma = 2$  and the normalization free for all instruments. This model was applied to emphasize the need for more complex models than a simple power law. *Middle Row:* The ratio of the data with the simple power law model. Comparison to the dotted line at ratio = 1 demonstrates the curvature in the data. *Bottom Row:* The ratio of the background to the background model, with ratio = 1.

istics; an underlying power law component, extreme spectral curvature around 3 – 8 keV, and a potential narrow feature at 6.4 keV. To model these features, we apply a power law plus a cold ( $\log \xi = 0$ ; where the ionisation parameter  $\xi = L/nr^2$  and  $L$  is the incident luminosity,  $n$  is the column density of the cloud, and  $r$  is the distance from the cloud to the illumination source), distant reflector representing reflection off the torus. To reproduce the observed spectral curvature we modify the power law with a single region of neutral absorption. The XSPEC model would appear as: `CONSTANT×TBABS×(XILLVER + ZPCFABS×PO)`. The constant is the cross calibration constant between FPMA and FPMB and *Swift*. This model was found to pro-

vide a suitable fit to the *NuSTAR* / *Swift* data in the 2 – 30 keV band, and gives a fit statistic of  $C/\text{dof} = 356.46/314$ <sup>10</sup>.

We extended the model and data down to 0.5 keV to see if this model is also capable of explaining the spectrum at low energies. This results in a much poorer fit ( $C/\text{dof} = 449.86/338$ ) and a large excess below approximately 1 keV. The addition of a second neutral partial covering component does not improve the fit quality, however the addition of an ionized partial covering absorber (ZXIPCF; Reeves et al. 2008) significantly improves the fit quality ( $C/\text{dof} = 324.03/335$ ). Despite the large change in the C-statistic, there remain significant residuals at approximately 1 keV, as were noted by Grupe et al. (2004). Additionally, all model fits give very high values of the absorber covering fraction ( $CF \sim 0.95 - 1$ ). It therefore seems possible that the intrinsic emission from the AGN is largely obscured below  $\sim 3$  keV, and appears only at high energies.

Based on the work of Ruschel-Dutra et al. (2016) in the mid-infrared, we can infer the existence of star forming regions in Mrk 1239 (see Section 2.1). Given the lack of evidence for variability at low energies, it is possible that the soft emission does not originate close to the central engine, but rather from star formation on extended scales. We therefore use MEKAL (Liedahl et al. 1995), collisionally ionised emission from hot diffuse gas, to model the SFR. We specify that MEKAL use abundances given by Wilms et al. (2000), with abundance frozen for all spectral fits. This improves the fit to  $C/\text{dof} = 307.92/333$ , and removes the residuals at 1 keV. The measured temperature is  $kT \approx 1$  keV.

Alternatively, we examine if the curvature and hard X-ray emission could be attributed to blurred reflection (e.g. Ross & Fabian 2005) rather than the ionized partial covering. By removing the ionized absorber and replacing it with a blurred reflection (RELXILL, García et al. 2014) one gets an acceptable fit with a simple blurred reflection model. A neutral partial cover-

---

<sup>10</sup>The dof is derived by XSPEC using the number of energy bins in the spectra and free parameters in the model.

ing component and MEKAL are still needed. Furthermore, the use of *NuSTAR* and *Swift* spectra alone does not allow for the constraint of many of the blurred reflection parameters. This model will be explored in more detail using additional data in Section 2.4.2.2.

## 2.4.2 Multi-epoch Spectral Modelling

In this section, we attempt to describe the behaviour of Mrk 1239 in a self consistent manner using the multi-epoch spectral data collected over 18 years. This has the advantage of giving us low energy sensitivity, provided by MOS and XIS, for the soft excess and the Fe  $K\alpha$  region. *NuSTAR* provides us with good energy coverage up to 30 keV, with simultaneous coverage between 0.5 and 7 keV from *Swift*. This allows us to simultaneously study the soft excess, Fe K region and the broadband continuum. We motivate the models used based on spectral features and variability on multiple time scales.

Structure around the neutral Fe  $K\alpha$  band seen in all spectra are suggestive of distant cold reflection, likely originating in the torus. For this we use XILLVER with  $\log\xi = 0$  to represent a cold reflector.

Study of the long term and rapid variability shows that there is negligible variability below 3 keV. This indicates that direct AGN continuum emission may be highly absorbed and thus not visible. There is structure seen in the MOS and XIS spectra that may be from distant optically-thin emission from star formation activity. We use MEKAL for this feature.

It also seems possible that the direct AGN component is revealed in the 3-10 keV band, but completely obscured below  $\sim 3$  keV. This indicates the presence of a partial covering absorber (ZPCFABS). We expand upon Section 2.4.1 by applying the ionized partial covering model and the blurred reflection model to all epochs. Some intrinsic properties of the system were linked, as they are not expected to change on timescales of years. This included the MEKAL component (both normalization and kT), the distant cold reflector (XILLVER) and some of the

blurred reflection parameters discussed in detail in Section 2.4.2.2.

Upon analysis of Figure 2.1 and fitting both models it was found that the *Suzaku* spectra closely followed the MOS spectra. Linking all parameters between *Suzaku* and MOS did not significantly decrease the fit quality for either physical model, so they are linked throughout the remainder of the analysis. Allowing for a free constant between the *XMM-Newton* and *Suzaku* models is not a significant improvement to the fit ( $\Delta C = 3$  for one additional free parameter). This leaves us with two epochs; a historic one containing *XMM-Newton* MOS, *Suzaku* XIS and PIN data, and a recent one containing the *NuSTAR* FPMA and FPMB and *Swift* XRT data.

### 2.4.2.1 Partial Covering

In a partial covering scenario a cloud of absorbing material with column density ( $N_{\text{H}}$ ) is positioned in the line of sight of the AGN, obscuring a fraction of the direct emission. The model has some fraction of its source emission absorbed and the rest is considered direct emission (e.g. Holt et al. 1980; Tanaka et al. 2004). The model includes three parameters: the column density ( $N_{\text{H}}$ ); the covering fraction (CF), which is the fraction of intrinsic emission that is absorbed; and the redshift ( $z$ ), which remains fixed at  $z = 0.01993$ . The direct emission can be either scattered off the clouds or let through patches in the absorbing material (Tanaka et al. 2004). The patchy absorber is often called a “leaky absorber” (Tanaka et al. 2003) as the direct emission photons can “leak” through the absorber.

Partial covering is often employed to fit NLS1s (e.g. Boller et al. (2002); Tanaka et al. 2005; Turner et al. 2007; Gallo et al. 2015; Iso et al. 2016; Grupe et al. 2019). For Mrk 1239, Grupe et al. (2004) use two absorbing components to model a leaky absorber with the EPIC-pn spectrum. A variation of partial covering is ionized partial covering, where the absorbing medium has some ionization. In this scenario the illumination source is the power law corona (e.g. Reeves et al. 2008).

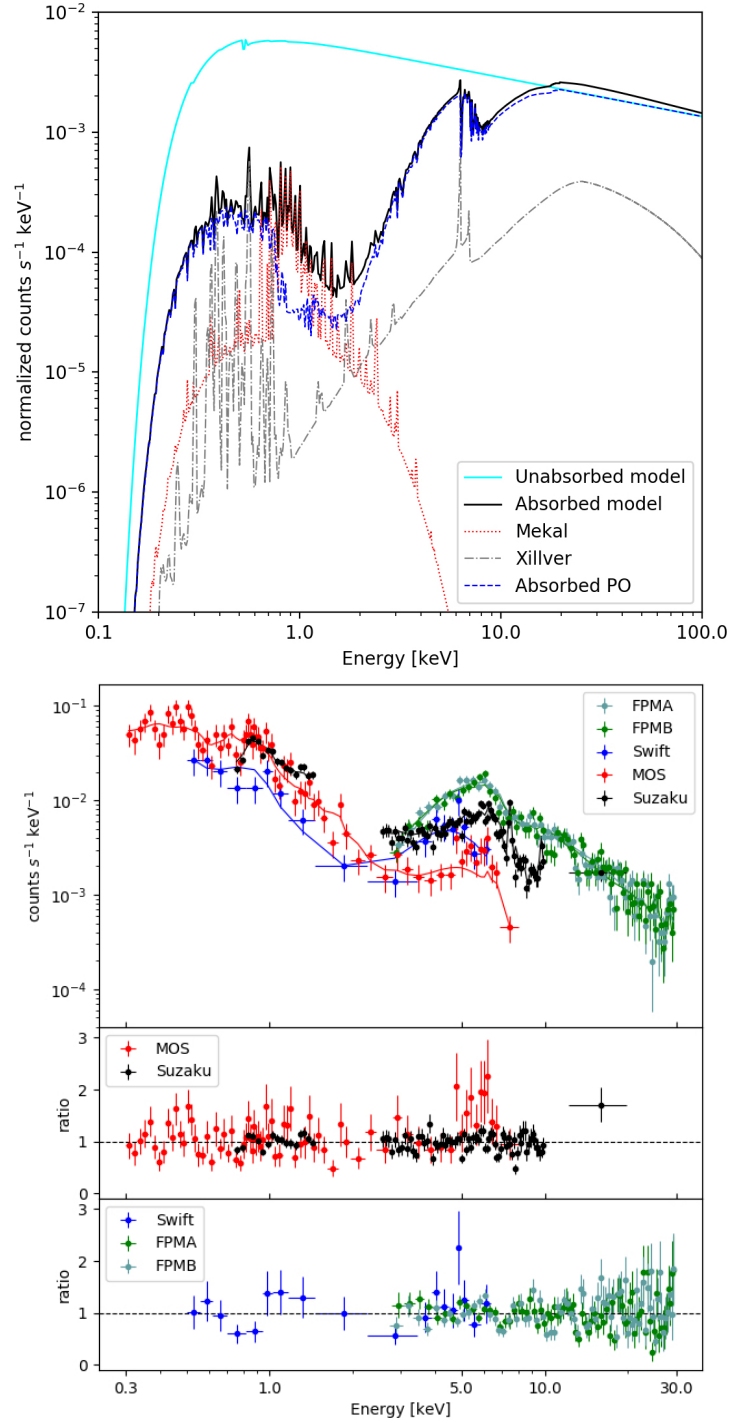


Figure 2.4: *Upper panel:* The theoretical best-fit ionised partial covering model shown over the entire X-ray band. The cyan line shows the continuum power law component with only Galactic absorption applied. *Upper middle panel:* The folded spectra with the best fit partial cover model applied to each data set. *Lower middle panel:* The ratio of data to model for the historic epoch, which includes the MOS, XIS and PIN spectra. *Lower panel:* The ratio of data to model for the modern epoch, which contains the XRT and FPMA/FPMB spectra.



We adopt a partial covering scenario assuming the absorbers are in a compact region and only the primary continuum (power law) source is absorbed. We include two absorbers, one that is neutral and one with some non-zero ionisation parameter. This is not necessarily two distinct absorbers, but could be representative of a ionisation and density gradient within one medium. The XSPEC model reads: `CONSTANT×TBABS(MEKAL + XILLVER + ZXIPCF×ZPCFABS×POWERLAW)`.

Three scenarios were tested to explain the variability between epochs: (i) constant power law and varying absorbers; (ii) constant absorbers and vary power law; and (iii) absorbers and power law free to vary. The continuum parameters were  $\Gamma$  and the power law normalization. The absorber parameters were both covering fractions (CF), both column densities ( $N_{\text{H}}$ ) and the cloud ionization ( $\log\xi$ ).

The initial model, with all parameters linked between epochs renders a very poor fit ( $C/\text{dof} = 1563.29/603$ ), and the cross-calibration constants for FPMB is far too large to be acceptable ( $\approx 1.7$ ). Allowing the absorber parameters free to vary (Test (i)), we obtain a significantly better fit. If the CF is free at each epoch the fit improves by  $\Delta C = 860.28$  for two additional free parameters. If we allow the  $\log\xi$  to be free between epochs as well the fit improves by  $\Delta C = 39.97$  for two additional free parameter. Allowing all absorber parameters to be free between epochs gives the best fit, with  $C/\text{dof} = 645.50/598$ .

Next, we test a variable continuum with a constant absorber (Test (ii)). Allowing just the power law normalization free between epochs (i.e. linked  $\Gamma$ ), the fit quality is  $C/\text{dof} = 850/602$ . Alternatively, permitting  $\Gamma$  to be free between epochs and the normalization linked, the fit quality improves by  $\Delta C = 38$ . If both the photon index and normalization are allowed free between epochs the  $C/\text{dof} = 764/601$ , an improvement of  $\Delta C = 48$  over the previous fit for one additional free parameter.

If all absorber and continuum parameters are allowed to vary between epochs (Test (iii)), the best fit is  $C/\text{dof} = 645.29/596$ , comparable to Test (i), where the power law parameters

are linked between epochs and absorber parameters are free to vary. The data and residuals (separated by epoch) can be seen in Figure 2.4. The best fit parameters can be seen in Table 2.3. The measured photon index is  $\Gamma \sim 2.3$ . Compared to Grupe et al. (2004), who reported  $\Gamma \approx 4$ , our value of  $\Gamma$  is in greater agreement with other NLS1s. This highlights the advantage of the high-energy sensitivity provided by *NuSTAR*. The covering fractions of the absorbers in both epochs are very high, each approximately 90 per cent covering. This is consistent with the high degree of optical polarization seen in Martin et al. (1983), and is consistent with the CF found in Grupe et al. (2004) of 0.995.

Figure 2.4 (top panel) shows the results for the best fitting model applied to only the FPMA data set for clarity. A number of interesting features are revealed. The intrinsic power law is shown in cyan, and the absorbed power law is shown in blue. This reveals that a large amount of absorption is required to reproduce the observed spectral curvature using this interpretation. This is sensible, as we measure covering fractions near 1. Given this high level of absorption at low energies, the MEKAL component (shown in red) is clearly visible in the total model (shown in dark blue). In particular, the strong 0.9 keV feature found by Grupe et al. (2004) is likely explained by this collisionally ionised plasma. This 0.9 keV feature is produced primarily by Fe L transitions. Contributions from the torus are shown in gray, and emission features at low energies also contribute to the soft excess.

The second panel of Figure 2.4 shows the folded spectrum along with the models for each instrument. The colours are the same as those used in Figure 2.1. The model appears to provide a good fit to the data. This is more evident in the bottom panels, where the residuals (data/model) are shown. While some excess residuals are present in the 5 – 7 keV band in the MOS data, the model is clearly able to explain the overall shape of the spectra at each epoch. In particular, no clear excess residuals are seen at low energies, suggesting that the starburst model provides a satisfactory fit to the data. Effectively, the long term variability in Mrk 1239 can be explained

largely by changes in a partial covering medium and a relatively constant power law. The excess residuals seen in the MOS data could be due in part to a poor fit of a blurred Fe  $K\alpha$  line suggesting a blurred reflection model must be examined.

(1)	(2)	(3)	(4)	(5)
Model	Model Component	Model Parameter	<i>Swift/ NuSTAR</i>	<i>MOS/ Suzaku</i>
Ionized Partial Covering	Ionized absorber ZXIPCF	nH ( $10^{22}\text{cm}^{-2}$ )	$64^{+37}_{-16}$	$114^{+31}_{-56}$
		$\log\xi$ [ergs cm s $^{-1}$ ]	$2.8^{+0.1}_{-0.2}$	$2.7^{+0.2}_{-0.4}$
		CF	$> 0.86$	$0.9 \pm 0.1$
	Neutral absorber ZPCFABS	nH ( $10^{22}\text{cm}^{-2}$ )	$13^{+10}_{-7}$	$60^{+19}_{-17}$
		CF	$0.96^{+0.03}_{-0.04}$	$0.89^{+0.04}_{-0.10}$
		Intrinsic	$\Gamma$	$2.3^{+0.3}_{-0.1}$
	Power Law	norm $^p$ ( $10^{-3}$ )	$6^{+4}_{-1}$	$5^{+4}_{-3}$
	FPMB Calibration	constant	$1.00 \pm 0.06$	
	Swift Calibration	constant	$1.0 \pm 0.2$	
	Collisionally Ionized material	kT [keV]	-	$0.66 \pm 0.03$
	MEKAL	norm ( $10^{-4}$ ) [cm $^{-5}$ ]	-	$1.3 \pm 0.1$
		Metal Abundance [cosmic]	$1^f$	
	Distant Cold Reflector	norm ( $10^{-5}$ )	-	$1.6 \pm 0.6$
	XILLVER	$A_{\text{Fe}}$ [solar]	$1^f$	
$\log\xi$ [ergs cm s $^{-1}$ ]		$0^f$		
$E_{\text{cut}}$ [keV]		$300^f$		
Inclination [ $^\circ$ ]		$30^f$		
Unabsorbed Flux	(0.1-100 keV)	$10^{-11}$ [ergs cm $^{-2}$ s $^{-1}$ ]	5.74	5.02
Observed Flux	(0.5-10 keV)	$10^{-11}$ [ergs cm $^{-2}$ s $^{-1}$ ]	0.289	0.137
Fit quality	C/dof			645.29/596

(1)	(2)	(3)	(4)	(5)
Model	Model Component	Model Parameter	<i>Swift/ NuSTAR</i>	<i>MOS/ Suzaku</i>
Blurred reflection	Neutral absorber	nH ( $10^{22} \text{cm}^{-2}$ )	$22 \pm 5$	$61 \pm 11$
	ZPCFABS	CF	$0.99 \pm 0.01$	$0.96^{+0.02}_{-0.01}$
	Intrinsic	$\Gamma$	$2.45^{+0.11}_{-0.14}$	$2.4 \pm 0.1$
	Power Law	norm ( $10^{-4}$ )	$< 22$	$< 18$
	FPMB Calibration	constant	$1.00 \pm 0.06$	
	Swift Calibration	constant	$1.0 \pm 0.2$	
	Collisionally Ionized material	kT [keV]	-	$0.65 \pm 0.04$
	MEKAL	norm ( $10^{-5}$ ) [ $\text{cm}^{-5}$ ]	-	$9 \pm 2$
		Metal Abundance [cosmic]	$1^f$	
	Distant Cold Reflector	norm ( $10^{-5}$ )	-	$2.1 \pm 0.06$
	XILLVER	$A_{\text{Fe}}$ [solar]	$1^f$	
		$\log \xi$ [ $\text{ergs cm s}^{-1}$ ]	$0^f$	
	$E_{\text{cut}}$ [keV]	$300^f$		
	Inclination [ $^\circ$ ]	$< 19^t$		
Blurred reflector	$q_{\text{in}}$		$3^f$	
RELXILL	$q_{\text{out}}$		$3^f$	
	Break radius [ $r_g$ ]		$6^f$	
	spin		$0.998^f$	
	Outer Radius [ $r_g$ ]		$400^f$	
	Inclination [ $^\circ$ ]		-	$< 19$
	$\log \xi$ [ $\text{ergs cm s}^{-1}$ ]		-	$3.00^{+0.07}_{-0.25}$
	$A_{\text{Fe}}$ [solar]		-	$4^{+2}_{-1}$

(1)	(2)	(3)	(4)	(5)
Model	Model Component	Model Parameter	<i>Swift/ NuSTAR</i>	<i>MOS/ Suzaku</i>
		$E_{\text{cut}}$ [keV]	$300^f$	
		norm ( $10^{-5}$ )	$10_{-5}^{+6}$	$4 \pm 1$
Unabsorbed Flux	(0.1-100 keV)	$10^{-11}$ [ergs $\text{cm}^{-2}$ $\text{s}^{-1}$ ]	9.85	4.32
Observed Flux	(0.5-10 keV)	$10^{-11}$ [ergs $\text{cm}^{-2}$ $\text{s}^{-1}$ ]	0.289	0.134
Fit quality	C/dof			615.64/598

Table 2.3: Best-fit model parameters for Mrk 1239. Column (1) indicated the tested model and column (2) indicates the model component. Column (3) gives the value of each parameter for the modern epoch. Column (4) gives the value for each parameter for the historic epoch. If a dash is present it indicated that the parameters are linked between epochs. All parameters with the superscript ‘*f*’ are kept fixed at quoted values. The parameters with superscript ‘*l*’ are linked between components. Normalizations with superscript ‘*p*’ are given by photons  $\text{keV}^{-1}\text{cm}^{-2}\text{s}^{-1}$  at 1 keV.

### 2.4.2.2 Blurred Reflection

While there is a high degree of absorption in Mrk 1239, the variability in the 3 – 10 keV band suggests we may be probing emission from the inner black hole region. Consequently, we examine if it is possible to model the intrinsic emission with a combination of power law and blurred reflection as has been done in some other highly absorbed, type II systems (e.g. Walton et al. 2019).

In blurred reflection, photons emitted by the corona are then incident on the accretion disk where they are absorbed and re-emitted via fluorescence (e.g. Ballantyne et al. 2001; Ross & Fabian 2005). This reflected spectrum is then subject to the general relativistic effects that are at play in accretion discs near black holes (e.g. Miniutti & Fabian 2004). Blurred reflection has been successful in describing the spectral and timing properties of NLS1s (e.g. Fabian et al. 2009; Chiang et al. 2015; Gallo et al. 2012, Gallo et al. 2015; Jiang et al. 2019; Waddell et al. 2019).

Here, the blurred reflection model, RELXILL (García et al. 2014), replaces the ionized absorber in the partial covering scenario above. Given the data quality, the initial approach is rather conservative. The illumination pattern as a function of distance ( $r$ ) on the disc (emissivity profile) is described by a power law ( $\propto r^{-q}$ ) with index  $q$ . For simplicity,  $q = 3$ , implying the primary emitter is radiating isotropically. The cut off energy ( $E_{cut}$ ) is frozen at 300 keV, as Mrk 1239 shows no evidence for a high energy cut off. The photon index is linked to the index of the primary power law component. The inner radius is fixed at the inner most stable orbit (ISCO) and the outer radius is fixed at  $400 r_g$ . The dimensionless spin parameter, defined by  $a = cJ/GM^2$  where  $M$  is the black hole mass and  $J$  is the angular momentum, can take on values of 0 (non spinning) to 0.998 (maximum spin). The spin is linked between epochs and initially frozen at 0.998, given the complexities in measuring this parameter (e.g. Bonson & Gallo 2016). The inclination is linked with that of XILLVER, which describes the cold distant reflector

(i.e. torus). It is linked between epochs, but left free to vary. The disc ionization parameter ( $\log\xi$ ) and the iron abundance ( $A_{\text{Fe}}$ ) are free to vary, but also linked between epochs.

We adopt very similar geometry as the partial covering model, where the very central region of the AGN is highly obscured, there is some amount of cold distant reflection and a star forming region at some large distance from the AGN. The XSPEC model used is `CONSTANT×TBABS×(MEKAL + XILLVER + ZPCFABS×(RELXILL + POWERLAW))`. As in the partial covering model we test three scenarios: (i) constant continuum and varying absorbers; (ii) constant absorbers and varying continuum; and (iii) continuum and absorber parameters free to vary. Here, continuum refers to the power law and blurred reflection components together.

The initial model, with all parameters linked between epochs renders a very poor fit ( $C/\text{dof} = 1538/603$ ). Examining Test (i), if the CF was allowed to vary between epochs the the fit statistic improves by  $\Delta C = 842$  for two additional free parameter. If instead  $N_{\text{H}}$  is allowed to vary between epochs and CF is linked, the improvement to the fit is  $\Delta C = 45$ . With both  $N_{\text{H}}$  and CF free between epochs the  $C/\text{dof} = 645/599$ .

In Test (ii), we linked absorbers and freed the continuum. If RELXILL normalization was free, but linked between epochs, the fit statistic is  $C/\text{dof} = 720/602$ . If instead the power law normalization was linked, but free to vary between epochs, there was no significant improvement in fit statistic. If both the RELXILL and power law normalization are allowed free to vary between epochs the fit statistic is  $C/\text{dof} = 680/601$ .

Test (iii) renders the best fit blurred reflection model. The parameters are given in Table 2.3. The best fit blurred reflection model gave a fit statistic of  $C/\text{dof} = 616/598$ . This was a marked improvement over linking the continuum or absorption parameters separately. The reflection fraction at each epoch was calculated by determining the unabsorbed flux contributions between 0.1 – 100 keV in the blurred reflector (RELXILL) and power law components. Error on the calculated reflection fraction are propagated from the uncertainties in the normalisation of each



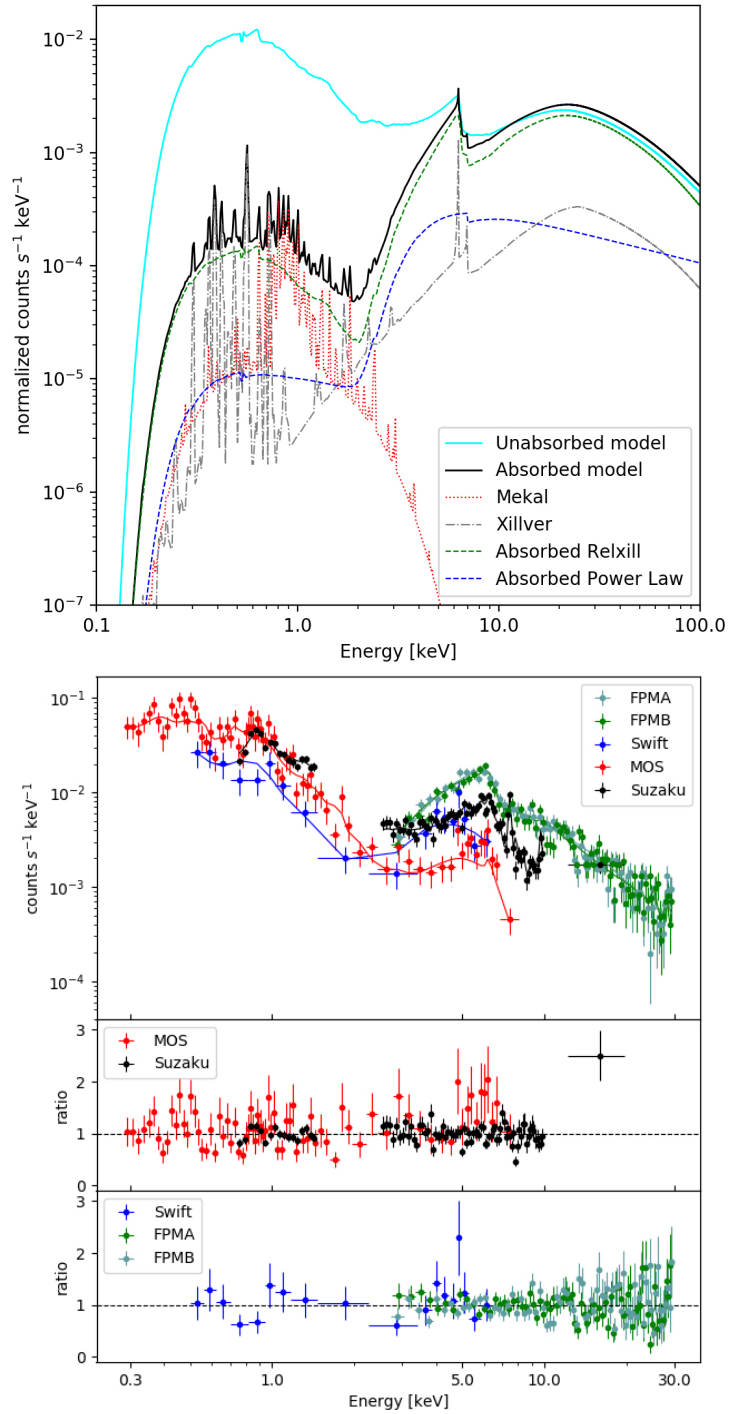


Figure 2.5: *Upper panel:* The theoretical best-fit blurred reflection model shown over the entire X-ray band. The cyan line shows the continuum power law and blurred reflector components with only Galactic absorption applied. This model appears to be reflection dominated. *Upper middle panel:* The folded spectra with the best fit blurred reflection model applied. *Lower middle panel:* The ratio of data to model for the historic epoch, which includes the MOS, XIS and PIN spectra. *Lower panel:* The ratio of data to model for the modern epoch, which contains the XRT and FPMA/FPMB spectra.

component. Only a lower limit could be calculated at both epochs, as only an upper limit could be placed on the power law flux. The reflection fraction for the *NuSTAR* epoch is  $> 2.5$ , for the MOS epoch  $> 1.3$ , so the model indicates the source is reflection dominated.

Only an upper limit could be measured for the inclination ( $< 19^\circ$ ) indicating the system is nearly face-on. Zhang & Wu (2002) measure an inclination of  $7^\circ$  from the broadline region, which is in good agreement with our measurement.

Figure 2.5 (top panel) shows the theoretical best fit blurred reflection model applied only to the FPMA data set for clarity. The intrinsic continuum is shown in cyan, the absorbed power law and blurred reflection component are shown in blue and green, respectively. This again shows the large amount of absorption that is required for the MEKAL (red) component to be visible. As in the ionized partial covering model, we believe that the MEKAL is responsible for the 0.9 keV feature reported by Grupe et al. (2004). The torus emission is shown in gray and further contribute to the soft excess. The bottoms three panels of Figure 2.5 show the data and residuals (separated by epoch) for the best fit blurred reflection model, the colours are the same as Figures 2.1 and 2.4. The fit has the same overall shape as the ionized partial cover model. We still see the residuals in the Fe  $K\alpha$  band of the MOS spectra despite the fact that our model requires an over abundance of iron, which is commonly seen in NLS1. Over all the data fits well, and the soft band is again adequately described by the MEKAL component, and the long term variability is again driven by changes in the absorber.

## 2.5 Discussion

The data of Mrk 1239 analysed in this work highlight distinct physical process that dominate above and below  $\sim 3$  keV. These two regimes feature dramatically different variability properties and physical origins. As such our discussion shall be divided into these two energy regimes.

We interpret the spectra of Mrk 1239 to contain two distinct sources of emission, the first is the low energy star forming region and the second is the higher energy AGN component.

### **2.5.1 Origins of the soft excess**

To begin, our analysis of the Suzaku data did not give any evidence for variability below 3 keV on short timescales. The unfolded spectra of Mrk 1239 showed a remarkable consistency over the 18 years of spectra coverage presented in this paper, with virtually no change in flux in the 0.3-3 keV while the harder band had significant change in flux over the same period. This is at odds with typical NLS1 where the soft band tends to have more variability (e.g. Leighly 1999a). As well, the spectral features present in the soft band, like the strong emission line-like features observed by Grupe et al. (2004), are inconsistent with smooth spectra typically seen in NLS1s.

The long-term consistency of Mrk 1239 along with its unusual spectral shape lead us to apply different models to explain the soft excess. We use MEKAL to model the possible contribution from starburst activity that may be present in Mrk 1239 (Rodríguez-Ardila & Viegas 2003). This model has been used to describe many AGN that exhibit depressed power law emission from obscuration (e.g. Franceschini et al. 2003) or intrinsic variability like Mrk 335 (e.g. Gallo et al. 2019). In AGN dominated flux states, this component is still present, but overwhelmed by the AGN emission.

There is also a contribution to the line emission at low energies from the distant reflector (Figure 2.4 and 2.5). In combination, the MEKAL and XILLVER components nicely describe the line-like features in the spectra without requiring additional Gaussian profiles or abnormal abundances. We considered the possibility that the emission could be due entirely to photoionized gas, perhaps from the narrow-line region. We tested this by replacing MEKAL with a PHOTEMIS component to our best fit ionized partial covering model for just the MOS spectra between 0.3 – 2 keV. The model was only applied to the MOS spectra as it is computationally intensive.

If there were any improvements over MEKAL, they would be most obvious in the the MOS spectra. The best fit PHOTEMIS model resulted in a poorer fit than with MEKAL ( $\Delta C = 30$ ) for the same number of free parameters, and positive residuals in the 0.8 – 1 keV band remained.

Table 2.4 show the flux and luminosity for each component between 0.5 – 2 keV at each epoch. We can see that the MEKAL component has a consistently strong contribution in both models with the central engine absorbed. But when the central engine absorption is removed, the line-emission MEKAL is completely overwhelmed by the power law contribution in the partial covering scenario and by the power law and RELXILL contribution in the blurred reflection scenario.

(1)	(2)	(3)	(4)	(5)	(6)	(7)
Model	Instrument	Component	Absorbed Flux [ergs cm <sup>-2</sup> s <sup>-1</sup> ]	Absorbed Luminosity [ergs s <sup>-1</sup> ]	Unabsorbed Flux [ergs cm <sup>-2</sup> s <sup>-1</sup> ]	Unabsorbed Luminosity [ergs s <sup>-1</sup> ]
Blurred Reflection	<i>Swift/NuSTAR</i>	Power Law	$2.20 \times 10^{-14}$	$1.98 \times 10^{40}$	$1.88 \times 10^{-12}$	$1.71 \times 10^{42}$
		Relxill	$17.0 \times 10^{-14}$	$15.6 \times 10^{40}$	$1.52 \times 10^{-11}$	$1.40 \times 10^{43}$
		Xillver	$7.39 \times 10^{-14}$	$6.73 \times 10^{40}$	$9.36 \times 10^{-14}$	$8.55 \times 10^{40}$
		Mekal	$11.6 \times 10^{-14}$	$10.5 \times 10^{40}$	$1.30 \times 10^{-13}$	$1.17 \times 10^{41}$
	<i>MOS/Suzaku</i>	Power Law	$6.13 \times 10^{-14}$	$5.53 \times 10^{40}$	$1.85 \times 10^{-12}$	$1.67 \times 10^{42}$
		Relxill	$19.6 \times 10^{-14}$	$18.0 \times 10^{40}$	$6.13 \times 10^{-12}$	$5.64 \times 10^{42}$
		Xillver	$7.18 \times 10^{-14}$	$6.48 \times 10^{40}$	$9.10 \times 10^{-14}$	$8.23 \times 10^{40}$
		Mekal	$11.6 \times 10^{-14}$	$10.5 \times 10^{40}$	$1.30 \times 10^{-13}$	$1.18 \times 10^{41}$
Partial Covering	<i>SwiftNuSTAR</i>	Power Law	$16.1 \times 10^{-14}$	$14.9 \times 10^{40}$	$1.38 \times 10^{-11}$	$1.25 \times 10^{43}$
		Xillver	$4.97 \times 10^{-14}$	$45.1 \times 10^{40}$	$6.25 \times 10^{-14}$	$5.70 \times 10^{40}$
		Mekal	$17.0 \times 10^{-14}$	$15.3 \times 10^{40}$	$1.90 \times 10^{-13}$	$1.71 \times 10^{41}$
	<i>MOS/ Suzaku</i>	Power Law	$22.5 \times 10^{-14}$	$20.6 \times 10^{40}$	$1.21 \times 10^{-11}$	$1.09 \times 10^{43}$
		Xillver	$4.86 \times 10^{-14}$	$43.8 \times 10^{40}$	$6.12 \times 10^{-14}$	$5.53 \times 10^{40}$
		Mekal	$17.0 \times 10^{-14}$	$15.3 \times 10^{40}$	$1.90 \times 10^{-13}$	$1.72 \times 10^{41}$

Table 2.4: Flux and luminosity for each model component between 0.5 – 2 keV. Column (1) indicates the model used for the measurements. Columns (2) and (3) denotes the instrument used/the epoch and the model component measured respectively. Columns (4) and (5) list the absorbed flux and luminosity between 0.5 – 2 keV. Columns (6) and (7) list the unabsorbed flux and luminosity between 0.5 – 2 keV. There are small discrepancies in the flux and luminosity measured between epochs in the same model even though the xillver component are shared between epochs. This is due to the differences in telescope responses.

We are using MEKAL to describe the X-ray evidence of starburst activity. Mrk 1239 has significant evidence of starburst activity. The PAH signatures found by Rodríguez-Ardila & Viegas (2003) agrees with this interpretation. The starburst regions are included in the X-ray extraction regions of the instruments used due to the modest angular resolution.

A study of ten ultraluminous infrared galaxies (ULIRGs) by Franceschini et al. (2003) used MEKAL to model the SFR in selected galaxies. They measured the average temperature of the MEKAL component to be  $kT \approx 0.7 \text{ keV}$  which agrees exactly with the temperature measured in Mrk 1239 ( $kT \approx 0.66 \text{ keV}$ ). The luminosity we measure for the MEKAL component also agrees with the luminosity Franceschini et al. (2003) measured in their sample.

Franceschini et al. (2003) also give a method to approximate the SFR using  $L_{2-10 \text{ keV}}$ :

$$\text{SFR}_{\text{X-ray}}^{\text{ULIRG}} \approx \frac{L_{2-10 \text{ keV}}}{10^{39} \text{ erg s}^{-1}} \text{ M}_{\odot} \text{ yr}^{-1} \quad (2.1)$$

If we measure the  $L_{2-10 \text{ keV}}$  for just the unabsorbed MEKAL component we get a SFR of 5.8 and  $3.7 \text{ M}_{\odot} \text{ yr}^{-1}$  based on the ionized partial cover and blurred reflection model respectively. This agrees nicely with the SFR predicted by the PAH signatures (Ruschel-Dutra et al. 2016).

Another interesting feature of MEKAL component is that it appears to be independent of the continuum model tested. The MEKAL temperature and normalization agree with each other to within 1 and  $2\sigma$ , respectively. This suggests that regardless of the mechanism producing the observed curvature at high energies, the soft X-ray emission of Mrk 1239 can be nicely explained by the starburst component and some photoionised emission from distant emission, without the need for significant overabundances of Ne or other elements. We found that the spectral feature Grupe et al. (2004) reported as a Ne overabundance was a blend of many Fe L transitions. We examined if adopting different cosmic abundances in XSPEC could alter the fit quality. Regardless of the abundance table used, the MEKAL temperature remained between

0.63 – 0.65 keV and the fit quality was  $C = 162 - 167$  for 165 dof.

### 2.5.2 The hard X-ray spectrum of Mrk 1239

The light curves seen in Figure 2.2 show rapid variability between 3 – 10 keV. Similarly, the multi-epoch spectra in Figure 2.1 suggest long term variability between 3 – 10 keV. In Section 2.3.2, the excess variance in the *NuSTAR* light curve was calculated and determined to be  $\sigma_{\text{rms}}^2 = 0.04 \pm 0.01$ . With the caveats that our analysis uses slightly different energy bands and time bins, the measured value of  $\sigma_{\text{rms}}^2$  for Mrk 1239 is comparable to the average value Ponti et al. (2012) measured for NLS1s ( $\sigma_{\text{NLS1}}^2 \approx 0.02$ ). Following the  $M_{\text{BH}}-\sigma_{\text{rms}}$  relation found by Ponti et al. (2012), we estimate a black hole mass of  $2 \times 10^6 M_{\odot}$  for Mrk 1239, which is in agreement with other works (see Ryan et al. 2007). Based on the rapid variability in the 3 – 10 keV band, Mrk 1239 behaves like an unobscured NLS1. The central black hole region is exposed in the 3 – 10 keV band.

Independent of the scenarios tested (i.e. partial covering or blurred reflection), the photon index of the intrinsic power law component is comparable ( $\Gamma \sim 2.3$ ). The measured value is much flatter than has been measured in other works (Grupe et al. 2004), but it is more consistent with what is expected from Seyfert galaxies and NLS1s (Grupe et al. 2010). Estimating the Eddington luminosity ratio from  $\Gamma$  based on the relationship in Brightman et al. (2013) gives  $L/L_{\text{Edd}} \sim 1 - 1.5$  for Mrk 1239. This is consistent with the value estimated by Yao et al. (2018). The high value implies a rapid accretor, which is also characteristic of the NLS1 class. Alternatively, the value could be overestimated if the primary emission is anisotropic, which might be consistent with the jet interpretation for some of the radio emission (Doi et al. 2015).

Comparing the partial covering and blurred reflection scenarios directly, similar neutral absorbers that are responsible for obscuring the low energy X-rays and revealing the starburst regions are required in both models. In both models the column density decreases between the

historic and modern epochs. The main difference in the two scenarios is the strength of the primary power law. In the blurred reflection scenario the spectra are extremely reflection dominated with the reflection fraction  $> 1.3$  and  $> 2.5$  for the historic and modern epoch, respectively. The reflection dominated interpretation may be at odds with the value of the emissivity index being fixed to  $q_{\text{in}} = 3$  (allowing it to be free did not improve the fit), which would imply an inner disk that is truncated at a large radius or a corona that is very high above the disc. A high reflection fraction requires a significant amount of light bending or a non-standard geometry for the accretion disc.

Though it appears clear that we are observing emission originating close to the black hole, it is difficult to produce a self-consistent blurred reflection model with the current data. The ionized partial covering scenario has the advantage of being consistent with the high levels of polarization seen in the optical band by Martin et al. (1983) and Goodrich (1989).

In both of the scenarios, the primary emission variability is minimal on long timescales. The change in flux above 3 keV observed on long timescales is driven by the absorbers. A possible explanation for the large amount of absorbing material surrounding the AGN could be that it contains a Schwarzschild black hole. According to Ishibashi (2020), non-spinning black holes have less radiation pressure to drive obscuring gas and dust out of our line of sight than Kerr black holes do. The best fit blurred reflection model with  $a = 0$  results in a fit of  $C/\text{dof} = 625.50/598$ . Most fit parameters remained similar to the values we report in Table 2.3, except for the iron abundance which decreases to  $A_{\text{Fe}} = 2.2$ . Although the fit is not as good as that produced by the Kerr black hole model, a non-spinning black hole is more consistent with the low emissivity profile that is adopted.

Figure 2.6 show a diagram for the physical scenario we propose. The top box shows the physical scenario for the ionized partial covering model. Here photons are emitted by the disc in the UV and are Compton-upscattered by the corona. The primary X-ray photons are then



emitted by the corona, where they encounter the partial covering components. This includes a neutral partial cover and an ionized partial cover (warm absorber). In our model most of the photons interact with the absorbers, and few escape the inner region unaffected. This is due to the high CF we measure. The bottom of the two boxes show the AGN for the blurred reflection scenario. Here UV photons are produced by the disk, Compton-upscattered by the corona and then reflected off of the disc. Both the primary and blurred reflected emission are absorbed by a neutral absorber before leaving the AGN. Once we move out to the torus our diagrams for the ionized partial cover and blurred reflection scenario are the same. The photons from the AGN interact with the torus to give us cold distant reflection emission lines. Then our collisionally ionized material, which we believe is starburst activity and therefore must be located within 400 pc of the central engine as PAH measurements show starburst activity here (Ruschel-Dutra et al. 2016). Outside of the starburst region we see no evidence of further emission in the X-ray band. Alternatively the cold absorber could be associated with the torus. Perhaps our line-of-sight is grazing the torus or the torus is more patchy and isotropic around the primary source. The difference in each of these scenarios is how the primary continuum is produced and then absorbed. If the absorbing material is in fact surrounding the AGN then it stands to reason that the absorbing material is what is driving the long term variability in Mrk 1239. This is the case regardless of which model (ionised partial covering or blurred reflection) is implied as the additional component to fit the continuum above 3 keV. ==

## 2.6 Conclusion

In this work, multi-epoch X-ray spectra spanning 18 years of the NLS1 galaxy Mrk 1239 are presented. This study combines data from *XMM-Newton* and *Suzaku* with a simultaneous *NuS-TAR* and *Swift* observation to study the spectrum and variability of this source. A comparison

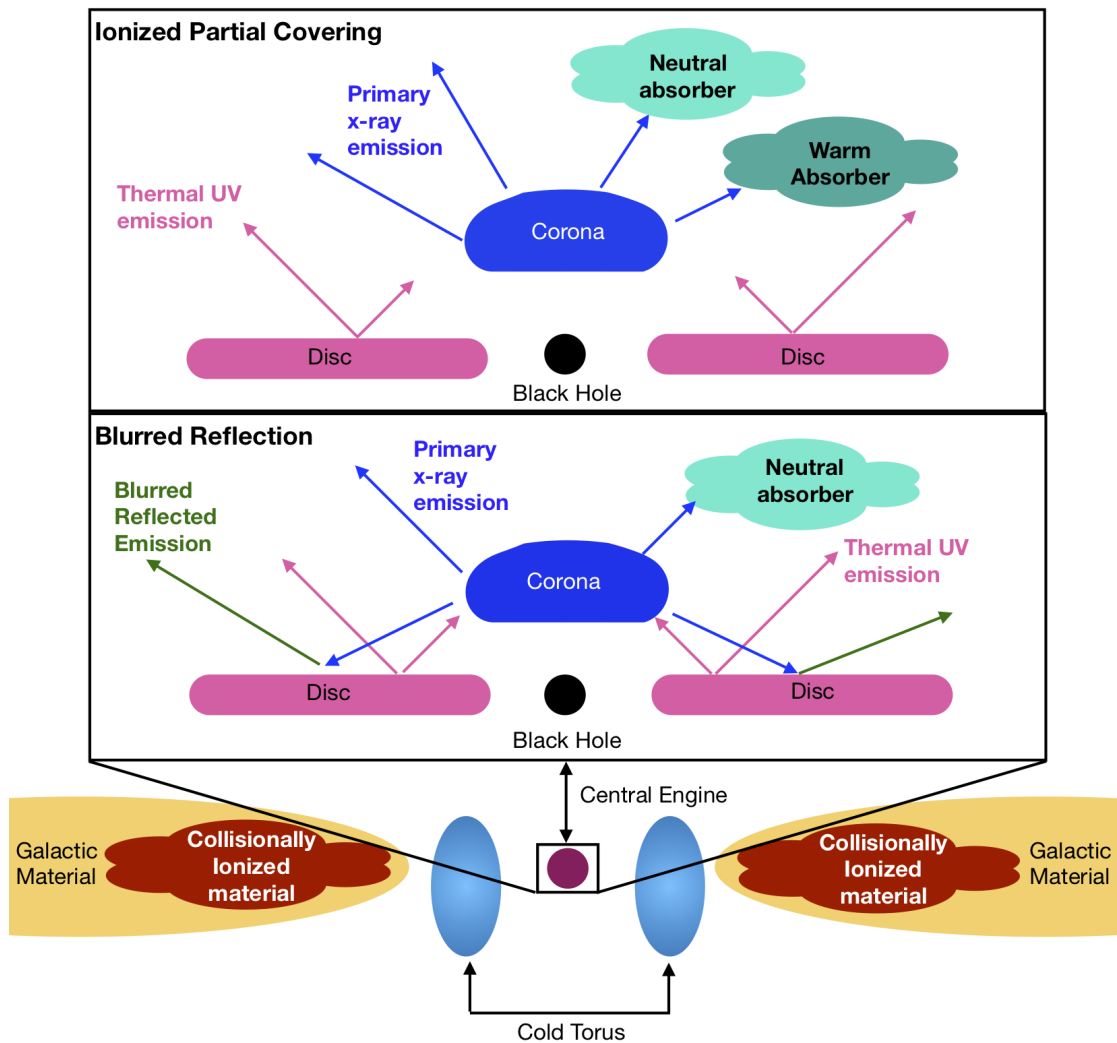


Figure 2.6: A graphic interpretation of our proposed models. The top box shows the AGN in the ionized partial covering scenario. The bottom box show the AGN in the blurred reflection scenario. In both the ionized partial covering and blurred reflection scenarios, the absorption of the primary continuum is inside the torus.

of the unfolded spectra reveals that the spectra are very similar at all epochs below 3 keV, while the *NuSTAR* and *Swift* data are brighter by a factor of 2 – 3 at higher energies. The light curves also reveal no short term variability below 3 keV, while modest variability at higher energies is seen.

Motivated by this, and by signatures of star formation in the infrared spectra presented in previous works, we successfully model the soft spectrum with emission from a hot plasma. When

the absorption component is removed, the starburst component accounts for  $\sim 1 - 10$  per cent of the total emission, which is sensible for a type-1 AGN. Both a blurred reflection and ionised partial covering model are employed to explain the remainder of the emission. Both models have several key components in common; a power law component with a slope of  $\sim 2.3 - 2.4$ , a neutral absorber with a covering fraction near  $\sim 1$ , and contributions from a distant reflector (e.g. the torus). There are some apparent inconsistencies which may be difficult to explain in the blurred reflection model, including a high iron abundance, and a low emissivity index despite having a reflection dominated spectrum. By contrast, the two-component absorption model may agree with the two polarisation regions found in the optical emission.

Deep observations with calorimeter-type resolution (e.g. Takahashi et al. 2016) such as *XRISM* (Tashiro et al. 2018) may help to reveal any emission line features present in the low energy spectrum from the starburst and distant reflection components. They may also reveal absorption features present at high energies, helping to confirm the high level of absorption required to fit the observed curvature. Additionally, future observations with *XMM-Newton* may help to confirm the minimal level of low energy variability and support a starburst emission component to explain the soft emission from this unique source.

## **Chapter 3**

# **Multi-Epoch, Broadband Analysis of WKK 4438: Origins of the Broad Iron Line and Hard Excess**

### **3.1 Introduction**

The primary source of X-rays in NLS1 is typically the (optically thin) corona, which produces X-rays via inverse Compton scattering of UV seed photons produced by the accretion disc. The properties of the primary X-ray emission are determined by the optical depth and temperature of the corona (see Section 1.2.1 and references therein). Other features often found in the spectra of NLS1s are the soft excess (of unknown origin); narrow and broad Fe  $K\alpha$  emission lines believed to originate from neutral and ionised iron found in the torus and disc, respectively; and the Compton hump produced by Compton scattering of photons emitted by the corona off of optically thick material. The Compton hump is seen in the hard X-ray spectra, peaking between 20 – 30 keV.

Blurred reflection (Ross & Fabian 2005) is a widely used explanation for the spectra of

NLS1s, it can account for many of the features seen in the X-ray spectra (e.g. broad iron line, Compton hump, soft excess). It can naturally explain the observed correlation between the hard and soft excess seen in NLS1s (Waddell & Gallo 2020) as both features are originating from the same process.

Other scenarios may be responsible for the features described above, including soft Comptonization (Done et al. 2012) where a second cooler corona is responsible for the soft excess; or partial covering where absorbing clouds are responsible for creating the complex spectra seen (e.g. Tanaka et al. 2004). A more detailed investigation of partial covering can be found in Chapter 2.

An alternate explanation of the excess emission above 10 keV could be synchrotron self-Comptonization (SSC) emission, originating from a jet component (Ghisellini & Maraschi 1989). SSC emission has been used to explain excess emission in other objects such as quasars (e.g. 3C 273 Madsen et al. 2015); blazars (e.g. Mrk 421, Tramacere et al. 2009); and RL-NLS1s (e.g. PKS 2004-447, Gallo et al. 2006). A challenge with SSC emission is distinguishing it from the traditional source of the hard excess, the Compton hump. High energy spectral data is needed to attempt to confirm the presence of SSC emission.

WKK 4438 (IGR J14552-5133) is a  $\gamma$ -ray emitting NLS1, located at a redshift of  $z = 0.016$  (Masetti et al. 2006), and viewed through a Galactic column density of  $4.34 \times 10^{21}$  atoms  $\text{cm}^{-2}$  (Willingale et al. 2013). The the  $\text{H}\beta$  line has a width of  $\text{FWHM} = 1700 \text{ km s}^{-1}$  and the mass of the SMBH is  $2 \times 10^6 M_{\odot}$  (Malizia et al. 2008). WKK 4438 is part of the *BAT* 105 month survey (Oh et al. 2018), and it has been detected with the  $\gamma$ -ray telescope, *INTEGRAL* (Landi et al. 2007). The  $\gamma$ -ray emission, thus suggests the presence of jet activity, but there are no radio observations to confirm the existence of a jet in WKK 4438. The presence of a jet would place WKK 4438 in the minority of NLS1s, as it is not a common feature in the population.

Jiang et al. (2018) presented evidence of a ultra-fast outflow (UFO) in the *Suzaku* 2012

and *NuSTAR* 2013 spectra of WKK 4438. A second absorption feature was found at 4.6 keV and interpreted as absorption due to Ar XVIII originating from the same UFO. Both absorption lines attributed to the UFO were seen in the spectra of the *Suzaku* 2012 and *NuSTAR* 2013 observations, which is important in determining the confidence of the interpretation.

This work presents the spectral and timing analysis of all available X-ray data from *Suzaku*, *NuSTAR* and *Swift*, spanning 6 years between 2012 and 2018, and comparing with the hard X-ray/ $\gamma$ -ray spectra from *Suzaku-PIN* and *Swift-BAT* detectors. This work will focus on modelling the broadband X-ray spectrum, which has never been done. In Section 3.2, the observations and data reduction techniques are summarised. We can use this to study the nature of the soft excess and see if there is evidence for a jet in the X-rays. A timing analysis will be done in Section 3.3, examining the variability of the source across both long (years) and short (hours) timescales. In Section 3.4 we will employ two separate interpretations of the spectral data developed using the *NuSTAR* 2018 observations, to analyze the broadband, multi-epoch spectra. A discussion of the results is given in Section 3.5 where we attempt to find a self-consistent description that fits the spectral data and the timing data. Conclusions about the physical interpretation of WKK 4438 are drawn in Section 3.6, and future work is summarised.

## 3.2 Data Reduction

WKK 4438 has been observed once by *Suzaku* (Mitsuda et al. 2007) in 2012 and twice by *NuSTAR* (Harrison et al. 2013) in 2013 and 2018. It has been consistently monitored by *Swift* (Burrows et al. 2004) and is part of the *Swift-BAT*-105 month survey (Oh et al. 2018). Observations of WKK 4438 are summarised in Table 3.1, with the instrument name, exposure time, and energy range. The *Swift-BAT* and *Suzaku-PIN* observations were not used for spectral fitting as the data were of lower quality (*Suzaku-PIN*) or were averaged over many observations (*Swift-BAT*).

(1)	(2)	(3)	(4)	(5)	(6)
Observatory	Observation ID	Name	Date	Exposure [s]	Energy Range [keV]
<i>Suzaku</i> XIS 0+3	706011010	S2012	2012-01-22	70321	0.7-1.5, 2.5-10
<i>Suzaku</i> PIN		PIN	2012-01-22	57470	15-30
<i>NuSTAR</i> (FPMA/B)	60061259002	N2013	2013-09-19	21943	3-30
<i>Swift</i> XRT	00080140001	Sw2013	2013-09-20	7077	0.5-4
<i>NuSTAR</i> (FPMA/B)	60401022002	N2018	2018-09-21	100942	3-50
<i>Swift</i> XRT	00088730001	Sw2018	2018-09-22	2053	0.5-4
<i>Swift</i> - BAT	-	BAT	-	-	15-150

Table 3.1: Observation log for WKK 4438. The observations and instruments used for analysis are listed in column (1). The observation ID and labels used in this work are given in columns (2) and (3), respectively. The start date of each observation is given in column (4) with the format [YYYY-MM-DD]. The duration of each observation, is given in column (5). The energy each observation were fit over is given in column (6). For the *NuSTAR* and *Swift* observations to reduce confusion we will only refer to the data by observatory name and year observed. Unless otherwise specified the data from FPMA and FPMB will be summed.

Instead the highest energy spectra are used to compare high energy spectral changes and model predictions.

### 3.2.1 *NuSTAR* and *Swift*

The *NuSTAR* observations had a duration of 22 ks and 101 ks for the 2013 and 2018 observations, respectively. Each was accompanied by a snap shot observation with *Swift*. For the *NuSTAR* 2018 and 2013 observations, the spectra were extracted using circular regions of 75'' radius and the background from a region of 110'' radius on the same chip. The data were processed using CALDB index version 20170817 and 20150316 for the 2018 and 2013 observations, respectively. The simultaneous *Swift* XRT data were built by *Swift*-XRT data products generator (Evans et al. 2009)<sup>1</sup>. All the spectra were optimally binned using FTGROUPPHA (Kaastra & Bleeker 2016). The *Swift*-BAT 105 month spectrum was obtained from the survey catalogue<sup>2</sup>, no additional

<sup>1</sup>[https://www.swift.ac.uk/user\\_objects/](https://www.swift.ac.uk/user_objects/)

<sup>2</sup><https://swift.gsfc.nasa.gov/results/bs105mon/>

binning was applied. The *BAT* data were collected from late 2004 until mid 2013 (Oh et al. 2018).

### 3.2.2 *Suzaku*

The *Suzaku* spectra were extracted from the XIS0 and XIS3 front illuminated (FI) detectors from a 240'' source region, and a 180'' background region. Response matrices were made using XISRMFGEN and XISSIMARFGEN. The spectra from the two detectors were merged to improve signal-to-noise, and only the merged FI spectrum is presented for the remainder of the analysis.

Data from the HXD-PIN detector were also retrieved using HXDPINXBPI, resulting in a 58 ks exposure. The background level is determined using both the non-X-ray background (NXB) and the cosmic X-ray background (CXB). Detections of 5% above background are considered significant (Fukazawa et al. 2009), for this work the *PIN* detection was 6.2%. A calibration factor of 1.18 was used between the XIS and PIN detectors (when applicable).

## 3.3 Characterizing the Variability

The variability analysis of WKK 4438 will be divided into two major time scales, rapid variability on time scales of hours (Section 3.3.1) and long term variability over years (Section 3.3.2). The rapid variability will be analysed using the light curves of the N2018 observation. The long term variability will examine spectral and flux changes in the object between different epochs.

### 3.3.1 Rapid Variability

We begin the analysis into the rapid variability of WKK 4438 with the most recent *NuSTAR* observation (N2018). The light curves were made with HEASOFT 6.26. For our analysis, the light curves for the two detectors, FPMA and FPMB, were summed using LCURVE. The light curves were also binned in LCURVE using four separate time bins: 500 s, 1000 s, 5780 s (or



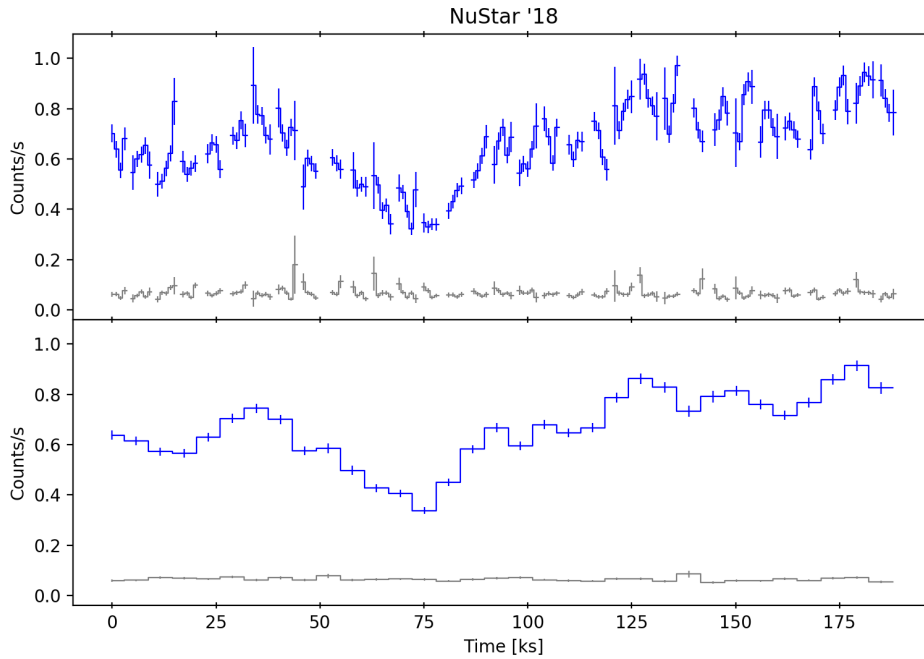


Figure 3.1: *Top panel:* Light curve (blue) of WKK 4438 with 1000 s time bins. The background is shown in gray to illustrate background levels. *Bottom panel:* Summed lightcurve (blue) of WKK 4438 with 5780 s time bins. The summed background is shown in gray to illustrate background levels.

orbital bins), and 10 ks. Temporal regions that are background dominated were removed. The broadband lightcurve (3-50 keV) of the N2018 data is presented in Figure 3.1, with 1000 s and 5780 s time bins. The light curves vary in brightness throughout the observation, with a dip in the lightcurve centred at 75 ks. To further examine the rapid variability, energy resolved light curves were produced with energy bins of 3-5 keV, 5-8 keV, 8-10 keV, 10-20 keV, and 20-40 keV. Above 40 keV the data become background dominated. The normalized hardness ratio given by  $HR = (H - S)/(H + S)$  where  $H$  and  $S$  are the hard and soft bands, respectively, were calculated to search for spectral variability. In this analysis the soft band is always 3-5 keV. Figure 3.2 shows the 5-8 keV, 8-10 keV, 10-20 keV, and 20-40 keV bands compared to the soft band of 3-5 keV.

Each hardness ratio is compared to a constant with a  $\chi^2$  test to determine the level of vari-

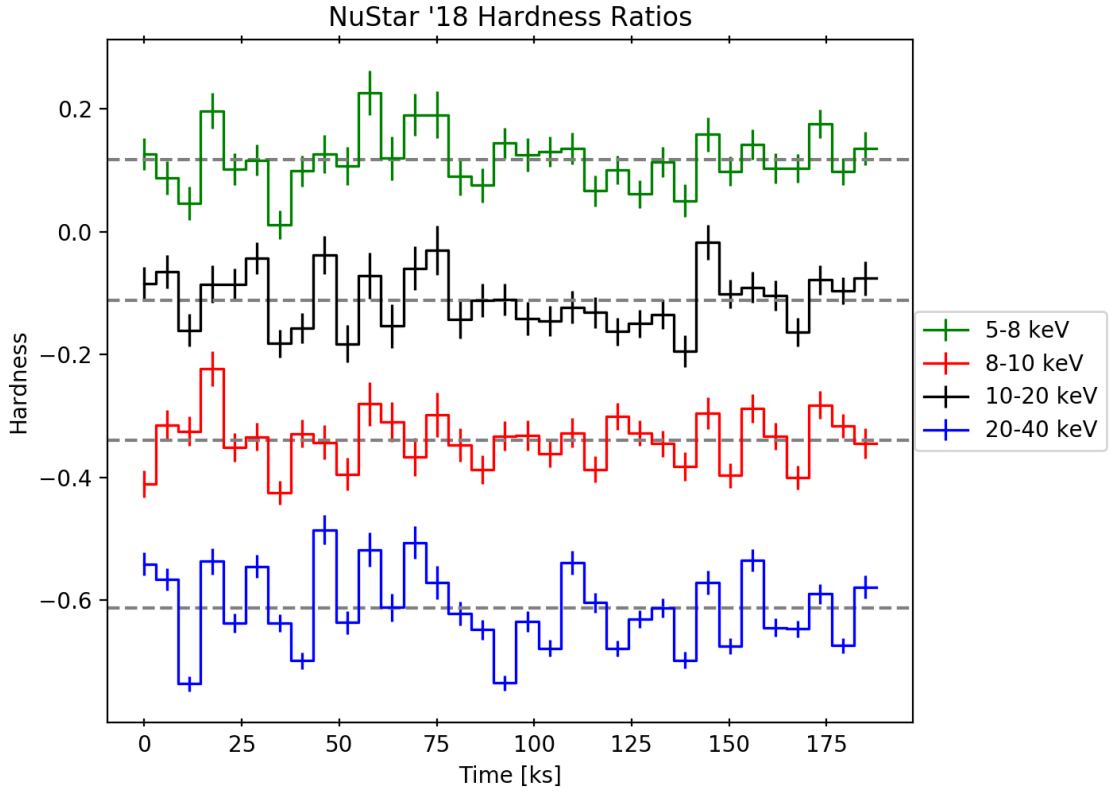


Figure 3.2: Hardness ratios for orbital binned light curves (N2018) of WKK 4438. All energy bands are compared to the 3-5 keV soft band, and the legend identifies the hard band. The gray lines shows the mean hardness ratio for each band.

ability in each band. These fit values are presented in Table 3.2. There was insufficient data quality for the hardness ratio to be consistently calculated for the 500 s time bins. There is a significant departure in the reduced  $\chi^2$  values calculated between the softer bands (5-8, 8-10, and 10-20 keV) and that calculated for the hardest band (20-40 keV). This departure can be seen

(1)	(2)	(3)	(4)
Energy band	1000 s	5780 s	10 ks
5-8 keV	275/142	88/32	35/18
8-10 keV	537/142	110/32	30/18
10-20 keV	460/142	94/32	30/18
20-40 keV	1654/134	551/32	215/18

Table 3.2: The fit statistic for each HR compared to a constant fit. Column (1) The energy band used as the hard band. Column (2)-(4) states the  $\chi^2_{\nu}/\text{dof}$  for each time bin a hardness ratio was calculated for. The soft band is always 3-5 keV.

most clearly in the fit statistics of the 10 ks time bins, where the reduced  $\chi^2$  values is  $\sim 30/18$  for the soft bands and 215/18 for the hardest band. However the hardness ratio variations do not show any correlation with brightness as might be expected. This suggests that the hardness ratio changes we see here may simply be due to stochastic processes in the light curves rather than any physical reason.

Next the fractional variability was calculated according to the methods outlined in Edelson et al. (2002). The five energy bins described above were used, with a slight modification that the 8-10 keV was increased to 8-12 keV to improve data quality. The fractional variability was calculated for the four time binned light curves. For the 500 s and 1000 s time bins, we cannot calculate the fractional variability in the 20-40 keV band due to data quality. Examining Figure 3.3 we can see that the fractional variability for this observation is flat. A  $\chi^2$  test was used to compare the data to a constant fit. For all time bins  $\chi^2_{\nu}/\text{dof} < 1$  indicated a constant could describe the fractional variability well. There is no difference between the fractional variability above and below 20 keV, that we saw in the hardness ratios, further indicated that the difference

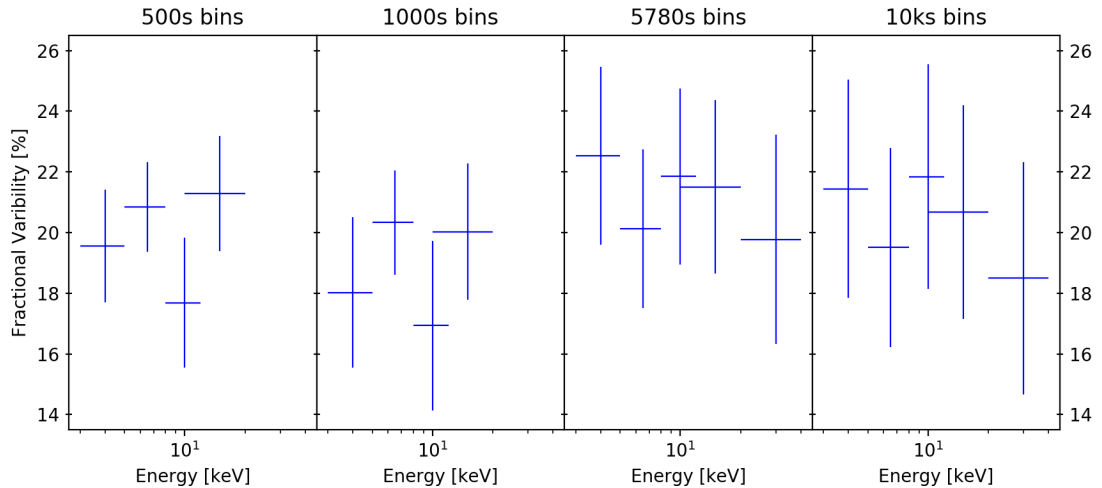


Figure 3.3: *Left panel:* The fractional variability for the N2018 spectra with 500 s time bins. *Middle left panel:* The fractional variability for the N2018 spectra with 1000 s time bins. *Middle right panel:* The fractional variability for the N2018 spectra with 5780 s time bins. *Right panel:* The fractional variability for the N2018 spectra with 10 ks time bins. The energy bins used for all panels are 3-5 keV 5-8 keV 8-12 keV 10-20 keV and 20-40 keV. The fractional variability is constant across all energy bands.

seen in the hardness ratios was due to stochastic processes.

### 3.3.2 Long Term Variability

The unfolded spectra of WKK 4438 are presented in Figure 3.4. The data from the two *NuSTAR* detectors have been summed for each of their respective years for visual clarity and data quality, and the high energy *Swift-BAT* and *PIN* spectra have been included in this figure. The earliest

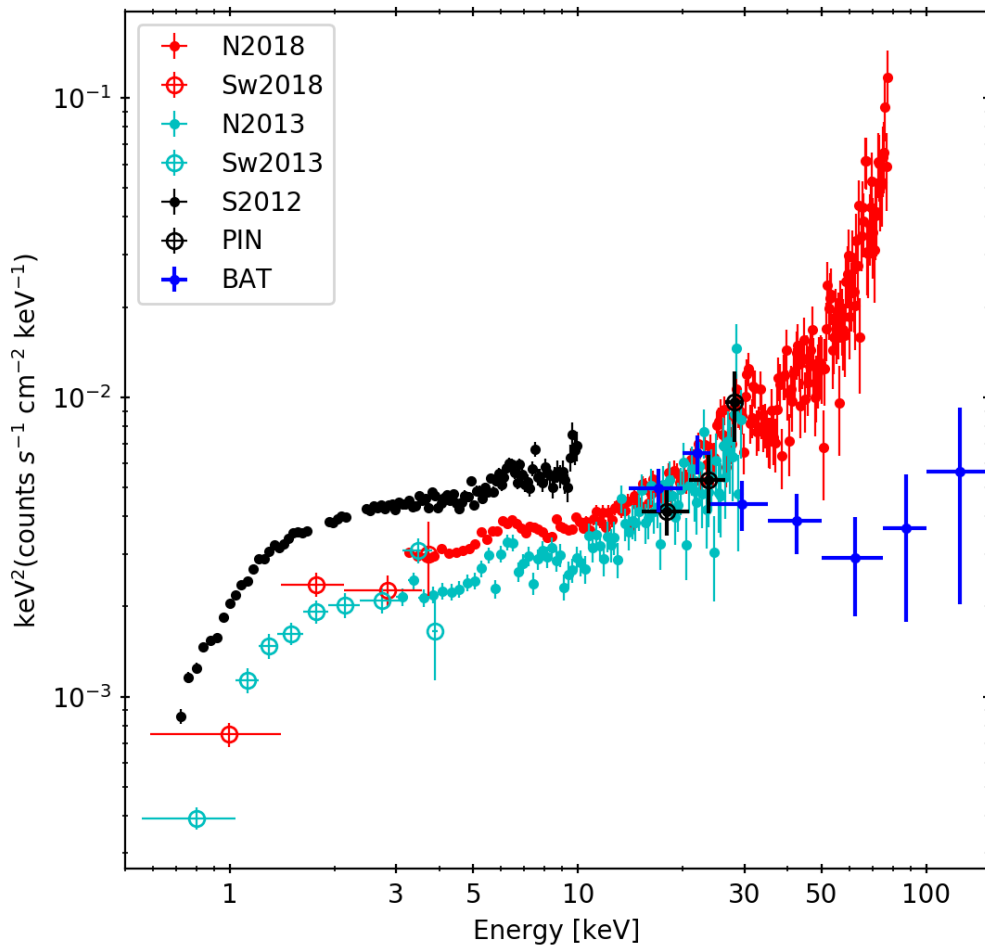


Figure 3.4: The unfolded spectra of WKK 4438, with pointed observations spanning 6 years, and the *BAT* 105 month spectra.

pointed observation is the S2012 XIS spectra and it sports the highest flux level in the soft band.

Compared to the *Swift*-XRT observations (snapshots taken contemporaneous to *NuSTAR*), S2012 maintains its higher flux level. In the hard X-ray band, the 2012 PIN data are more consistent with the *NuSTAR* observations. The flux of the N2018 data is situated between the S2012 and N2013 data. This suggests a high level of variability on long time scales in the soft X-ray band.

When comparing the pointed observations to the long-term monitoring data with *Swift*-BAT over 105 months, we note some interesting behaviour. The long term average spectra seem to be consistent with the pointed observations below 30 keV. However between 30-70 keV the N2018 data exhibits a much brighter and harder spectra than the long term mean spectrum. This difference could be indicative of a flaring event during the N2018 observation, or long term spectral change in the hard X-rays.

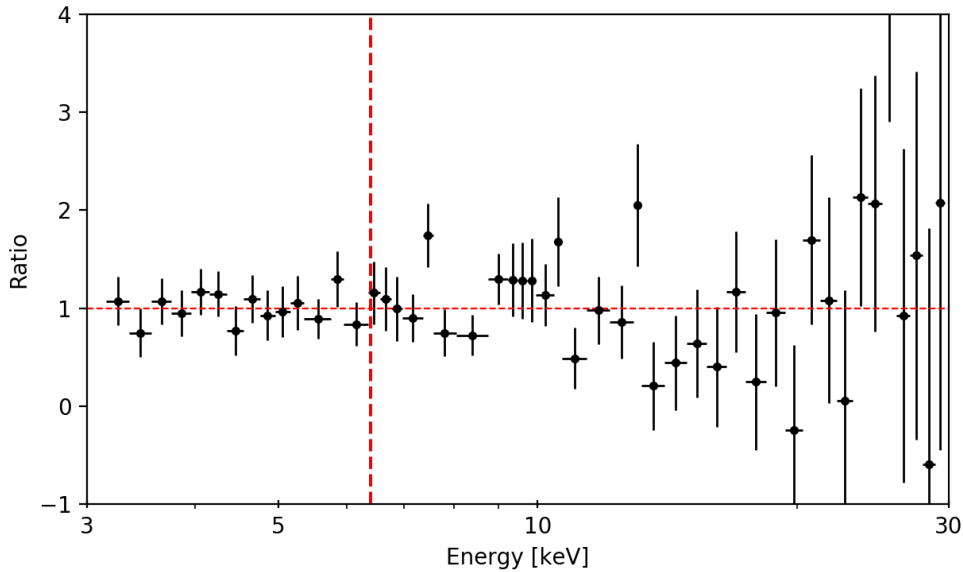


Figure 3.5: Ratio from fitting the difference spectra (N2018-N2013) with a power law. The vertical line is at 6.4 keV where we see Fe  $K\alpha$  emission. Deviations from a powerlaw fit indicate where there is spectral change between epochs. For WKK 4438 there is limited deviation in the ratio indicating that a powerlaw change is driving the long term variability.

The difference spectra can give us insights into the nature of the variability. The difference spectra was produced using the summed *NuSTAR* spectra. In this case we subtracted the N2013 spectra from the brighter N2018 spectra and fit with a Galactic absorbed power law ( $N_H =$

$0.434 \times 10^{22}$  atoms  $\text{cm}^{-2}$  Willingale et al. 2013). The ratio of this can be seen in Figure 3.5. The difference spectrum is well fit with a power law. This indicates that the primary difference between the N2018 and N2013 is a change in brightness and not in the shape of the continuum.

### 3.4 Spectral Modelling

All spectra used for modelling were optimally binned using FTGROUPPHA and C-statistics (Cash 1979) were applied to evaluate the fit quality. The modelling was carried out using XSPEC version 12.11.1c (Arnaud 1996). All spectra were background modelled except for the *PIN* and *BAT* spectra which were background subtracted. Cross-calibration constants were applied between the *NuSTAR* FPMA, FPMB and *Swift*-XRT spectra. They were free to vary and were monitored to ensure they fell within the acceptable range given by *NuSTAR* FAQ<sup>3</sup>. The *PIN* and *BAT* spectra were not used in spectral modelling, but were only utilized to compare the high energy predictions of our two competing models discussed below. The *PIN* spectra were linked to the S2012 data by a cross-correlation constant frozen at 1.18<sup>4</sup>. The *BAT* spectra were linked to the N2018 data.

The parameter errors were calculated using a Markov chain Monte Carlo (MCMC) method. This method randomly samples the probability distribution function proposed by the model tested, accepting or rejecting parameter values based on the probability that the observed data producing that value. The burn-in phase is used to ensure that the method is not biased by the initial parameters, and has reached a stationary distribution. Chains found during the burn-in phase are discarded and only chains after this are recorded. These accepted values form the chains of parameters used to estimate errors (Ivezić et al. 2019). We utilized the Goodman-Weare algorithm (Goodman & Weare 2010), with 70 walkers<sup>5</sup>, a burn-in length of 19950 and

<sup>3</sup>[https://heasarc.gsfc.nasa.gov/docs/nustar/nustar\\_faq.html](https://heasarc.gsfc.nasa.gov/docs/nustar/nustar_faq.html)

<sup>4</sup><https://heasarc.gsfc.nasa.gov/docs/suzaku/analysis/abc/node8.html>

<sup>5</sup>independent chains that move through parameter space

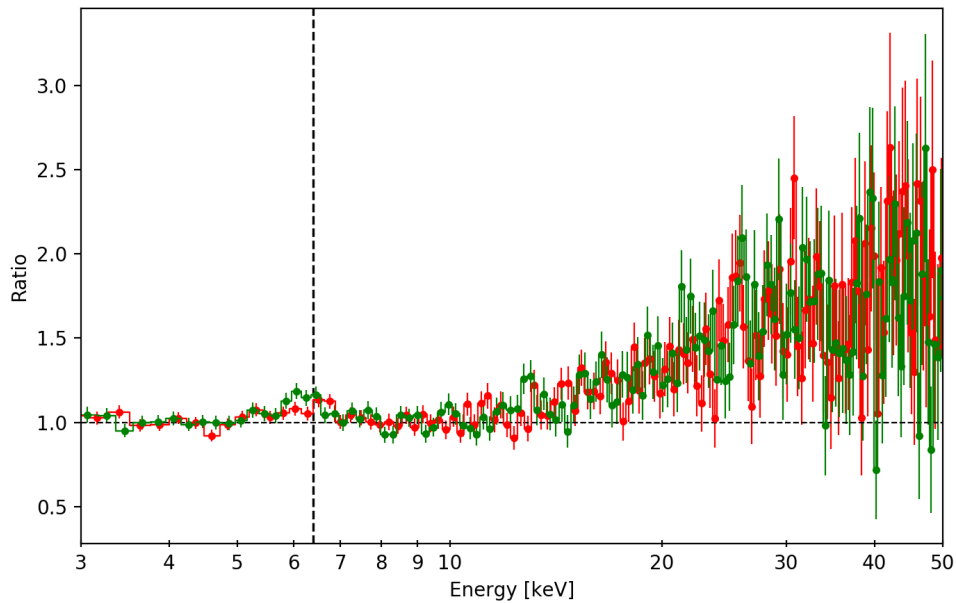


Figure 3.6: The residuals of a Galactic absorbed power law fit to N2018 data over 3-5 and 8-10 keV, then extrapolated over 3-50 keV to illustrate the departure from a power law in the spectra.

a chain length of 99960. After the MCMC algorithm was completed the errors were calculated using the native MCMC error command in XSPEC. The values quoted in this work are at the 90% confidence level.

The spectral modelling began by analysing the N2018 data. A toy model of a Galactic absorbed power law was applied to the data and fit over 3-5 keV and 8-10 keV, a region we expect to be power law dominated. The residuals of this fit can be seen in Figure 3.6, and show significant deviation from a power law in the Fe  $K\alpha$  band and above 10 keV. WKK 4438 shows evidence of a significant hard excess.

To investigate the origin of the broad excess in the Fe  $K\alpha$  band, the N2018 spectra were fit over 3-10 keV with a variety of different line profiles to describe the broad iron line. Figure 3.7 shows the residuals of these fits.

The emission line profiles tested include a broad Gaussian (e.g. ZGAUSS); disc emission line (e.g. DISKLINE; see Fabian et al. 1989) and a Laor line for gravitationally broadened Fe  $K\alpha$

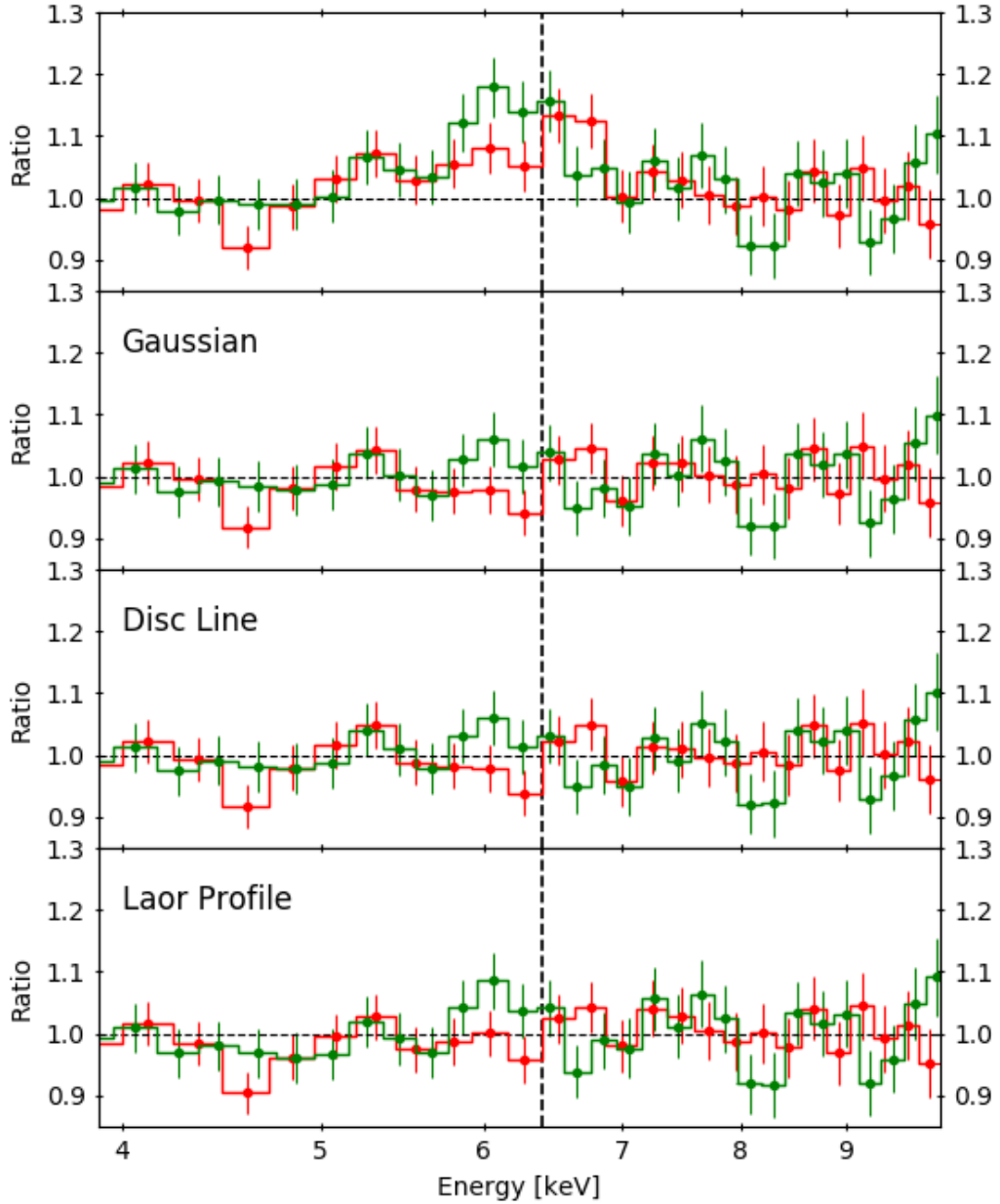


Figure 3.7: The residuals of the N2018 spectra fit with a variety of line profiles for the Fe  $K\alpha$  emission line. *Top panel:* Spectra fit a power law over 3-5 and 8-10 keV to demonstrate the intrinsic shape of the emission line ( $C/\text{dof} = 161/115$ ). *Second panel:* Power law plus Gaussian ( $C/\text{dof} = 96/112$ ). *Third panel:* Power law with disc line ( $C/\text{dof} = 95/112$ ). *Bottom panel:* Power law with Laor line profile ( $C/\text{dof} = 103/112$ ).

emission (e.g. LAOR; see Laor 1991). The power law continuum fit to the N2018 data has a fit quality of  $C/\text{dof} = 161/115$ . The addition of a Gaussian profile resulted in a  $\Delta C = 65$ , while a disc line had  $\Delta C = 66$ , both for three additional free parameters. The Laor line produced a fit with  $\Delta C = 58$ , again for three additional free parameters. For the disc line a high inclination



was required to obtain the fit quality. If the inclination was frozen at  $30^\circ$ , a more fiducial value for a NLS1 and in line with what has been previously reported for WKK 4438 (Jiang et al. 2018), the fit quality reduces to  $C/\text{dof} = 101/113$ , but still an acceptable fit. As well, there are slightly more pronounced residuals in the Fe  $K\alpha$  band with the inclination fixed. For now, the broad iron line will be measured using a Gaussian, as it has an equivalent fit to the disc line, and does not have any ambiguity with the disc inclination.

Two competing models were developed based on the N2018 spectra: The first was a double power law with a broad iron line modelled using a Gaussian; the second was a blurred reflection model using lamp post geometry, consistent with the models used in Jiang et al. (2018).

The double power law model is motivated by possible jet emission. In this scenario a soft component is responsible for the AGN emission (i.e. Comptonization in a traditional optically-thin corona) and the hard component is responsible for the SSC emission (e.g. Gallo et al. 2006; Grupe et al. 2008; Gonzalez et al. 2020). A cut-off power law is used to model both components due to its simplicity. More complex and physical models for Comptonization (Titarchuk (1994)) and SSC emission are available (Kataoka et al. 1999).

Blurred reflection (Ross & Fabian 2005) is a popular choice for spectral modelling in NLS1s, especially those with broad iron lines (e.g. Fabian et al. 2004; Risaliti et al. 2013; Marinucci et al. 2014). In a blurred reflection scenario, photons from the corona are reflected off the inner regions of the accretion disc. The extreme general relativistic effects that are present near the SMBH blur the reflected emission, producing broadened emission lines. Other characteristics of a reflection spectra are the soft excess (discussed in Chapter 2) and the Compton hump. The Compton hump results in an excess emission above 10 keV typically peaking at  $\sim 20 - 30$  keV. It arises from Compton scattering of high energy photons off of material surround the SMBH.

Both models had mechanisms to describe the two major components seen in the N2018 spectra (e.g. broad iron line and hard excess). The double power law utilizes a Gaussian for

the iron line and a second hard power law to capture the hard excess. The blurred reflection scenario utilizes a gravitationally broadened iron line and a Compton hump for the hard excess. We attempt to model the multi-epoch data using both models in a self-consistent manor.

### 3.4.1 Double Powerlaw

To examine a jet origin for the X-ray emission in WKK 4438 we begin by fitting a double power law. The XSPEC model reads as:  $\text{TBABS} \times \text{ZTBABS}(\text{ZGAUSS} + \text{CUTOFFPL} + \text{CONSTANT} \times \text{CUTOFFPL})$ . In this model, TBABS is the Galactic column density, and ZTBABS accounts for column density in the host galaxy of WKK 4438. We model the broad Fe  $K\alpha$  line using ZGAUSS and allowing the rest frame line energy and line width free to vary. The soft and hard power laws are modelled using a cut-off power law with the cut-off energy fixed to 300 keV. The hard power law in the S2012 spectrum is linked by a constant factor to the N2018 data since S2012 data do not extend past 10 keV. By linking the hard power law between N2018 and S2012 epochs with a constant value we can ensure that the S2012 fit will account for both power laws even if the S2012 data are dominated by the softer one. Figure 3.8 show the double power law model, along with the data folded over the detector responses and the residuals resulting from the best fit model. The best fit parameters can be found in Table 3.3, and the errors for these parameters were found using MCMC chain produced by XSPEC. The double power law model had a best fit of  $C/\text{dof} = 864/1080$ . In all three epochs, the line energy found for the Gaussian is consistent with Fe  $K\alpha$  at 6.4 keV. The soft power law have a  $\Gamma \approx 2$ , and the hard power law have  $\Gamma \approx 1$ .

The variability was tested between epochs to determine its spectral origin. Different iron line and continuum parameters were linked to test different scenarios. The continuum parameters were the hard and soft  $\Gamma$  values and both power law normalizations. The broad iron line parameters were the line centre ( $L_E$ ), line width ( $\sigma$ ) and iron line normalization. The cut-off

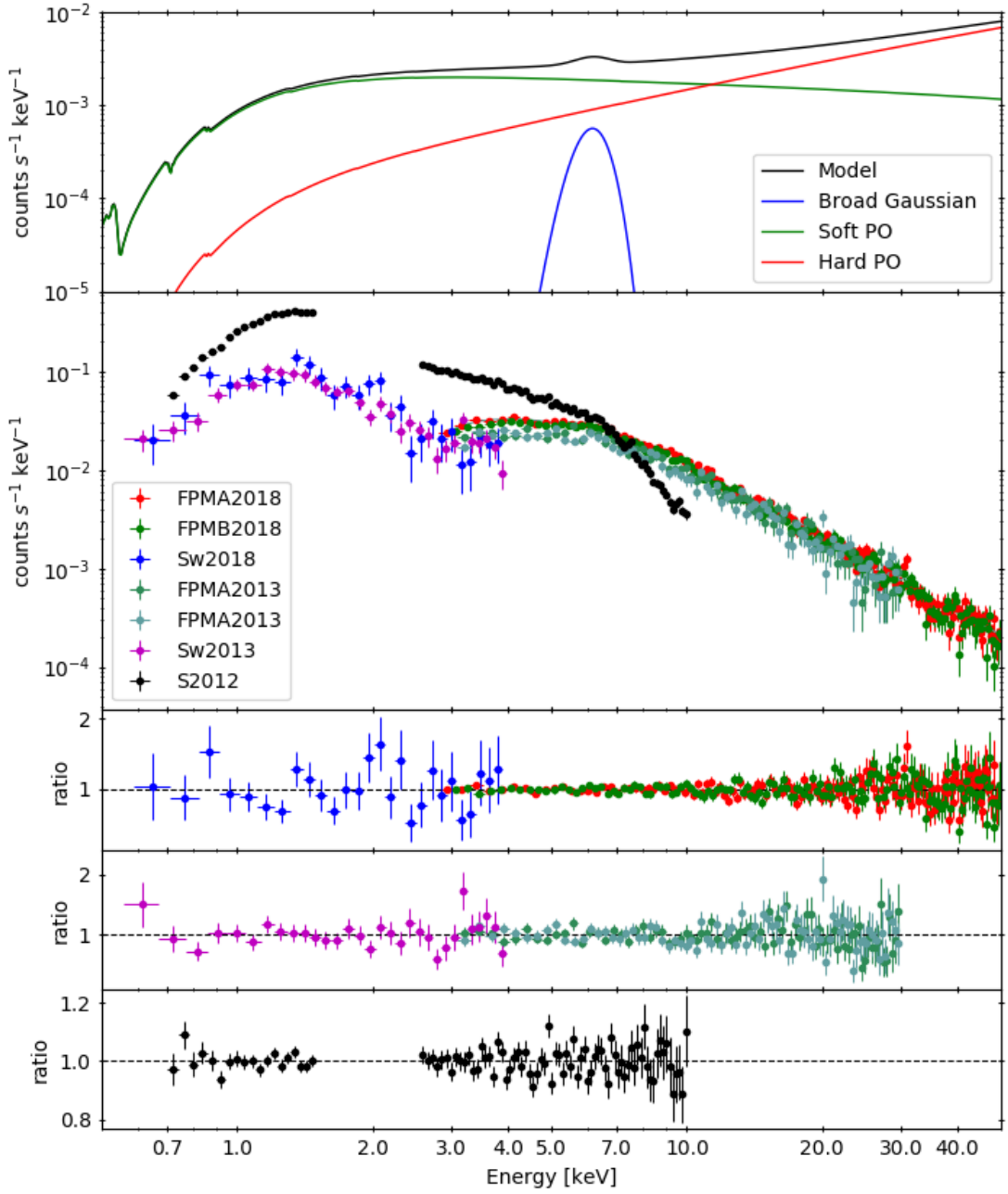


Figure 3.8: *Top Panel:* Model showing the three primary components of the best fit. *Second Panel:* Data folded over the detector response for each spectra fit. *Middle Panel:* Ratio for the N2018 observation, with the Sw2018 snapshot. *Forth Panel:* Ratio for the N2013 observation, with the Sw2013 snapshot. *Bottom Panel:* Ratio for the S2012 data.

energies for both the hard and soft power law components were not constrained, instead they were each frozen to 300 keV.

With all parameters linked between epochs, the fit quality is quite poor, with  $C/\text{dof} =$

2356/1093. Releasing the hard power law normalization improves the fit by  $\Delta C = 1285$  for two free parameters. If instead we release the soft power law normalization (keeping the hard normalization linked), there is a further fit improvement  $\Delta C = 187$ , suggesting that either can account for a significant amount of the spectral variability, but the soft power law normalization can account for more.

Turning towards the photon indices, freeing the hard  $\Gamma$  results in a  $\Delta C = 49$  for one additional free parameter as compared to only the hard power law normalization free between epochs. Whereas if the soft  $\Gamma$  is freed between epochs there is only a  $\Delta C = 2$  for two additional free parameters. This suggests that the hard power law component is changing flux and shape while the soft power law component only changes flux between epochs.

With both soft and hard power law components free between epochs the fit improves to  $C/\text{dof} = 871/1086$ , a  $\Delta C = 16$  for three additional free parameters over the previous best fit with only the soft power law free to vary between epochs. Note here that the hard power law has only three parameters, the N2013  $\Gamma$  and normalization, and the S2012 hard power law contribution factor. Releasing the line energy for the broad iron line gives an insignificant fit improvement of  $\Delta C = 2$  for two additional free parameters. Releasing the line width and normalization of the iron line in addition leads to a fit improvement of  $\Delta C = 4$  for four additional free parameters. This indicates that in this model the broad iron line is remarkably consistent in all epochs, not changing shape or flux.

The results of the spectral fitting for the double power law model indicate that the variability can be accounted for with either normalization changes in the soft power law; changes in the flux and shape of the hard power law; or a combination of the two.

(1)	(2)	(3)	(4)	(5)	(6)
Model	Model Component	Model Parameter	N2018	N2013	S2012
Double Power Law	Neutral Absorber	$N_{\text{H}}$ [ $10^{20}$ ] atoms $\text{cm}^{-2}$	$4_{-2}^{+3}$	$4^l$	$4^l$
	ZTBABS				
	Broad Fe $K\alpha$ Line	Line energy [keV]	$6.2_{-0.3}^{+0.2}$	$6.2_{-1.1}^{+0.2}$	$6.4 \pm 0.2$
	ZGAUSS	Sigma [keV]	$0.7_{-0.2}^{+0.4}$	$0.4_{-0.3}^{+1.2}$	$0.5_{-0.1}^{+0.3}$
		Normalization [ $10^{-5}$ ]	$3 \pm 1$	$2_{-1}^{+3}$	$2 \pm 1$
	Soft Power Law	$\Gamma$	$2.18_{-0.05}^{+0.09}$	$1.82_{-0.08}^{+0.09}$	$2.08_{-0.05}^{+0.07}$
	CUTOFFPL	Cut off Energy [keV]	$300^f$	$300^f$	$300^f$
		Normalization [ $10^{-3}$ ]	$4.0_{-0.2}^{+0.4}$	$1.9 \pm 0.3$	$4.7 \pm 0.2$
	Hard Power Law	$\Gamma$	$0.73_{-0.07}^{+0.11}$	$0.1_{-0.3}^{+0.4}$	$0.73^l$
	CUTOFFPL	Cut off Energy [keV]	$300^f$	$300^f$	$300^f$
		Normalization [ $10^{-5}$ ]	$8_{-2}^{+4}$	$0.4_{-0.3}^{+0.8}$	$8^l$
	<i>Suzaku</i>	Constant	-	-	$0.9 \pm 0.4$
	FPMB Calibration	Constant	$1.00 \pm 0.02$	$1.01 \pm 0.04$	-
	<i>Swift</i> Calibration	Constant	$0.68_{-0.07}^{+0.08}$	$1.1 \pm 0.1$	-

(1)	(2)	(3)	(4)	(5)	(6)
Model	Model Component	Model Parameter	N2018	N2013	S2012
Blurred Reflection	Neutral Absorber	$N_{\text{H}}$ [ $10^{20}$ ] atoms $\text{cm}^{-2}$	$1.4^{+0.9}_{-0.7}$	$1.4^l$	$1.4^l$
	ZTBABS				
	Blurred Reflection	Coronal Height [ $\text{GM}/c^2$ ]	$< 3$	$< 3$	$43^{+20}_{-12}$
	RELXILLP	spin	$0.998^f$	$0.998^f$	$0.998^f$
		Inclination [ $^\circ$ ]	$30^f$	$30^f$	$30^f$
		Outer Radius [ $r_{\text{g}}$ ]	$400^f$	$400^f$	$400^f$
		redshift	$0.016^f$	$0.016^f$	$0.016^f$
		$\Gamma$	$1.0^r$	$1.7^r$	$1.90^r$
		$\log \xi$ [ $\text{ergs cm s}^{-1}$ ]	$3.81^{+0.24}_{-0.01}$	$3.3^{+0.4}_{-0.2}$	$3.4^{+0.2}_{-0.3}$
		$A_{\text{Fe}}$ [solar]	$8 \pm 1$	$8^l$	$8^l$
		$E_{\text{cut}}$ [keV]	$300^f$	$300^f$	$300^f$
		Normalization	$(1.5^{+0.5}_{-0.3}) \times 10^{-3}$	$(5^{+3}_{-2}) \times 10^{-4}$	$(1.5^{+0.5}_{-0.4}) \times 10^{-5}$
	Power Law	$\Gamma$	$1.0^{+0.1}_{-0.4}$	$1.6^{+0.7}_{-0.5}$	$1.90^{+0.05}_{-0.02}$
	CUTOFFPL	Cut off Energy [keV]	$300^f$	$300^f$	$300^f$
		Normalization	$(1.0^{+0.6}_{-0.7}) \times 10^{-21}$	$(1.0^{+0.3}_{-0.2}) \times 10^{-3}$	$(3.5 \pm 0.5) \times 10^{-3}$
	FPMB Calibration	Constant	$1.00^{+0.04}_{-0.02}$	$1.01 \pm 0.05$	-
	<i>Swift</i> Calibration	Constant	$0.9 \pm 0.1$	$1.1 \pm 0.1$	-

Table 3.3: Best-fit model parameters for WKK 4438. Column (1) indicates the tested model and column (2) indicates the model component. Column (3) indicates the model parameter and its units. Column (4) gives the value for each parameter for the N2018 epoch. Column (5) gives the value for each parameter for the N2013 epoch. Column (6) gives the value for each parameter for the S2012 epoch. All parameters with the superscript ‘ $f$ ’ are kept fixed at quoted values. The parameters with superscript ‘ $l$ ’ are linked between the 2018 and 2012 epochs.

### 3.4.2 Blurred reflection

For the blurred reflection scenario RELXILLP (García et al. 2014) was used for the reflection spectra. This is a different flavour of RELXILL than used in Chapter 2. It utilized a lamppost geometry for the corona, where the corona is located some height  $h$  above the accretion disc. This replaces the parameters specifying the emissivity profile in the standard flavour of RELXILL. The XSPEC model reads as:  $\text{TBABS} \times \text{ZTBABS}(\text{RELXILLP} + \text{CUTOFFPL})$ . Again, TBABS is the Galactic column density, and ZTBABS is included for the host galaxy column density. Figure 3.9 shows the best fit model for the blurred reflection scenario, the data folded over the detector response and the residuals for the best fit model at each epoch.

Similar to the double power law model, the cut-off energy is not constrained, and thus frozen at 300 keV for all epochs. The photon index in the reflection component is linked to the index of the primary power law component. The inner radius is fixed at the inner most stable orbit (ISCO) and the outer radius is fixed at  $400 r_g$ . The dimensionless spin parameter is defined as  $a = cJ/GM^2$ , where  $M$  is the black hole mass and  $J$  is the angular momentum. The parameter  $a$  can take on values of 0 (non spinning) to 0.998 (maximum spin). The spin is linked between epochs and frozen at 0.998. The inclination was not constrained and also linked between epochs and frozen at  $30^\circ$ . The disc ionization parameter ( $\log\xi$ ) and coronal height ( $h$ ) were free to vary between epochs, and the iron abundance ( $A_{\text{Fe}}$ ) was free to vary, but linked between epochs. The best fit parameters for the blurred reflection scenario are found in Table 3.3.

Initially, with all parameters linked between epochs the blurred reflection fit had a fit statistic of  $C/\text{dof} = 2689/1094$ . By freeing the blurred reflection component ( $h$ ,  $\log\xi$ , and normalization), the fit significantly improves with a  $\Delta C = 1128$  for 6 additional free parameters, for a fit statistic of  $C/\text{dof} = 1561/1088$ . Furthermore, releasing  $\Gamma$  or the power law normalization significantly improves the fit by  $\Delta C = 522$  or  $\Delta C = 557$ , respectively, for 2 additional additional

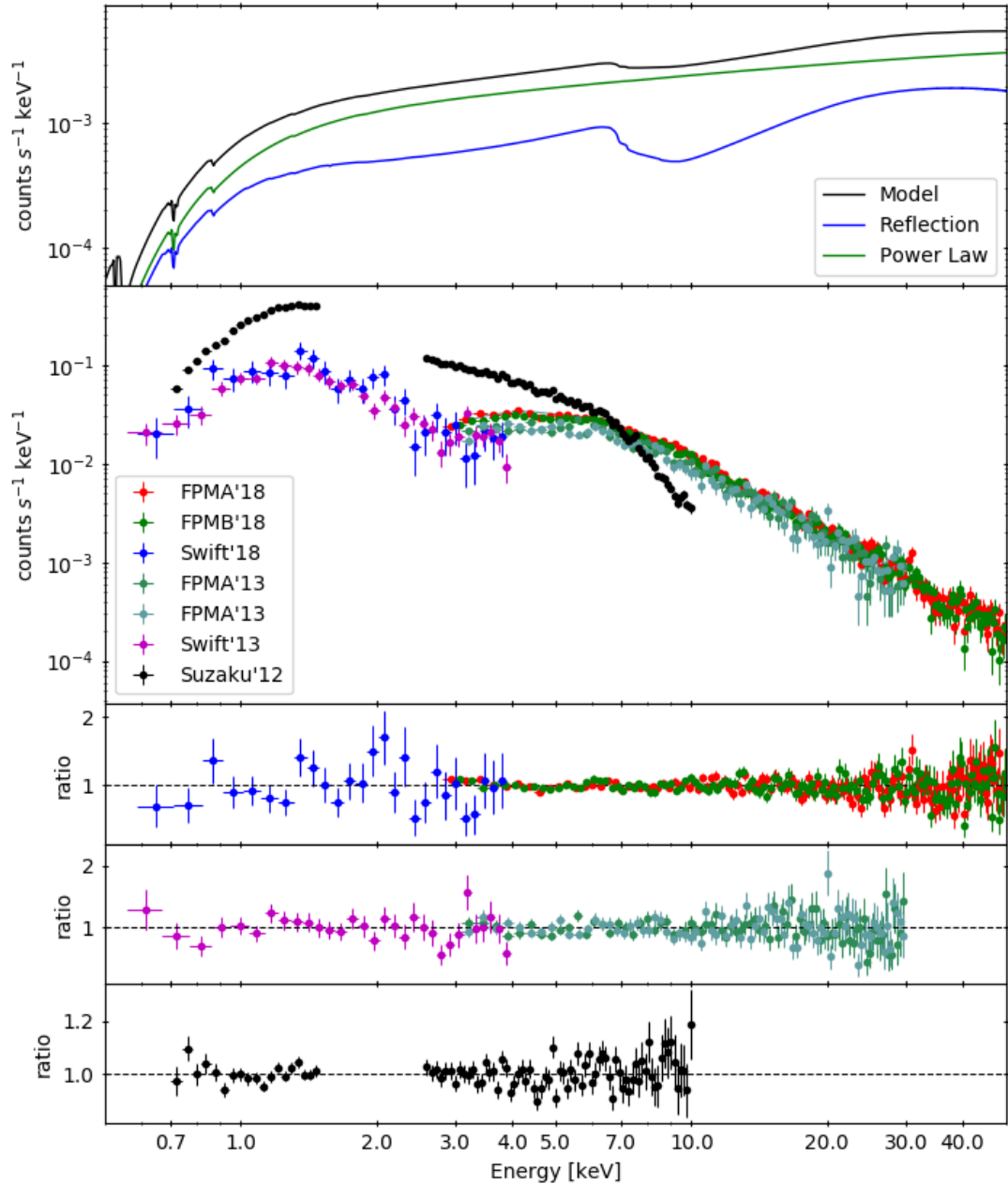


Figure 3.9: *Top Panel:* Model showing the three primary components of the best fit. *Second Panel:* Data folded over the detector response for each spectra fit. *Middle Panel:* Ratio for the N2018 observation, with the Sw2018 snapshot. *Forth Panel:* Ratio for the N2013 observation, with the Sw2013 snapshot. *Bottom Panel:* Ratio for the S2012 .

free parameters.

If we instead keep the reflection parameters linked, and release  $\Gamma$  between epochs the fit is  $C/\text{dof} = 1434/1092$ , an improvement of  $\Delta C = 1256$  for two additional free parameters. If the normalization is freed instead, there is a further fit improvement of  $\Delta C = 376$  ( $C/\text{dof} =$



1057/1092). Releasing  $\Gamma$  between epochs results in a  $C/\text{dof} = 1016/1090$ , an improvement of  $\Delta C = 41$  over just the normalization free (for two additional additional free parameters).

The best fit model for the blurred reflection scenario has the blurred reflection and power law components free between epochs, with a fit statistic of  $C/\text{dof} = 910/1084$ . From these fits we can conclude that a majority of the variability can be accounted for in much the same manor as the double power law scenario, with a changing in a power law normalization. However a significant amount of spectral change needs the reflection component and the spectral index to be free between epochs.

## 3.5 Discussion

### 3.5.1 Blurred Reflection

It was seen in Figure 3.5, that there was minimal spectral change between the N2013 and N2018 data below 30 keV. The result of fitting N2018 with the parameters obtained from N2013 simply scaled are shown in Figure 3.10. We can see a large departure between the the N2018 and N2013 model occurring above 30 keV, as well as a slight change in curvature between 10-20 keV. The best fit parameters for the blurred reflection models indicate a very flat  $\Gamma$  values for the N2018 data, which is at odds with the NLS1 classification, and other data presented (e.g. N2013, S2012). As well, the model requires  $A_{Fe} = 8 Z_{\odot}$ , this may indicate a high density disc model is needed (e.g. Jiang et al. 2018).

A more quantitative method of distinguishing between the epochs is the reflection fraction. The reflection fraction was calculated using a ratio of the 0.1-100 keV flux of the reflection component to the power law component. The normalization errors of each component were propagated through to find the errors of the reflection fraction. The three epochs had their reflection fractions calculated based on the FPMA18, FPMA13 and S2012 spectra, respectively.

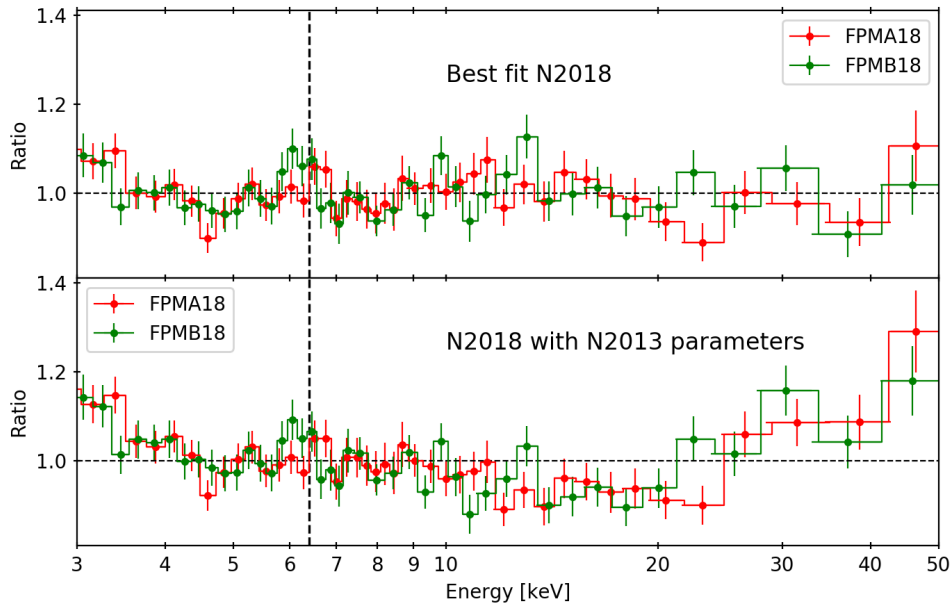


Figure 3.10: *Top panel:* Residuals for the best fit blurred reflection model on the N2018 data, binned for clarity. *Bottom panel:* The N2018 data fit (up to a constant) with the N2013 best fit parameters, again binned for clarity. The 2013 parameters fit the 2018 data reasonably well, especially between 4-10 keV. However, above above 30 keV the model does a poor job at predicting the increase in flux.

The reflection fractions calculated were:  $R_{N2018} = (3_{-2}^{+12}) \times 10^{17}$ ;  $R_{N2013} = 0.5_{-0.2}^{+0.5}$ ; and  $R_{S2012} = 0.2 \pm 0.1$ . We can see that the N2018 spectra was heavily reflection dominated, with the power law component completely suppressed. However, the N2013 and S2012 spectra are not reflection dominated, with reflection fractions less than unity. This rapid swing in reflection fraction is unlikely to be physical, especially given the similarities in spectral shape and brightness between N2018 and N2013.

Although the blurred reflection scenario produces a good statistical fit for all epochs, the photon index and reflection fraction needed for the N2018 epochs render the validity of the model questionable. Below 30 keV the simple blurred reflection scenario provides a good fit to the data, and produces reasonable reflection fractions and  $\Gamma$  values, which is consistent with previous work that did not have the N2018 spectral data up to 50 keV.

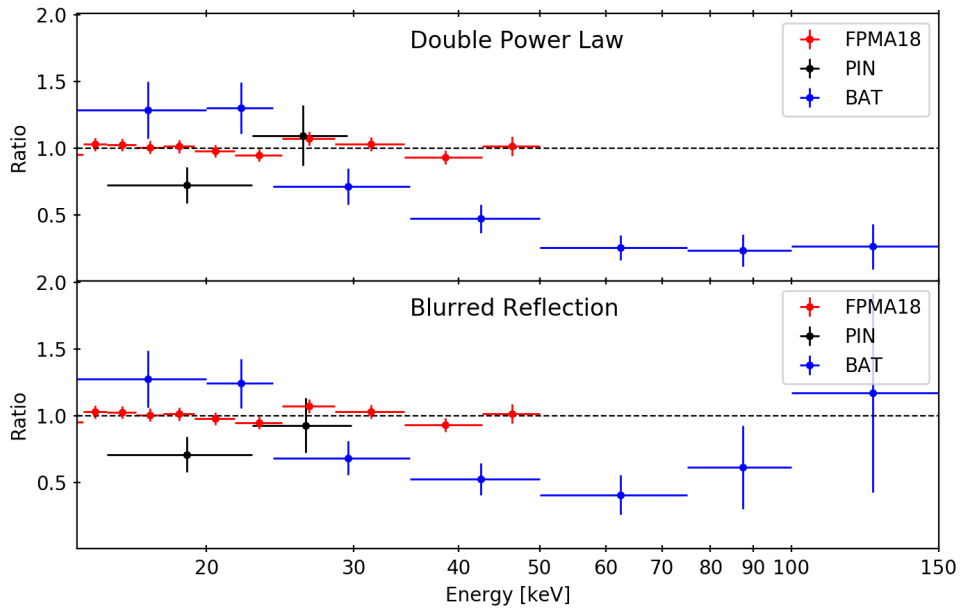


Figure 3.11: *PIN* and *BAT* spectra examine to higher energies than used in spectral fitting. The *PIN* spectrum is linked to the S2012 parameters and scaled by a constant of 1.18, the *BAT* spectrum is linked to the N2018 parameters. *Top panel*: Residuals for the double power law model extended to 150 keV, with *PIN* and *BAT* data over plotted. *Bottom panel*: Residuals for the blurred reflection model extended to 150 keV, with *PIN* and *BAT* data over plotted.

### 3.5.2 Hard Excess

Utilizing the last two spectra discussed in Section 3.2, the *PIN* and *BAT* spectra, we can examine the high energy predictions of each model. This is done by linking the *PIN* and *BAT* data to the S2012 and N2018 parameters, respectively then extending the models to higher energies. Figure 3.11 shows the residuals for the *PIN* and *BAT* spectra. The residuals are reasonably similar for both the double power law and blurred reflection model up to approximately 90 keV, after that the double power law model predicts an excess of flux. While the double power law model does describe the data and variability reasonably well below 50 keV it is not able to describe the data above 50 keV, over predicting the flux. Further study is needed to understand the hard excess of WKK 4438.

The over prediction of flux in the *BAT* spectra is consistent with the lower flux levels we

saw in the unfolded spectra (Figure 3.4). The data for the *BAT* spectra were collected over many years (2004-2013), whereas the N2018 data were collected in a single pointed observation. It is possible that the drastic change in flux is due to a flaring event that occurred during the pointed observation or a long term change in the high energy spectra occurring in recent years.

The spectra of WKK 4438 may in fact be very similar to the high-luminosity quasar 3C 273 which hosts a radio emitting jet. The spectra of 3C 273 requires a broad iron line ( $\sigma = 0.65$  keV) and two emission components, one for the AGN and one for the jet (Madsen et al. 2015). The photon index for the jet is consistent with the one we measure with our hard power law. The soft photon index is much softer in WKK 4438 than in 3C 273, however that could be attributed to the higher mass SMBH, with 3C 273 host a  $\sim 10^9 M_{\odot}$  SMBH (Peterson et al. 2004).

Madsen et al. (2015) utilized a more complex power law, PEGPWRLW, which pegs the flux of the component, preventing it from being suppressed, and a different reflection model, PEXRAV (Magdziarz & Zdziarski 1995). Using the *BAT* and *PIN* data in addition to these more complex/physical models may lead to a more complete description of WKK 4438, helping to determine if SSC emission is contributing to the hard excess. These models could be investigated for WKK 4438. As well, broader band spectroscopy, including the existing data in the IR and microwave, may be used to consider jet models in detail.

### 3.5.3 Broad Iron Line

The flux of the broad iron line derived from the best fit double power law model is about  $2 - 3 \times 10^{-13}$  erg cm<sup>-2</sup> s<sup>-1</sup> at all epochs. Despite the change in continuum flux between the S2012, N2013 and N2018 epochs, the flux of the iron line remains consistent. Combining with the results of the spectral fitting with linking Gaussian parameters we see that the Fe K $\alpha$  emission line is consistent in both flux and shape.

A possible interpretation of the emission we see at 6.4 keV is an Fe K $\alpha$  originating from

the BLR. From the measured quantities provided by the Gaussian fit to the Fe  $K\alpha$  line we can find the velocity of the material that would be needed to produce an emission line with the measured width. In measuring velocities, FWHM is typically used rather than  $\sigma$  (FWHM =  $2\sqrt{2\ln 2}\sigma$ ). Using the Doppler broadening formula we calculated the velocity to be  $V_{FWHM} = 40000_{-10000}^{+20000}$ ,  $25000_{-17000}^{+72000}$ , and  $27000_{-6000}^{+16000}$  km s<sup>-1</sup> for the N2018, N2013 and S2012 epochs, respectively. These are significantly higher velocities than measured in the broad-line region, indicating the source of this material is much closer to the central engine than the broad-line region that produces the H $\beta$  line. The velocities measured are consistent with other NLS1s fit with a broad Gaussian for the broad Fe  $K\alpha$  emission line, which were found to have a mean FWHM value of 47000 km s<sup>-1</sup> (Nandra et al. 1997) suggesting the origin of the iron line may lie within the accretion disc.

Using the virial mass equation we can estimate the location of the material responsible for emitting the Fe  $K\alpha$  line. The virial mass is given by

$$M = f \frac{r_{\text{FeK}\alpha} \sigma_{RMS}^2}{G}, \quad (3.1)$$

where  $f$  is a factor dependant on the geometry of the system;  $r_{\text{FeK}\alpha}$  is the radius (in  $r_g$ ) that the material is emitted by;  $\sigma_{RMS} = (\sqrt{3}/2)V_{FWHM}$ , is the root mean square velocity of the emitting material; and  $G$  is the gravitational constant ( $G = 4.3 \times 10^{-3} \frac{\text{pc}}{\text{M}_\odot} (\frac{\text{km}}{\text{s}})^2$ ) (Peterson & Wandel 1999). For an isotropic velocity field,  $f = \sqrt{3}/2$ , however motion in the disc is ordered and thus a factor  $f = 1.3$  would be more appropriate (Labita et al. 2006). Finally, gravitational redshift must be considered as it can artificially broaden the line widths and in turn the velocity of the line profile. To account, for gravitational redshift we can express the

$\Delta V_{FWHM}$ , the change in velocity due to gravitational redshift as (Peterson & Wandel 1999):

$$\Delta V_{FWHM} = \frac{MG}{c r_{\text{FeK}\alpha}}, \quad (3.2)$$

where  $c$  is the speed of light. Working with the S2012 data, the radius Fe  $K\alpha$  emitting region is  $r_{\text{FeK}\alpha} = 150_{-100}^{+70} r_g$ . This is nearer than the BLR, but farther than the location on the accretion disc where blurred reflection originates.

### 3.6 Conclusion

Using broadband multi-epoch X-ray spectra to study WKK 4438 reveals limited short term spectral variability, whereas the long term variability is dominated by a change in normalization below 30 keV. Above 30 keV more study is needed to understand the origins of the long term variability.

A double power law model can describe the excess emission seen in WKK 4438 for the pointed observations (e.g. S2012, N2013, N2018). This could suggest the presence of jet emission, which is consistent with WKK 4438 being a  $\gamma$ -ray source. However, the double power law model over predicts the flux levels seen in the *BAT* data. This discrepancy could be due to a flare during the N2018 observation or insufficiencies in the model applied.

The blurred reflection model can naturally explain the origin of the broad Fe  $K\alpha$  line as well as the hard excess (in the form of a Compton hump). However, the parameters derived from the best fit models are not self consistent, a non-physical change in reflection fraction would be necessary to explain the spectra presented.

Future work on this object may take many forms, initially more complex and physical models should be tested on the data. These may include, but are not limited to a double power law plus blurred reflection model; jet models similar to 3C 273; or spectral fitting including the high

energy *BAT* data.

As well, very deep *NuSTAR* observations might help to pin down the origin of the hard excess, by improving the spectra signal to noise past 50 keV. Variability studies of the Fe  $K\alpha$  line might help reveal its origin. Timing analysis and reverberation mapping could help to pin down the radius of the Fe  $K\alpha$  region.

Finally WKK 4438 has no radio observations to date to confirm the existence of a jet. Detecting the presence of a jet in the radio band will help identify the contributions the jet may make to the X-ray emission.

## Chapter 4

### Conclusion

Mrk 1239 and WKK 4438 are two ‘weird’ examples of NLS1s. While they show typical behaviours and properties of NLS1s (e.g. steep soft X-ray photon indexes,  $H\beta$  widths  $< 2000$  km s<sup>-1</sup>, rapid variability, low SMBH masses), they also show extremely peculiar behaviour. Mrk 1239 has very little rapid variability in its soft excess while exhibiting more typical NLS1 behaviour above 3 keV. WKK 4438 exhibits excess hard emission above 30 keV that is inconsistent with typical AGN behaviour. It could be that WKK 4438 possesses a jet and is a member of the rare group of jetted NLS1s. Broadband spectral modelling was required to uncover the true nature of these objects.

Mrk 1239 shows a strong soft excess in its X-ray spectrum and attempts to model it with a soft-Comptonization or blurred reflection fail to completely describe the emission seen. The unique timing properties of Mrk 1239 revealed in this work point to a large scale origin for the soft excess.

The excess line emission in Mrk 1239, which was originally attributed to Ne IX (Grupe et al. 2004) was shown to be a blend of iron L transitions. This unusual origin of the soft excess may not have been found if not for the higher energy *NuSTAR* and *Suzaku* data which helped to uncover the consistent flux below 3 keV over many years and thus point to large scale origins.



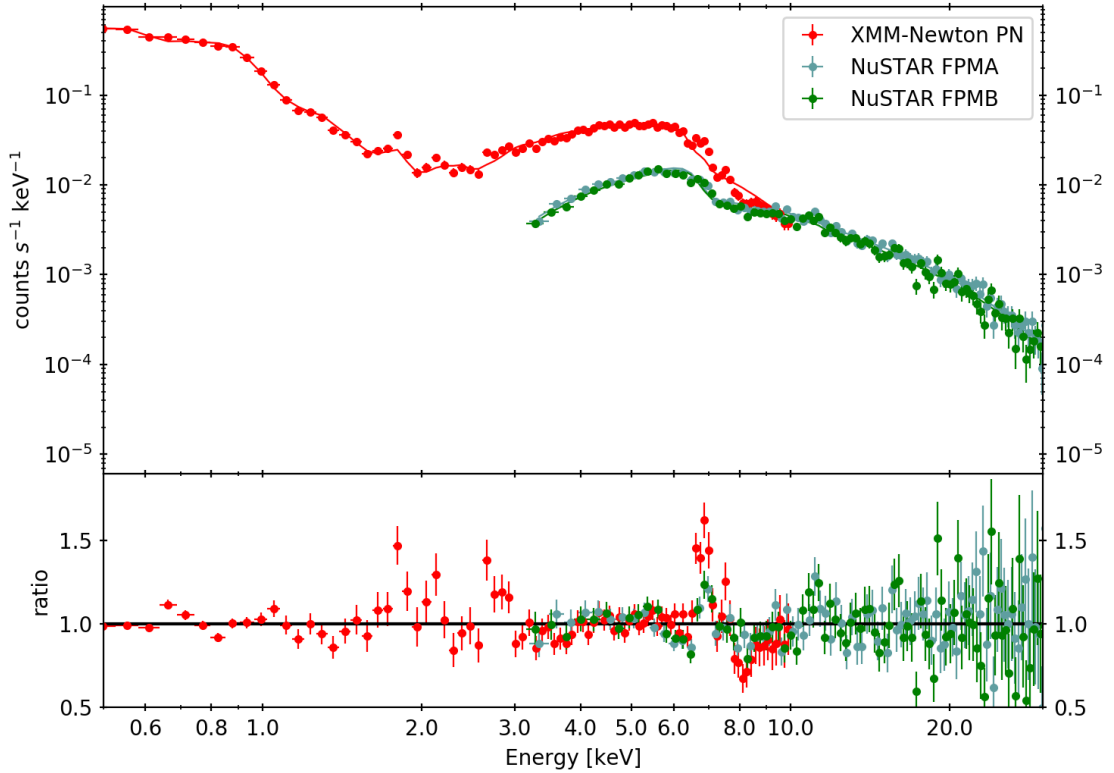


Figure 4.1: *Top panel:* Simulated *XMM-Newton* (pn, 60 ks) and *NuSTAR* (100 ks for FPMA and FPMB) data using the ionized partial covering developed for Mrk 1239. Data were then fit with the blurred reflection model developed for Mrk 1239. *Bottom panel:* residuals for the fits presented above.

In future work we endeavor to describe the spectra of Mrk 1239 more completely, as a 100 ks joint *XMM-Newton/NuSTAR* proposal has been excepted in *NuSTAR*-Cycle 7 (proposal number 7165<sup>1</sup>) with priority A. From the 100 ks of proposed time, we expect to receive  $\sim 60$  ks of good data for the pn instrument (due to background flaring), and 100 ks for both FPMA and FPMB. From these observations we expect to be able to differentiate between the two best fit models in Chapter 2. This was tested by simulating an observation of *NuSTAR* and *XMM-Newton* using the best fit ionized partial covering model and fitting it with the blurred reflection model. The residuals in Figure 4.1 show a strong deviation in the fit, especially near the broad Fe  $K\alpha$  line. From the new high energy observations (e.g. pn and *NuSTAR*) the contribution from cold distant material (e.g. the torus; XILLVER) are expected to be constrained.

<sup>1</sup>[https://heasarc.gsfc.nasa.gov/docs/nustar/ao7/c7\\_accepted\\_program\\_abstracts.html](https://heasarc.gsfc.nasa.gov/docs/nustar/ao7/c7_accepted_program_abstracts.html)

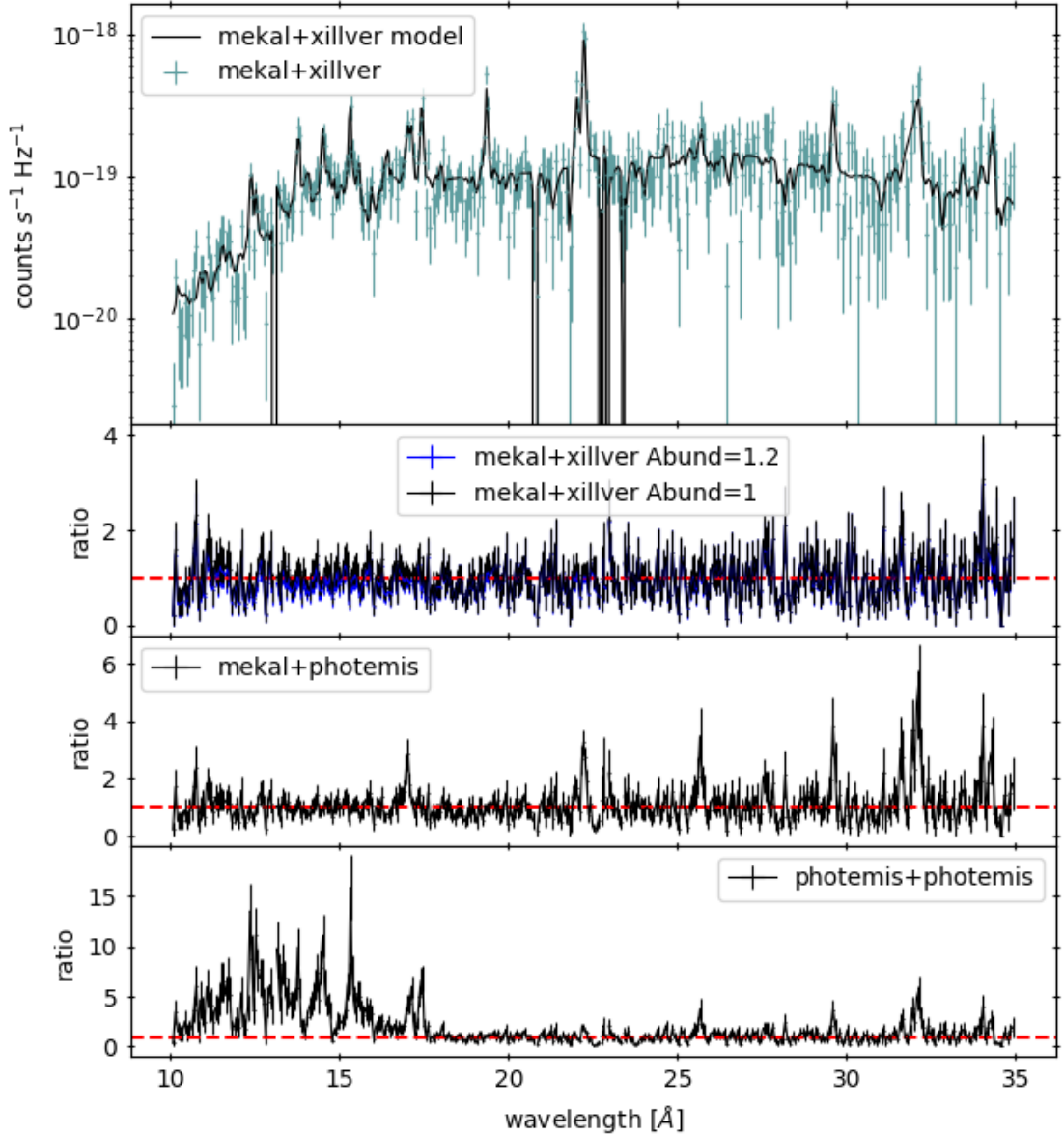


Figure 4.2: Simulated *XMM-Newton* RGS data are tested against other models. *Top panel:* Simulated *XMM-Newton* RGS (100 ks) data using the ionized partial model covering developed for Mrk 1239. *Second panel:* Residuals for the data presented above, modelled using MEKAL+XILLVER. In blue the abundance has been increased by 20%. *Third panel:* Residuals for the data modelled using MEKAL+PHOTEMIS for emission collisionally ionized and photoionized plasma. *Bottom panel:* Residuals for the data modelled using PHOTEMIS+PHOTEMIS for two separate region that have been photoionized.

We expect to receive good quality Reflection Grating Spectrometer (RGS) spectra from the 100 ks *XMM-Newton* observation. By constraining the torus contributions using the 0.5-30 keV spectra we can determine what emission lines are due to the torus and which arise from possible

star forming regions in Mrk 1239. Figure 4.2 shows the simulated RGS spectra based on our best fit models as well as several alternative scenarios which this work was unable to distinguish. We can see that the new observation will be able to shed more light on the mechanisms producing the strange soft excess seen in Mrk 1239. With the RGS data we expect to be able to isolate the emission lines due to cold reflection, leaving only the distant (starburst) emission.

Turing towards WKK 4438, where the exact origin of the hard excess seen in the X-ray spectra remains unclear. Neither model proposed in this work succeeded in providing a complete picture of WKK 4438. Instead we gained insights into the nature of the hard excess, and we can confirm that based on the multi-epoch broadband fit of the spectra that the traditional blurred reflection scenario fails to account for the hard excess via the Compton hump. While the fit was statistically valid, the parameters obtained from the fit are inconsistent with what we expect from a blurred reflection scenario.

The best fit model for WKK 4438 is consistent with a soft Comptonization scenario, however, the parameters derived are not. Typically, when NLS1s require two coronal components, there is the standard power law component from the corona, and a softer Comptonization component from a cool, optically thick electron cloud over the accretion disc (Done et al. 2012). In WKK 4438 we find the standard AGN corona components and a second harder powerlaw component. This component is needed to explain the excess in emission seen in the 2018 *NuSTAR* observation.

Further study is required to understand the complex nature of WKK 4438. Using additional archival data from *Swift-BAT* will aid in understanding the hard excess, allowing us to understand how much emission is from the AGN and how much is from a possible jet component.

NLS1 are important for understanding the Seyfert phenomenon, growth, and evolution of AGN. However, the class may not be unique as Mrk 1239 and WKK 4438 show. Both objects have been modelled as typical NLS1s (e.g. Grupe et al. 2004, Jiang et al. 2018). However,

looking at their timing properties and spectral shape reveal their unique behaviour. Caution should be taken when considering NLS1 as a class. The same phenomena do not uniquely describe all objects in this class. Broadband, multi-epoch study is necessary to understand the complex nature of individual objects.

# Bibliography

Ajello, M., Alexander, D. M., Greiner, J., et al. 2012, *ApJ*, 749, 21

Antonucci, R. 1993, *ARA&A*, 31, 473

Antonucci, R. R. J. & Miller, J. S. 1985, *ApJ*, 297, 621

Arnaud, K. A. 1996, in *Astronomical Society of the Pacific Conference Series*, Vol. 101, *Astronomical Data Analysis Software and Systems V*, ed. G. H. Jacoby & J. Barnes, 17

Ballantyne, D. R., Ross, R. R., & Fabian, A. C. 2001, *MNRAS*, 327, 10

Bassani, L., Molina, M., Malizia, A., et al. 2005, *ApJ*, 636, L65

Baumgartner, W. H., Tueller, J., Markwardt, C. B., et al. 2013, *ApJS*, 207, 19

Beckmann, V. & Shrader, C. 2013, *PoS, INTEGRAL 2012*, 069

Beers, T. C., Kriessler, J. R., Bird, C. M., & Huchra, J. P. 1995, *AJ*, 109, 874

Berton, M., Congiu, E., Järvelä, E., et al. 2018, *A&A*, 614, A87

Berton, M., Foschini, L., Ciroi, S., et al. 2015, *A&A*, 578, A28

Blandford, R., Meier, D., & Readhead, A. 2019, *Annu. Rev. Astron. Astrophys.*, 57, 467

Boller, T., Brandt, W. N., & Fink, H. 1996, *AAP*, 305, 53

- Boller, T., Fabian, A., Sunyaev, R., et al. 2002, MNRAS, 329, L1
- Bonson, K. & Gallo, L. C. 2016, MNRAS, 458, 1927
- Bonson, K., Gallo, L. C., Wilkins, D. R., & Fabian, A. C. 2018, MNRAS, 477, 3247
- Boorman, P. G., Gandhi, P., Stern, D., Harrison, F., & NuSTAR Obscured AGN Team. 2018, in American Astronomical Society Meeting Abstracts, Vol. 231, American Astronomical Society Meeting Abstracts #231, 343.01
- Brandt, W. N., Mathur, S., & Elvis, M. 1997, MNRAS, 285, L25
- Brightman, M., Silverman, J. D., Mainieri, V., et al. 2013, MNRAS, 433, 2485
- Burrows, D. N., Hill, J. E., Nousek, J. A., et al. 2004, in Society of Photo-Optical Instrumentation Engineers (SPIE) Conference Series, Vol. 5165, X-Ray and Gamma-Ray Instrumentation for Astronomy XIII, ed. K. A. Flanagan & O. H. W. Siegmund, 201–216
- Cash, W. 1979, ApJ, 228, 939
- Chiang, C.-Y., Walton, D. J., Fabian, A. C., Wilkins, D. R., & Gallo, L. C. 2015, MNRAS, 446, 759
- Cunningham, C. 1976, ApJ, 208, 534
- Doi, A., Wajima, K., Hagiwara, Y., & Inoue, M. 2015, ApJL, 798, L30
- Done, C., Davis, S. W., Jin, C., Blaes, O., & Ward, M. 2012, MNRAS, 420, 1848
- Edelson, R., Turner, T. J., Pounds, K., et al. 2002, ApJ, 568, 610
- Evans, P. A., Beardmore, A. P., Page, K. L., et al. 2009, MNRAS, 397, 1177
- Fabian, A. C., Iwasawa, K., Reynolds, C. S., & Young, A. J. 2000, PASP, 112, 1145

Fabian, A. C., Lohfink, A., Kara, E., et al. 2015, MNRAS, 451, 4375

Fabian, A. C., Miniutti, G., Gallo, L., et al. 2004, MNRAS, 353, 1071

Fabian, A. C., Rees, M. J., Stella, L., & White, N. E. 1989, MNRAS, 238, 729

Fabian, A. C., Zoghbi, A., Ross, R. R., et al. 2009, Nature, 459, 540

Fanaroff, B. L. & Riley, J. M. 1974, MNRAS, 167, 31P

Foschini, L., Angelakis, E., Fuhrmann, L., et al. 2012, A&A, 548, A106

Foschini, L., Berton, M., Caccianiga, A., et al. 2015, A&A, 575, A13

Franceschini, A., Braito, V., Persic, M., et al. 2003, MNRAS, 343, 1181

Fukazawa, Y., Hiragi, K., Mizuno, M., et al. 2011, ApJ, 727, 19

Fukazawa, Y., Mizuno, T., Watanabe, S., et al. 2009, pASJ, 61, S17

Gallo, L. 2018, PoS, NLS1-2018, 034

Gallo, L. C. 2006, MNRAS, 368, 479

Gallo, L. C. 2011, J. R. Astron. Soc. Can., 105, 143

Gallo, L. C., Brandt, W. N., Costantini, E., & Fabian, A. C. 2007a, MNRAS, 377, 1375

Gallo, L. C., Brandt, W. N., Costantini, E., et al. 2007b, MNRAS, 377, 391

Gallo, L. C., Edwards, P. G., Ferrero, E., et al. 2006, MNRAS, 370, 245

Gallo, L. C., Fabian, A. C., Grupe, D., et al. 2012, MNRAS, 428, 1191

Gallo, L. C., Gonzalez, A. G., Waddell, S. G. H., et al. 2019, MNRAS, 484, 4287

Gallo, L. C., Wilkins, D. R., Bonson, K., et al. 2015, MNRAS, 446, 633

García, J., Dauser, T., Lohfink, A., et al. 2014, *ApJ*, 782, 76

George, I. M. & Fabian, A. C. 1991, *MNRAS*, 249, 352

Ghisellini, G. & Maraschi, L. 1989, *ApJ*, 340, 181

Gierliński, M. & Done, C. 2004, *MNRAS*, 349, L7

Gonzalez, A. G., Gallo, L. C., Kosec, P., et al. 2020, *MNRAS*, 496, 3708

Gonzalez, A. G., Wilkins, D. R., & Gallo, L. C. 2017, *MNRAS*, 472, 1932

Goodman, J. & Weare, J. 2010, *Commun. Appl. Math. Comput. Sci.*, 5, 65

Goodrich, R. W. 1989, *ApJ*, 342, 224

Grupe, D., Beuermann, K., Thomas, H. C., Mannheim, K., & Fink, H. H. 1998, *A&A*, 330, 25

Grupe, D., Komossa, S., Gallo, L., et al. 2019, *MNRAS*, 486, 227

Grupe, D., Komossa, S., Gallo, L. C., et al. 2008, *The Astrophysical Journal*, 681, 982

Grupe, D., Komossa, S., Leighly, K. M., & Page, K. L. 2010, *ApJS*, 187, 64

Grupe, D., Mathur, S., & Komossa, S. 2004, *AJ*, 127, 3161

Grupe, D., Thomas, H. C., & Beuermann, K. 2001, *A&A*, 367, 470

Haardt, F. & Maraschi, L. 1991, *ApJL*, 380, L51

Haardt, F. & Maraschi, L. 1993, *ApJ*, 413, 507

Harrison, F. A., Craig, W. W., Christensen, F. E., et al. 2013, *ApJ*, 770, 103

Holt, S. S., Mushotzky, R. F., Becker, R. H., et al. 1980, *ApJL*, 241, L13

Ishibashi, W. 2020, *MNRAS*, 495, 2515



- Iso, N., Ebisawa, K., Sameshima, H., et al. 2016, PASJ, 68, s27
- Ivezić, Ž., Connelly, A. J., Vanderplas, J. T., & Gray, A. 2019, Statistics, Data Mining, and Machine Learning in Astronomy
- Jansen, F., Lumb, D., Altieri, B., et al. 2001, AAP, 365, L1
- Jensen, J. J., Hönic, S. F., Rakshit, S., et al. 2017, MNRAS, 470, 3071
- Jiang, J., Fabian, A. C., Dauser, T., et al. 2019, MNRAS, 489, 3436
- Jiang, J., Parker, M. L., Fabian, A. C., et al. 2018, MNRAS, 477, 3711
- Jiang, J., Walton, D. J., Parker, M. L., & Fabian, A. C. 2018, MNRAS, 481, 639
- Kaastra, J. S. & Bleeker, J. A. M. 2016, A&A, 587, A151
- Kataoka, J., Mattox, J. R., Quinn, J., et al. 1999, ApJ, 514, 138
- Kellermann, K. I., Sramek, R., Schmidt, M., Shaffer, D. B., & Green, R. 1989, AJ, 98, 1195
- Komossa, S. 2008, in Rev. Mex. Astron. Astrofis. Conference Series, Vol. 32, Rev. Mex. Astron. Astrofis. Conference Series, 86–92
- Komossa, S., Grupe, D., Schartel, N., et al. 2016, Proc. Int. Astron. Union, 12, 168
- Komossa, S., Voges, W., Xu, D., et al. 2006, AJ, 132, 531
- Koratkar, A. & Blaes, O. 1999, PASP, 111, 1
- Labita, M., Treves, A., Falomo, R., & Uslenghi, M. 2006, MNRAS, 373, 551
- Landi, R., Masetti, N., Gehrels, N., et al. 2007, ATel, 990, 1
- Laor, A. 1991, ApJ, 376, 90
- Laor, A., Fiore, F., Elvis, M., Wilkes, B. J., & McDowell, J. C. 1997, ApJ, 477, 93

- Leighly, K. M. 1999a, ApJS, 125, 297
- Leighly, K. M. 1999b, ApJs, 125, 317
- Liedahl, D. A., Osterheld, A. L., & Goldstein, W. H. 1995, ApJL, 438, L115
- Liu, T., Wang, J.-X., Yang, H., Zhu, F.-F., & Zhou, Y.-Y. 2014, ApJ, 783, 106
- Longair, M. S. 2011, High Energy Astrophysics (Cambridge University Press)
- Madsen, K. K., Fürst, F., Walton, D. J., et al. 2015, ApJ, 812, 14
- Magdziarz, P., Blaes, O. M., Zdziarski, A. A., Johnson, W. N., & Smith, D. A. 1998, MNRAS, 301, 179
- Magdziarz, P. & Zdziarski, A. A. 1995, MNRAS, 273, 837
- Malizia, A., Bassani, L., Bird, A. J., et al. 2008, MNRAS, 389, 1360
- Marin, F. 2016, MNRAS, 460, 3679
- Marinucci, A., Matt, G., Kara, E., et al. 2014, MNRAS, 440, 2347
- Martin, P. G., Thompson, I. B., Maza, J., & Angel, J. R. P. 1983, ApJ, 266, 470
- Masetti, N., Morelli, L., Palazzi, E., et al. 2006, A&A, 459, 21
- Mathur, S. 2000, MNRAS, 314, L17
- Meléndez, M., Mushotzky, R. F., Shimizu, T. T., Barger, A. J., & Cowie, L. L. 2014, ApJ, 794, 152
- Miniutti, G. & Fabian, A. C. 2004, MNRAS, 349, 1435
- Mitsuda, K., Bautz, M., Inoue, H., et al. 2007, PASJ, 59, S1
- Miyakawa, T., Ebisawa, K., & Inoue, H. 2012, PASJ, 64, 140

- Miyazawa, T., Haba, Y., & Kunieda, H. 2009, pASJ, 61, 1331
- Nandra, K., George, I. M., Mushotzky, R. F., Turner, T. J., & Yaqoob, T. 1997, ApJ, 477, 602
- Nandra, K., O'Neill, P. M., George, I. M., & Reeves, J. N. 2007, MNRAS, 382, 194
- Netzer, H. 2013, *The Physics and Evolution of Active Galactic Nuclei*. (Cambridge University Press)
- Nikolajuk, M., Czerny, B., & Gurynowicz, P. 2009, MNRAS, 394, 2141
- Oh, K., Koss, M., Markwardt, C. B., et al. 2018, ApJS, 235, 4
- Osterbrock, D. E. 1977, ApJ, 215, 733
- Osterbrock, D. E. & Pogge, R. W. 1985, ApJ, 297, 166
- Pan, X., Zhou, H., Yang, C., et al. 2021, ApJ, 912, 118
- Parker, M. L., Longinotti, A. L., Schartel, N., et al. 2019, MNRAS, 490, 683
- Peterson, B. M. 1997, *An Introduction to Active Galactic Nuclei* (Cambridge University Press)
- Peterson, B. M., Ferrarese, L., Gilbert, K. M., et al. 2004, ApJ, 613, 682
- Peterson, B. M. & Wandel, A. 1999, ApJL, 521, L95
- Petrucci, P. O., Haardt, F., Maraschi, L., et al. 2001, ApJ, 556, 716
- Ponti, G., Gallo, L. C., Fabian, A. C., et al. 2010, MNRAS, 406, 2591
- Ponti, G., Papadakis, I., Bianchi, S., et al. 2012, A&A, 542, A83
- Pounds, K. A., Done, C., & Osborne, J. P. 1995, MNRAS, 277, L5
- Puchnarewicz, E. M., Mason, K. O., Cordova, F. A., et al. 1992, MNRAS, 256, 589

- Raymond, J. C. & Smith, B. W. 1977, *ApJS*, 35, 419
- Reeves, J., Done, C., Pounds, K., et al. 2008, *MNRAS: Letters*, 385, L108
- Ricci, C., Ueda, Y., Paltani, S., et al. 2014, *MNRAS*, 441, 3622
- Risaliti, G., Harrison, F. A., Madsen, K. K., et al. 2013, *Nature*, 494, 449
- Rodríguez-Ardila, A. & Mazzalay, X. 2006, *MNRAS: Letters*, 367, L57
- Rodríguez-Ardila, A. & Viegas, S. M. 2003, *MNRAS*, 340, L33
- Ross, R. R. & Fabian, A. C. 2005, *MNRAS*, 358, 211
- Ruschel-Dutra, D., Rodríguez Espinosa, J. M., González Martán, O., Pastoriza, M., & Riffel, R. 2016, *MNRAS*, 466, 3353
- Rush, B. & Malkan, M. A. 1996, *ApJ*, 456, 466
- Ryan, C. J., De Robertis, M. M., Virani, S., Laor, A., & Dawson, P. C. 2007, *ApJ*, 654, 799
- Rybicki, G. B. & Lightman, A. P. 1979, *Radiative processes in astrophysics* (Wiley)
- Sani, E., Lutz, D., Risaliti, G., et al. 2010, *MNRAS*, 403, 1246
- Seyfert, C. K. 1943, *ApJ*, 97, 28
- Shakura, N. I. & Sunyaev, R. A. 1973, *A&A*, 500, 33
- Shapiro, S. L., Lightman, A. P., & Eardley, D. M. 1976, *ApJ*, 204, 187
- Skrutskie, M. F., Cutri, R. M., Stiening, R., et al. 2006, *AJ*, 131, 1163
- Takahashi, T., Kokubun, M., Mitsuda, K., et al. 2016, in *Society of Photo-Optical Instrumentation Engineers (SPIE) Conference Series*, Vol. 9905, pSPIE, 99050U

- Tanaka, Y., Boller, T., & Gallo, L. 2005, in *Growing Black Holes: Accretion in a Cosmological Context*, ed. A. Merloni, S. Nayakshin, & R. A. Sunyaev, 290–295
- Tanaka, Y., Boller, T., Gallo, L., Keil, R., & Ueda, Y. 2004, *PASJ*, 56, L9
- Tanaka, Y., Ueda, Y., & Boller, T. 2003, *MNRAS*, 338, L1
- Tashiro, M., Maejima, H., Toda, K., et al. 2018, in *Society of Photo-Optical Instrumentation Engineers (SPIE) Conference Series*, Vol. 10699, pSPIE, 1069922
- Titarchuk, L. 1994, *ApJ*, 434, 570
- Tramacere, A., Giommi, P., Perri, M., Verrecchia, F., & Tosti, G. 2009, *A&A*, 501, 879
- Truemper, J. 1982, *Adv. Space Res.*, 2, 241
- Tueller, J., Baumgartner, W. H., Markwardt, C. B., et al. 2010, *ApJS*, 186, 378
- Turner, T. J., Miller, L., Reeves, J. N., & Kraemer, S. B. 2007, *A&A*, 475, 121
- Véron-Cetty, M. P. & Véron, P. 2001, *AAP*, 374, 92
- Waddell, S. G. H. & Gallo, L. C. 2020, *MNRAS*, 498, 5207
- Waddell, S. G. H., Gallo, L. C., Gonzalez, A. G., Tripathi, S., & Zoghbi, A. 2019, *MNRAS*, 489, 5398
- Walton, D. J., Nardini, E., Gallo, L. C., et al. 2019, *MNRAS*, 484, 2544
- Wilkins, D. R. & Fabian, A. C. 2012, *MNRAS*, 424, 1284
- Wilkins, D. R. & Gallo, L. C. 2015, *MNRAS*, 449, 129
- Wilkins, D. R., Gallo, L. C., Silva, C. V., et al. 2017, *MNRAS*, 471, 4436

Willingale, R., Starling, R. L. C., Beardmore, A. P., Tanvir, N. R., & O'Brien, P. T. 2013,  
MNRAS, 431, 394

Wilms, J., Allen, A., & McCray, R. 2000, ApJ, 542, 914

Woudt, P. A. & Kraan-Korteweg, R. C. 2001, A&A, 380, 441

Yao, S., Qiao, E., Wu, X.-B., & You, B. 2018, MNRAS, 477, 1356

Zhang, T.-Z. & Wu, X.-B. 2002, CJAA, 2, 487